

DISS. ETH NO. 19572

Visually Servoing Wireless Magnetic Intraocular Microrobots

A dissertation submitted to

ETH ZURICH

for the degree of

Doctor of Sciences

presented by

CHRISTOS BERGELES

Dipl.-Ing, National Technical University of Athens

March 21, 1984

citizen of the Hellenic Republic

accepted on the recommendation of

Prof. Bradley J. Nelson, ETH Zurich, examiner,
Prof. Gregory Hager, Johns Hopkins University, co-examiner

2011

With a major thank you to my mother, my father, my brother, and my
close friends.

Words like that are improper, blasphemous.
Just to be on the first step should make you happy and proud.
To have come this far is no small achievement:
what you have done is a glorious thing.
Even this first step is a long way above the ordinary world.
To stand on this step
you must be in your own right a member of the city of ideas.
And it is a hard, unusual thing to be enrolled as a citizen of that city.
Its councils are full of Legislators no charlatan can fool.
To have come this far is no small achievement:
what you have done already is a glorious thing.

C. P. Cavafy, from "The First Step", Collected Poems.

Acknowledgments

This dissertation is the cumulative result of four years of Doctoral Studies at the Institute of Robotics and Intelligent Systems (IRIS) at ETH Zurich. My Ph. D. work allowed me to see computer vision from a different viewpoint. Having to go back to the fundamentals of image formation and examine existing methods under new perspectives was for me a great twist.

This work would not be possible without the help of many people. I would like to thank Prof. Brad Nelson for his inspiring guidance and support throughout these years. Brigitte Geissmann always helped me avoid quagmires when dealing with any kind of administrative issues. Prof. Jake Abbott's help was invaluable during my first steps as a Ph. D. student, and without his assistance, the transition from my university years would have been painful. Dr. Brad Kratochvil is acknowledged for his support during the last years of my studies. I also want to thank Chauncey Graetzel, Zoltan Nagy, and Dominic Frutiger, my office-mates during these wonderful four years. Their example for a guiding force for my efforts.

I am thankful to students I collaborated with: to Kamran Shamaei for our initial work on focus-based localization, to George Fagogenis for our work on color-based tracking, and to Mourad ben Ayed for his work on optics.

For contributions in this thesis, I would like to thank Prof. D. A. Atchison from the School of Optometry, Queensland University of Technology, Australia, for providing the high resolution images of ocular MRI scans. Michael Kummer's help on the experiments with cadaver eyes and simulated vitreous humors is greatly appreciated. The assistance of Oertli Switzerland through the donation of a fully functional vitrectomy system and their time spent in training me in vitrectomies was also invaluable. Prof. Bernhard Spiess from the Small Animal Clinic of the Animal Hospital, Zurich gave me great advice on handling cadaver eyes and on imaging techniques, and Prof. Carsten Frame is acknowledged for his help on experiments in porcine vitreous humor.

Abstract

Robotic systems that can undertake surgical tasks, provide assistance to the clinicians, and augment their capabilities are rapidly being developed. One of the common research areas for surgical robotics is ophthalmology. Ophthalmic procedures require increased dexterity and delicate motions in order to avert any damage caused to the visual receptors. Moreover, drug delivery for ophthalmology presents additional challenges and limitations, since the ideal pathway consists of placing the drug at the pathological location, which is not easily accessible.

Recently, magnetic microrobotic approaches to assist the clinicians have been introduced. The microrobots can perform procedures like retinal vein cannulation, drug delivery, and oxygen sensing. However, precise control of magnetic devices requires position information, both for calculating the electromagnetic field, and for servoing the device itself.

This thesis aims at developing new localization methods for intraocular devices, and at testing the feasibility of intraocular interventions using microrobots. First, we examine the effect of the human-eye optics in image formation, and we develop a focus-based localization algorithm. We additionally develop a method to estimate the position of rigid bodies without requiring focus information. We evaluate the performance of the proposed algorithms with experiments in human-like eye models, and we use them in servoing experiments. Additionally, we experiment with microrobots in synthesized vitreous humors and in cadaver porcine eyes in order to evaluate the devices' capability to move in the interior of the human eye without requiring a vitrectomy. Finally, we present methods to track microdevices using statistical color and shape information.

Zusammenfassung

Robotische, adaptive Systeme zur Durchführung von Operationen und zur Unterstützung des ausführenden Arztes unterlagen im letzten Jahrzehnt einer rapiden Entwicklung. Für viele Operationen werden diese System heute standardmässig eingesetzt.

Eines der typischen Gebiete für chirurgische Robotik ist die Ophthalmologie. Ophthalmologische Behandlungen erfordern ausserordentliche Geschicklichkeit und präzise Motorik um Verletzungen der visuellen Rezeptoren auszuschliessen. Eine weitere Herausforderung stellt das gezielte Verabreichen von Wirkstoffen, direkt an, zum Teil schwer zugänglichen, Krankheitsherden dar.

Minimal-invasive Ansätze zur Unterstützung von Ärzten durch magnetische Mikroroboter wurden erst kürzlich vorgestellt. Diese Mikroroboter sollen Prozeduren wie die Retinal Vein Cannulation, lokale Wirkstoffabgaben und Sauerstoffmessungen durchführen. Die präzise Kontrolle dieser Mikroroboter erfordert jedoch exakte Positionsinformationen. Einerseits für die Berechnung des erforderlichen elektromagnetischen Feldes für die Bewegungsausführung und andererseits für die automatische Steuerung des Instrumentes selbst.

Das Ziel dieser Dissertation ist es neue Lokalisierungsmethoden für intraokulare Instrumente zu entwickeln, sowie Machbarkeitsstudien für intraokulare Eingriffe mit Hilfe von Mikrorobotern zu erstellen. Zuerst werden die Effekte der Optik des menschlichen Auges auf die Bildgebung untersucht und ein fokus-basierter Lokisierungsalgorithmus entwickelt. Zusätzlich wird eine Methode zur Bestimmung der Position eines starren Körpers ohne die Verwendung von Fokusinformationen entwickelt. Die Leistungsfähigkeit der vorgeschlagenen Methoden wird mit Experimenten an Modellen des menschlichen Auges evaluiert. Ebenso wurden die Algorithmen zur automatischen Positionskontrolle eingesetzt. Zusätzlich wird die Bewegungsfähigkeit der Mikroroboter im menschlichen Auge ohne den Einsatz einer Vitrek-

tomie anhand von Experimenten im synthetischen Glaskörper und in Augen von Schweinekadavern evaluiert. Abschliessend werden Tracking-Methoden, beruhend auf statistischer Farb- und Forminformationen, für eine dynamische Robotersteuerung vorgestellt.

Contents

Abstract	iii
Zusammenfassung	iv
List of Tables	ix
List of Figures	x
1 The Human Eye: Structure, Pathologies, Challenges	1
1.1 The Anatomy of the Human Eye	1
1.2 Prevalent Ophthalmic Pathologies	3
1.3 Challenges in Ocular Surgery and Treatment	6
1.4 Conclusions	10
2 Robotic Solutions for Ophthalmology	12
2.1 Surgeon Extenders	12
2.2 Teleoperated or Autonomous Robots	14
2.3 Microrobotic Systems	16
2.4 Sensing Technologies	18
2.5 Problem Statement	19
3 Imaging Intraocular Microdevices	21
3.1 Comparison of Ophthalmoscopy Methods	23
3.2 Wide-Angle Image Formation	28
3.3 Conclusions	31
4 Single-Camera Focus-Based Localization	33
4.1 Algorithm	33
4.2 Sensitivity Analysis	35

4.3	Calibration	39
4.4	Experiments	45
4.5	Conclusions	50
5	Single-Camera Rigid-Body Localization	52
5.1	Common Projection Models	53
5.2	Projecting Through the Eye's Optics	55
5.3	Algorithm	59
5.4	Sensitivity Analysis	60
5.5	Experiments	62
5.6	Conclusions	66
6	Monocular Visual Servoing	69
6.1	Visually Servoing the Electromagnetic Field	71
6.2	Visually Servoing Microrobots	74
6.3	Conclusions	76
7	<i>Ex Vivo</i> Experiments	79
7.1	Experiments with Artificial Vitreous Humors	80
7.2	Experiments with Cadaver Porcine Eyes	83
7.3	Tracking Experiments	89
7.4	Protocol for <i>In Vivo</i> Experimentation	90
7.5	Conclusions	94
8	Color/Shape-Based Tracking of Microdevices	95
8.1	Colorspace Selection	95
8.2	Level-Set Tracking using Statistical Information	97
8.3	Experiments	103
8.4	Conclusions	112
9	Summary: Contributions and Conclusions	113
9.1	Research Contributions	113
9.2	Conclusion	115

References	116
A Developing a Miniaturized Ophthalmoscope	133
A.1 Optical Construction	134
A.2 Illumination	135
A.3 Developed Prototypes and Experimental Work	135
A.4 Discussion	136
Curriculum Vitae	139

List of Tables

1.1	Prevalence of ophthalmic diseases	7
3.1	Optical parameters for direct ophthalmoscopy	24
3.2	Optical parameters for ophthalmoscopy using vitrectomy lenses	26
3.3	Optical parameters for indirect ophthalmoscopy	26
3.4	Optical parameters for an aspheric condensing lens	29
4.1	Focus-based localization errors	50
5.1	Uncertainties in the human-eye parameters	60
5.2	Model-based localization errors due to uncertainties	61
5.3	Optical parameters for the new eye model	65
5.4	Model-based localization results	66
6.1	Magnetic drift compensation	72
7.1	Chemical ingredients for the simulated vitreous humors (a) . .	81
7.2	Chemical ingredients for the simulated vitreous humors (b) . .	81
8.1	Shape-cycle of the level-set tracking algorithm	103
8.2	Colorspace mean quality and standard deviation	109
8.3	Tracking errors for different colorspace	111

List of Figures

1.1	The anatomy of the human eye	2
1.2	Cataract and its effects on vision	3
1.3	Glaucoma and its effects on vision	4
1.4	Age-related macular degeneration and its effects on vision	5
1.5	Diabetic retinopathy and its effects on vision	6
1.6	Typical scenes from ophthalmic surgery	8
1.7	Examples of intraocular drug delivery methods	10
1.8	Drug diffusion study through MRI	11
2.1	Advanced forceps and the Micron	13
2.2	The Steady Hand Robot from JHU	14
2.3	The JPL and Columbia robots	15
2.4	The ETH Zurich microrobotic system	17
2.5	Oxygen sensors for glaucoma monitoring	19
3.1	Simulated effect of the eye's optics on imaging	22
3.2	Image formation in direct ophthalmoscopy	24
3.3	Image formation using contact vitrectomy lenses	25
3.4	Image formation in indirect ophthalmoscopy	27
3.5	Isofocus surfaces and isopixel curves for indirect ophthalmoscopy	30
3.6	Parametrization of the isofocus surfaces and isopixel curves	32
4.1	Flowchart for the focus-based localization algorithm	34
4.2	Sensitivity analysis	38
4.3	Biometric measurements from MRI	40
4.4	First-order model for indirect ophthalmoscopy	41
4.5	Example of biometric calibration	43
4.6	Sensitivity analysis after biometric calibration	44
4.7	Schematic of the experimental setup	45
4.8	Isofocus surfaces and isopixel curves for the experimental setup	46
4.9	Parametrization of the isofocus surfaces and isopixel curves	48

4.10 Calibration of the experimental setup	49
4.11 Localization results for a planar object in a model eye	51
5.1 The raxel-based projection model	55
5.2 Flowchart for the model-based localization algorithm	56
5.3 Updated parametrization of the isopixel curves	57
5.4 Projection of intraocular objects in three dimensions	58
5.5 The electromagnetic control system with the model eye	63
5.6 The new human-like eye model	64
5.7 Model-based localization results	68
6.1 Visual servoing flowchart	70
6.2 Screenshot of the developed interface	71
6.3 Magnetic drift compensation for a CoNi microrobot	73
6.4 Microrobotic devices used for visual servoing experiments	74
6.5 Automated visual servoing of a CoNi microrobot	74
6.6 The electromagnetic control system with a model eye	75
6.7 Semi-automated visual servoing of a NdFeB microrobot	77
6.8 Visual servoing interface	78
7.1 <i>In vitro</i> experiments with vitreous humors	80
7.2 Prepared vitreous simulators	82
7.3 CoNi microrobot moving by tumbling	83
7.4 Cadaver porcine eyes for <i>ex vivo</i> experimentation	84
7.5 Experimental workstation	85
7.6 Removing the porcine cornea, and our surgical tools	86
7.7 Comparison of transscleral illumination and endoillumination	87
7.8 <i>Ex vivo</i> experiment with NdFeB microrobots (1)	88
7.9 <i>Ex vivo</i> experiment with NdFeB microrobots (2)	89
7.10 <i>Ex vivo</i> tracking of an NdFeB microrobot	90
7.11 Developing a protocol for <i>in vivo</i> experimentation	91
7.12 Pictures of the experimental process	93
7.13 Microrobots and veins	94
8.1 Illustration of level-set tracking and the propagating front	98
8.2 Micromanipulation with a MagMite (1)	105
8.3 Micromanipulation with a MagMite (2)	106

8.4	Basic incorporation of shape information to handle occlusions	107
8.5	Experimental setup for tracking using color information	108
8.6	Colorspace evaluation	109
8.7	Tracking in different colorspace	110
8.8	Tracking on a chorioallantoic membrane using color information	111
8.9	Tracking using color and shape information	112
A.1	Concept of the miniaturized ophthalmoscope	135
A.2	Concept of the transscleral LED illuminator	136
A.3	CAD model and first prototype	136
A.4	Final device prototypes	137
A.5	Experimental results	137

Chapter 1

The Human Eye: Structure, Pathologies, Challenges

The introduction of the visual system sparked the diversification of animal lifeforms and acted as a guiding force for evolution. Visual perception steered the development of offensive and defensive mechanisms, and facilitated interaction with the environment [Parker, 2003]. This evolutionary observation underlines the importance of sight, and corroborates the common knowledge that vision is one of the most, or perhaps even the most, important sense. Our world is built around visual information, and implications that hinder the individual's ability to see are a serious impediment to his quality of life.

Ophthalmology, derived from the greek words *οφθαλμός* (ofthalmos, eye) and *λόγος* (logos, speech), is the science that studies eyes, predicts and diagnoses pathologies, and suggests appropriate treatments. The eye contains the only part of the body's vasculature that is externally observable, and its physiology gives important insight in the health condition of the examinee. Ophthalmic observation has been practiced for centuries, and clinicians have the ability to acquire high-definition and magnified images of the interior of the human eye, using an ever-increasing variety of optical tools that are designed specifically for the unique optical system that is the human eye. Additionally, the wide breadth and continual evolution of surgical techniques in general ophthalmology and the ophthalmic subspecialties is staggering [Albert and Lucarelli, 2004].

1.1 The Anatomy of the Human Eye

The human eye is divided in three layers. It consists of an outer layer (the cornea and sclera), a middle layer (the iris, the choroid, and the ciliary body),

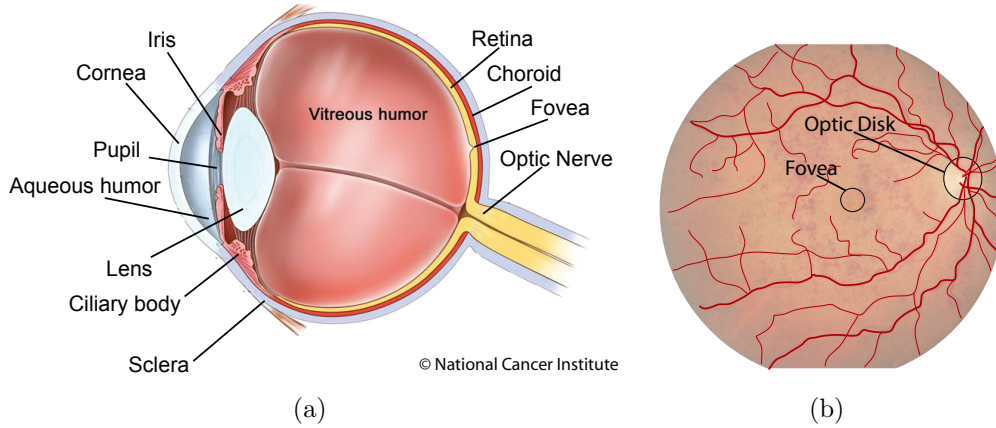


Figure 1.1: Schematics of (a) the human eye, and (b) the human-eye retina.

and an inner layer (the retina) [Atchison and Smith, 2000]. The exterior of the human eye consists of the cornea and sclera, and the interior of the eye holds the aqueous humor, the intraocular lens, and the vitreous humor. The different elements are annotated on Fig. 1.1.

The optical elements of the human eye that are responsible for image formation are the cornea, the aqueous humor, the pupil, the intraocular lens, and the vitreous humor. The cornea and the intraocular lens are the most important refractive elements, with the cornea having the greatest contribution to the overall refraction. The intraocular lens can change its power through a process called accommodation, enabling the eye to focus at both close and distant objects. Abnormalities in these optical elements adversely affect image formation.

The retina is the light-sensitive tissue of the human eye, and it contains the photoreceptors. At high light levels, the best resolution is attained at the fovea. Oxygenation of the retina is guaranteed through the choroid's vasculature, which enters the eye at the optic disk. At the optic disk, there are no photoreceptors and this area is a blind spot. Retinal pathologies deteriorate the perception of images.



Figure 1.2: (a) Image perceived by a healthy person, and (b) the same image perceived by a person with cataract.

1.2 Prevalent Ophthalmic Pathologies

The pathologies of the human eye deteriorate the formation of images by damaging the optical elements and the photoreceptors. The diseases impair sight, and can potentially lead to blindness. The percentage of people with visual impairments and blindness caused by infectious diseases is diminishing [World Health Organization, 2009], but diseases such as cataracts, glaucoma, age-related macular degeneration, and diabetic retinopathy still affect large percentages of the population and are even characterized as increasing threats [World Health Organization, 2010].

Cataracts are caused by the clumping of proteins in the intraocular lens, which leads to its clouding. Cataract obstructs the passage of light and results in blurry vision, poor night vision, faded color perception etc. (Fig. 1.2). Cataracts may lead to blindness if left untreated. In the United States in 2004, 20.5 million people older than 40 years old were reported to have cataract in either eye, and by 2020, the number of the affected population is expected to reach 30 million [Congdon *et al.*, 2004b]. Globally, age-related cataracts are responsible for 48% of the world blindness [World Health Organization, 2010]. Unfortunately, there is yet no comprehensive prevention of cataract development. The common treatment involves extracting the intraocular lens, usually after breaking it with high-frequency waves during a



Figure 1.3: (a) Image perceived by a healthy person, and (b) the same image perceived by a person with glaucoma.

process called phacoemulsification. The lens is replaced by an implant which stays in the eye permanently, restores sight, but is unable to accommodate. Cataract treatment is fairly straightforward, and blindness usually occurs due to lack of access to the necessary resources (e.g. trained personnel, clinics).

Glaucoma is a group of diseases in which the optic nerve is damaged. The most common case of glaucoma is open-angle glaucoma, which is caused by abnormal increase of intraocular pressure. An example of the effects of glaucoma can be seen in Fig. 1.3. In the United States, the affected population for open-angle glaucoma has been estimated at 2.47 million [Quigley and Vitale, 1997]. This number will increase to more than 3 million by 2020 [Friedman *et al.*, 2004b]. Worldwide, glaucoma is responsible for the blindness of 4.5 million people [World Health Organization, 2010]. As in the case of cataracts, there is little known about the prevention of glaucoma. However, if the disease is diagnosed in an early stage, it can be effectively treated and sight can be maintained. The challenge is to accurately monitor intraocular pressure. Common treatment consists of drug intake in the form of drops that can control eye pressure. Otherwise, liquid drainage can be accomplished with laser trabeculoplasty that helps fluid drain out of the eye. Another option is surgically creating an opening for the excess of fluid in the eye.

Age-related macular degeneration (AMD), contrary to glaucoma that usu-



Figure 1.4: (a) Image perceived by a healthy person, and (b) the same image perceived by a person with age-related macular degeneration.

ally affects peripheral vision, and cataract that affects the whole sight, results in loss of the central vision by the development of degenerative lesions in the macular area (the central retinal area) (Fig. 1.4). AMD is related with aging, affecting mostly people over 60 years old. An estimated 1.75 million American adults over 40 years old suffer from AMD, the number increasing to 7 million people with substantial risk of developing AMD [Friedman *et al.*, 2004a] in older ages. This makes AMD the leading cause of blindness, accounting for more than 50% of the cases of blindness [Congdon *et al.*, 2004a] of American people. Globally, it accounts for 8.7% of blindness cases [World Health Organization, 2010]. AMD can be treated with laser surgery that destroys the generated vessels, by photodynamic therapy, which involves the injection of drug in the circulatory system, and by intraocular injections. The challenge is to achieve localized drug delivery, and ideally, sustained release over time. Treatment can control the progress of the disease, but in many cases, vision deterioration is unavoidable.

Diabetic retinopathy (DR), like AMD, is also characterized by the formation of lesions on the retina. It affects people that have had diabetes mellitus for several years. DR is the result of vascular changes in the retinal circulation, leads to partial or full blindness (Fig. 1.5), and was estimated to account for about 5% of the worldwide cases of blindness [World Health Organization, 2010]. In the United States, around 4.1 million adults over 40



Figure 1.5: (a) Image perceived by a healthy person, and (b) the same image perceived by a person with diabetic retinopathy.

years old are affected by DR, with 8.2% having high vision-loss risks [Kempen *et al.*, 2004]. The disease can be controlled by monitoring the blood's sugar level. In advanced stages, it is treated by laser surgery that shrinks abnormal blood vessels. Table 1.1 shows the demographics of the discussed pathologies.

For all these diseases, prior to any surgical treatment, a vitrectomy needs to be performed. The vitreous humor of the human eye is occasionally opaque due to the eye condition. Moreover, it is a viscoelastic fluid that, through interaction with surgical tools, causes traction forces that potentially result in retinal detachments. For these reasons, it has to be removed as a first surgical step, and this removal process is called a vitrectomy. The interior of the eye is either filled with air, with salt solutions, or with oils, so that the intraocular pressure is kept constant.

1.3 Challenges in Ocular Surgery and Treatment

Cataract, glaucoma, age-related macular degeneration, and diabetic retinopathy, are within the group defined by the World Health Organization as priority eye diseases [World Health Organization, 2010] (see Table 1.1). Since their risk increases with age, given the increasing age of modern societies, the number of affected people is expected to rise sharply in the following years.

		Prevalent Pathologies	
		Cataract	Glaucoma
USA	Report	20.5 million (2004)	2.5 million (1997)
	Estimate	30 million (2020)	3 million (2020)
World	Report	48%	12%
	Studies	[Congdon <i>et al.</i> , 2004b] [World Health Organization, 2010]	[Quigley and Vitale, 1997] [Friedman <i>et al.</i> , 2004b]
		Age-related macular degeneration	Diabetic retinopathy
USA	Report	1.8 million (2004)	4.1 million (2004)
	Estimate	3 million (2020)	
World	Report	8.7%	5% (2002)
	Studies	[Friedman <i>et al.</i> , 2004a] [Congdon <i>et al.</i> , 2004a] [World Health Organization, 2010]	[Kempen <i>et al.</i> , 2004]

Table 1.1: Prevalence of major ophthalmic diseases.

Most of these diseases can be prevented through regular eye examination, and their progress can be controlled through surgery or drug delivery.

During vitreoretinal surgery the tools are inserted through the *pars plana*, the meeting point of the iris and the sclera on the ciliary body. Insertion through the *pars plana* guarantees that the tools will not damage the pupil or intraocular lens [Machemer *et al.*, 1972]. The cuts are performed using trocars, i.e. a surgical tool that keeps incisions open by use of a tube. The trocars penetrate the conjunctiva (a membrane protecting the sclera) and the sclera. The tools are inserted through cannulas fixed at the incisions.

Minimally invasive surgical approaches in ophthalmology result in reduced pain, reduced blood loss, and shorter hospitalization time. The minimally invasive approaches and the inaccessibility of the interior of the eye, however, give rise to a number of challenges [Hagn *et al.*, 2008]: (1) the tissue cannot be palpated, (2) the relatively high tool/trocar friction cannot be

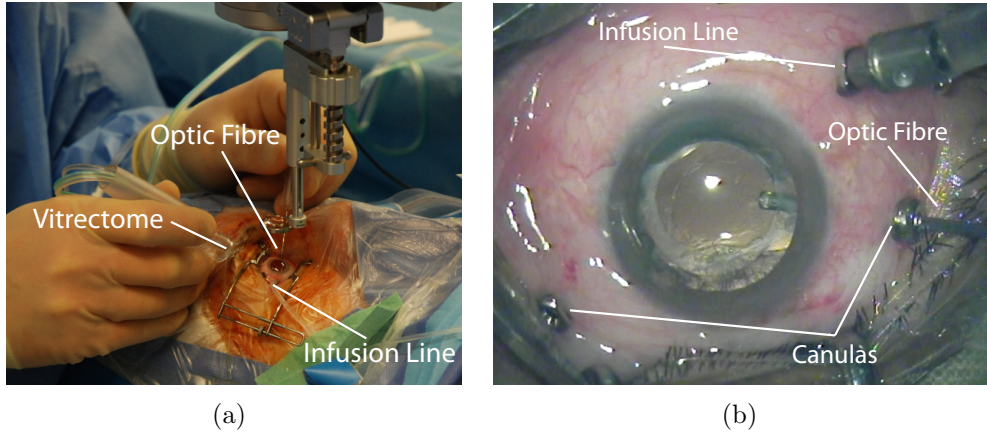


Figure 1.6: (a) Typical scene from the operating room, and (b) an example of a 23-gauge vitrectomy.

distinguished by tool/tissue interaction forces, and (3) as the instruments are moved through a single point, intuitive direct hand-eye coordination is lost. In ophthalmology, the small sizes of the affected structures and the robust drug clearance mechanisms of the human eye make treatment additionally challenging. The initial requirement for a vitrectomy further complicates procedures.

Twenty-gauge vitrectomy is the current gold standard in ophthalmic surgery [Albert and Lucarelli, 2004]. It involves performing 0.9 mm incisions on the *pars plana*. Three incisions are usually required: one for the cutter, one for the infusion line that keeps the intraocular pressure constant, and one for the illumination fibre (Fig. 1.6). Together with the fact that the vitreous is dissected and aspirated, the multiple incisions indicate opportunities for improving patient comfort. Towards this goal, 23-gauge vitrectomy is increasingly gaining acceptance. It offers similar cutting, aspiration, and infusion rates as the 20-gauge counterpart, and can potentially be performed with topical anesthesia, and without requiring post-operative suturing [Albert and Lucarelli, 2004; Theocharis *et al.*, 2007]. The next step is 25-gauge vitrectomy, which would enable access to the vitreous chamber without requiring conjunctival peritomy.

In addition to the skills needed for a vitrectomy, retinal surgery requires

even more precise movements and small tool/tissue interaction forces, since the retina is a delicate structure that is at risk of permanent damage and vision loss through even small surgical errors. Certain retinal procedures can only be physically performed by a limited set of surgeons. As [Gupta *et al.*, 1999] determined, only approximately 20% of contact events between the surgical tool and the retinal tissue during retinal microsurgery can be felt by a surgeon. This indicates that the majority of retinal surgery is probably performed without force feedback. A similar study in [Jagtap and Riviere, 2004] corroborates that the forces involved in retinal surgery are at or beyond the limits of human perception. Moreover, as that study showed, the forces experienced due to the tool/sclera interaction are much greater than the forces due to the interaction with the retina, further undermining the sense of haptic feedback. Reliance mainly on visual feedback increases the duration of the manipulation task and reduces accuracy, making procedures such as retinal-vein cannulation extremely demanding and risky.

Concerning drug administration, current delivery methods are suboptimal in delivering high drug quantities in a localized fashion. In [Li *et al.*, 2008], ocular drug diffusion is studied *in vivo* for various cases of drug administration. It was found that for the most common treatment, topical administration, less than 7% of the administered drug passes the ocular barriers. Furthermore, systemic drug administration, i.e. drug delivery through the circulatory system, another common route for posterior eye treatment, may cause toxic side effects on non-target tissues [Yasukawa *et al.*, 2004]. Thus, the challenge in intraocular drug delivery is to deliver the medicine at the problem's location without risking retinal detachments, tears, or other injuries due to the needle/vitreous traction forces. Moreover, controlled/sustained release systems are preferable, as they can increase the treatment time without the need of repeated injections. Different drug delivery methods are illustrated in Fig. 1.7. In Fig. 1.8, the MRI images show the difference in drug diffusion for the different cases, and make clear that only intravitreal drug delivery can satisfy the patients' needs.

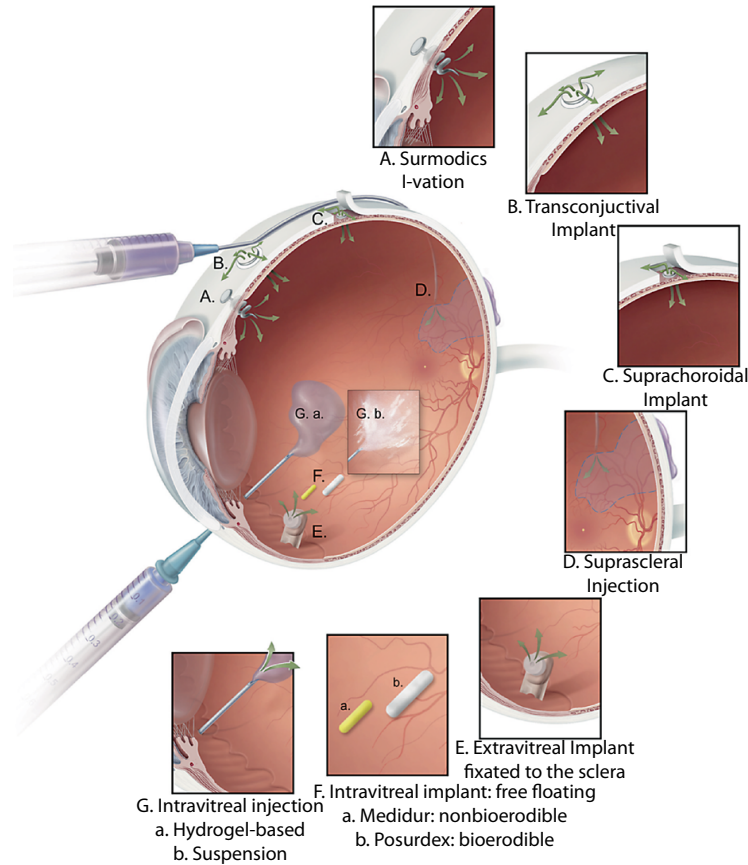


Figure 1.7: Different methods for intraocular drug delivery (from [Lee and Robinson, 2009]).

1.4 Conclusions

An increasingly large portion of the human population will suffer from an eye disease in the near future, rendering the affected people seriously handicapped. Widespread eye diseases affect also citizens of the modern world, and are not connected with infectious diseases. Current methods to estimate the progress of the different pathologies are usually limited to intraocular observation, and clinicians are unable to perform the needed intraocular measurements. Moreover, the dexterity that is required for the successful completion of a number of retinal treatments is only available to a limited set of skilled surgeons. Lastly, the existing methods of intraocular drug delivery need to

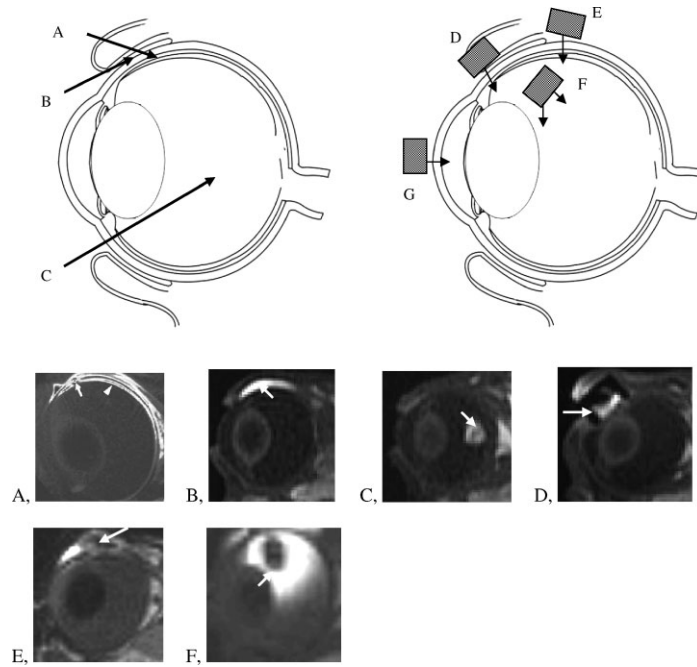


Figure 1.8: (a) Examples of drug-delivery methods studied using MRI: A, intrasceral infusion or injection into the suprachoroidal space; B, subconjunctival injection; C, intravitreal injection; D, transscleral iontophoresis; E, episcleral implant; F, intravitreal implant; G, transcorneal iontophoresis. (b) Representative MR images of ocular drug delivery in rabbits: A, intrasceral infusion; B, subconjunctival injection; C, intravitreal injection; D, ocular iontophoresis; E, episcleral implant; F, intravitreal implant. The arrows indicate the sites of drug delivery or the drug-delivery systems. Image taken from [Li *et al.*, 2008].

be reexamined, since the most common administration methods are either risky, or produce unsatisfactory results.

Towards the final goal of increasing treatment effectiveness, and reducing surgery time and patient recovery time, new tools and methods need to be introduced. Robot-assisted systems can augment the capabilities of human surgeons, assist in intraocular sensing, and provide the desired solutions.

Chapter 2

Robotic Solutions for Ophthalmology

Many systems that aid ophthalmic surgeons in their intricate tasks have been proposed, and robot-assisted solutions for ophthalmology is an emerging research topic.

The systems being developed can be classified in many ways. They can be considered as surgeon extenders ([Taylor and Stoianovici, 2003]) in which the surgeon controls the robotic tool directly, and the robot guarantees appropriate interaction forces and motions. They can be classified as master/slave systems, where the master, which is directly controlled by a surgeon, controls a slave robotic system that performs the actual surgery. The robots can also be fully automated, leaving the surgeon completely out of the loop. They can be active systems that perform an invasive task, or passive systems that perform only sensing. Additionally, surgical robotic assistants can be classified based on their dimensions. A review on microrobotic systems can be found in [Nelson *et al.*, 2010]. Larger surgical robotic assistants are covered in [Hager *et al.*, 2008] and [Dogangil *et al.*, 2010].

2.1 Surgeon Extenders

Surgeon extenders are collaborative robots that operate under surgical supervision. Usually they are tools that are directly controlled by the surgeon and enable him to perform operations with greater dexterity by providing haptic feedback, canceling the hand tremor, or guaranteeing that the tool follows a predefined path. This approach is easily acceptable by surgeons, since they can exercise the skills they have cultivated through training, but they can also enhance those skills. Moreover, it allows them to keep supervisory control of the entire surgical procedure.

In this spirit, in 1998, a group from Nagoya University modified the for-

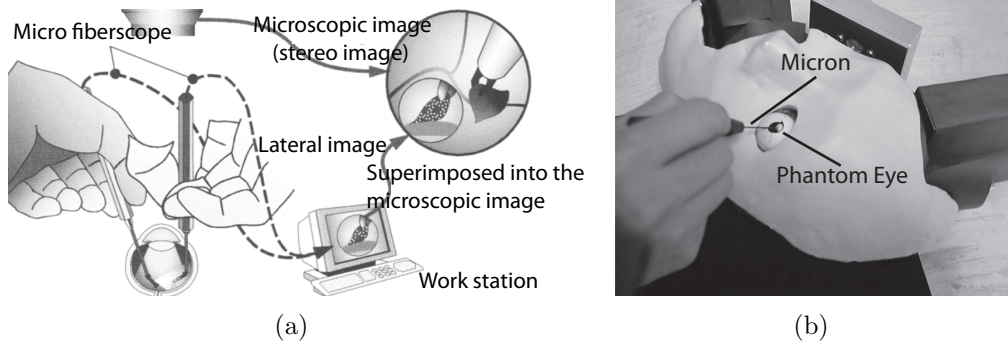


Figure 2.1: (a) The micro-active forceps with built-in fiberscope introduced by Nagata *et al.*, and (b) the Micron introduced by Riviere *et al.*. Images taken from [Ikuta *et al.*, 1998] and [Riviere *et al.*, 2003], respectively.

ceps that are commonly used in retinal microsurgery by adding a joint that enables their end-effector to approach the target tissue from different angles. Additionally, a fiberscope for close-up views of the manipulated tissue was included. The images from the fiberscope complement the existing view through the cornea (Fig. 2.1(a)). The device was optimized numerically, and its maneuverability was tested in porcine eyes [Ikuta *et al.*, 1998].

A technique that accounts for the physiological hand tremor that limits the precision of microsurgions was introduced in [Riviere *et al.*, 1998]. Researchers modeled the tremor online and created piezoelectric actuators that move the tooltip in opposition to the tremor, effectively subtracting the tremor from the total motion. They demonstrated the tool’s capabilities in a single dimension, and introduced the “Micron” [Riviere *et al.*, 2003], a microsurgical tool that uses this tremor compensation technique in three dimensions. Micron was used in [Becker *et al.*, 2009b] in a simulated laser photocoagulation scenario and was coupled with a visual system in [Becker *et al.*, 2009a], allowing it to be operated under different assistive modes (e.g. snap-to-vein).

A group from Johns Hopkins University introduced the “Steady Hand Robot” in 1999 [Taylor *et al.*, 1999]. This robot is directly controlled by the surgeon, and senses the surgeon/tool and tool/environment interaction forces. It uses this information to provide smooth, tremor-free, precise po-

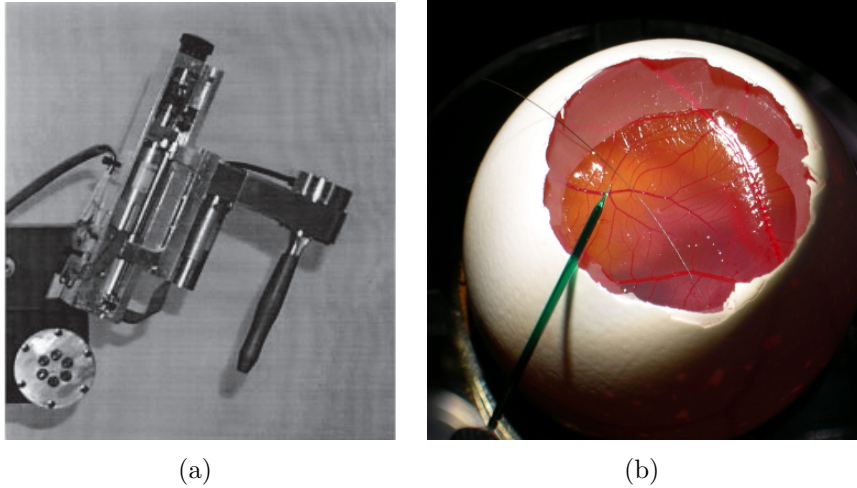


Figure 2.2: (a) A prototype of the Johns Hopkins Steady Hand robot, and (b) its application in CAM vein cannulation. Images taken from [Taylor *et al.*, 1999] and [Mitchell *et al.*, 2007], respectively.

sitional control and force scaling. The researchers' goal was to develop a manipulation system with the precision and sensitivity of a machine, but with the manipulative transparency of handheld tools. Preliminary feasibility experiments in [Kumar *et al.*, 2000] demonstrated stable one-dimensional robotic augmentation and force-scaling of a human operator's tactile input. The Steady Hand Robot was additionally coupled with virtual fixtures ([Betini *et al.*, 2004]) aiming to augment the capabilities of ophthalmic surgeons by enforcing unreachable regions on the retina [Dewan *et al.*, 2004]. The system's effectiveness was demonstrated in [Mitchell *et al.*, 2007] through successful cannulation of $80\ \mu\text{m}$ veins on the chorioallantoic membrane of a chicken embryo. Figure 2.2 shows the Steady Hand Robot, and its application on a phantom eye.

2.2 Teleoperated or Autonomous Robots

One of the first teleoperated systems for microsurgery on the retina was presented in [Jensen *et al.*, 1997]. The proposed manipulator provided sub-micrometer positioning of an instrument within the constrained environment

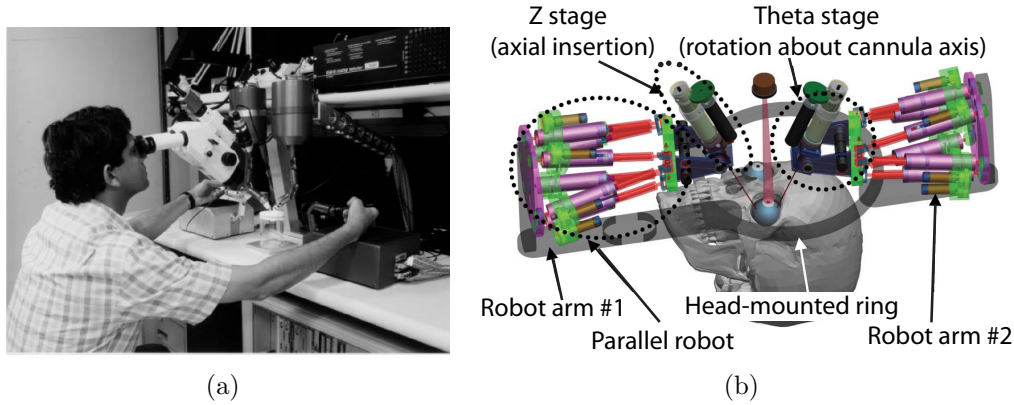


Figure 2.3: (a) The master/slave robotic system developed at JPL, and (b) the multi-arm system from Columbia University. Images taken from [Das *et al.*, 2001] and [Wei *et al.*, 2009], respectively.

of the eye. The goal was to account for the tremor and fatigue of the human surgeon. The position of the instrument was controlled using a hand-held trackball, and the researchers evaluated their system by performing cannulation on retinal veins.

In the Jet Propulsion Laboratory of the California Institute of Technology, a similar approach that led to a different master/slave system for ophthalmic surgery was pursued. The user controlled the master robot in multiple degrees of freedom, and the motion was translated to motion of the slave robot (Fig. 2.3(a)). Within the end-effector of the slave robot a force sensor that provided haptic feedback to the surgeon was implemented. The researchers demonstrated the use of a dual system that can assist in microsuturing [Das *et al.*, 2001].

Simaan *et al.* presented the design considerations and dexterity evaluation of a hybrid two-arm microsurgical robot [Wei *et al.*, 2007]. Rather than a straight needle, the robot's end-effector consists of pre-curved flexible tubes that give increased dexterity by increasing the degrees of freedom normally provided in intraocular surgery from four to five. Their theoretical analysis resulted in a kinematics framework that took into account the constraints from the motion of the eye. The capabilities of this two-armed robot in

performing dexterous intraocular operations were evaluated and compared to a similar robot without intraocular dexterity, showing superior behavior. In [Wei *et al.*, 2009], the researchers extended their considerations for cases covering multi-arm manipulation of hollow suspended organs. A schematic of their system is shown in Fig. 2.3(b).

All the aforementioned systems share four basic attributes:

1. They use a tool that is passed through the sclera and must perform constrained motions so that the sclera is not damaged during surgery. This scleral interaction places limits on dexterity.
2. They are fundamentally position-controlled devices, with any force control being accomplished by closed-loop force feedback, either in the form of force sensing or in the form of visual feedback of the interaction of the tool with the retina. The retina is still at risk from a tool that is capable of causing irreparable damage in the event of patient movement or system failure.
3. They require a vitrectomy to be performed to allow movement of the tool and to avoid retinal traction.
4. The tools are approximately the same size as those used during manual surgery. Consequently, the invasiveness of the procedure is not necessarily reduced through robotic assistance.

2.3 Microrobotic Systems

A different approach involves using microrobotic agents in surgery. Instead of enhancing tools or using optimized robotic arms, [Yeşin *et al.*, 2006] introduced a wireless magnetic microrobot for use in ophthalmic surgeries. Figure 2.4(a) shows a microrobot consisting of microfabricated elliptical plates that are microassembled into an “ellipsoidal” device. Microrobots can be inserted with a needle through the *pars plana* region of the sclera, and can be wirelessly controlled to the location of interest under teleoperation or supervisory control of a clinician. After performing their tasks, they can be driven closer to the initial insertion point for removal by a magnetic tool.

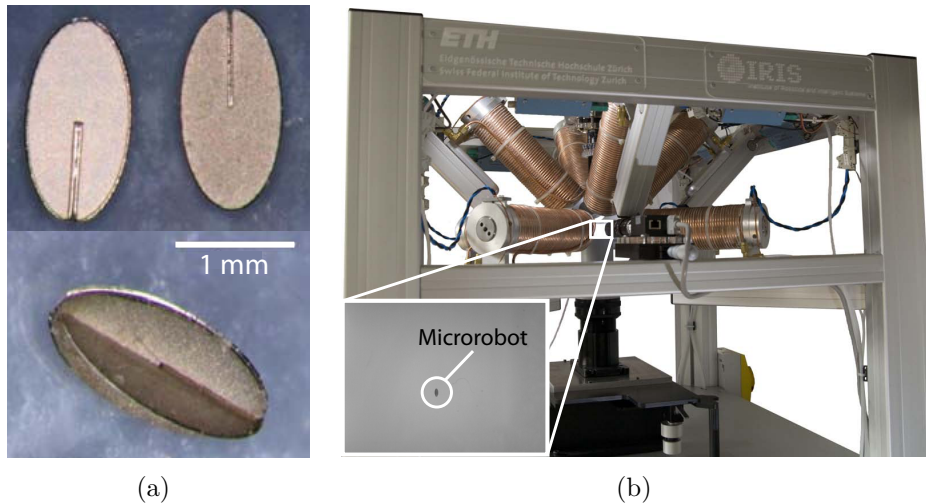


Figure 2.4: (a) A $2\text{ mm} \times 1\text{ mm} \times 1\text{ mm}$ CoNi ellipsoidal microrobot and its individual components, and (b) the OctoMag electromagnetic control system. The inset shows a $500\text{-}\mu\text{m}$ -long microrobot levitating in a chamber. Images taken from [Nagy *et al.*, 2008] and [Kummer *et al.*, 2010], respectively.

In the previous chapter it was mentioned that 23-gauge vitrectomy does not require post-operative suture; a microrobot that can fit in the same 23-gauge trocar can be thought of as truly minimally invasive. Nelson *et al.* from ETH Zurich introduced the OctoMag in [Kummer *et al.*, 2010], which is an electromagnetic control system capable of full five degree-of-freedom manipulation of magnetic devices (Fig. 2.4(b)). The OctoMag consists of eight electromagnets with soft-magnetic cores. The electromagnets are positioned in a hemispherical array, and they are capable of manipulating devices as small as $500\text{ }\mu\text{m} \times 250\text{ }\mu\text{m} \times 250\text{ }\mu\text{m}$, which fit in a 23-gauge syringe.

Intraocular microrobots can be made biocompatible by surface coatings [Dogangil *et al.*, 2008], and have the potential to be used for ophthalmic procedures ranging from targeted drug delivery to retinal vein cannulation and remote sensing. Recently, localized intravitreal administration is gaining interest [Yasukawa *et al.*, 2004; Lee and Robinson, 2009] as an alternative to transscleral drug delivery, which is less efficient due to the robust drug clearance mechanisms of the eye. In [Yasukawa *et al.*, 2004], biodegradable and non-biodegradable polymers that act as drug carriers are compared, with the

latter ones exhibiting a more controlled drug release. Moreover, in [Dogangil *et al.*, 2008; Ergeneman *et al.*, 2008a] the devices themselves are coated with the anticoagulant drug t-PA, and this technique is an alternative to retinal-vein cannulation as a therapy for retinal-vein occlusions. In [Kummer *et al.*, 2010] it was shown that the OctoMag can exert the forces necessary for retinal-vein cannulation by puncturing veins on the chorioallantoic membrane of a chicken embryo. As a result, the microrobots can be docked on retinal veins, and the drug from the microrobot's surface can diffuse into the retinal vasculature. The exact quantity of drug needed to successfully start clot dissolution is not yet known.

Another benefit of the microrobotic approach is that different type of agents can be used. In addition to ellipsoidal microrobots, hollow magnetic devices can be used as drug carriers. These devices would potentially require a vitrectomy, but helical swimmers such as those in [Zhang *et al.*, 2009], which can also be controlled with the OctoMag, have the potential to cut through the vitreous like a screw. The relative motion of the microrobot in the vitreous may not result in retinal traction.

In [Holligan *et al.*, 2003], fluids containing magnetic nanoparticles were proposed to repair retinal detachments. Pulling on these nanoparticles would make them act as a tamponading agent on the detached retina. These magnetic nanoparticles have to be proven nontoxic to the retina, however. The technology developed at the ETH Zurich could be used to steer such magnetic fluids as well.

2.4 Sensing Technologies

A passive implantable parylene MEMS system for glaucoma therapy was developed in [Meng *et al.*, 2005; Chen *et al.*, 2006]. The developed technology can provide pressure sensing and act as a drainage shunt, enabling both the detection and alleviation of elevated intraocular pressure. Tissue anchors for securing the pressure sensor on the iris were developed in an effort to facilitate direct optical monitoring of the intraocular pressure. Additional experiments reported in [Chen *et al.*, 2008] demonstrate good pressure sen-

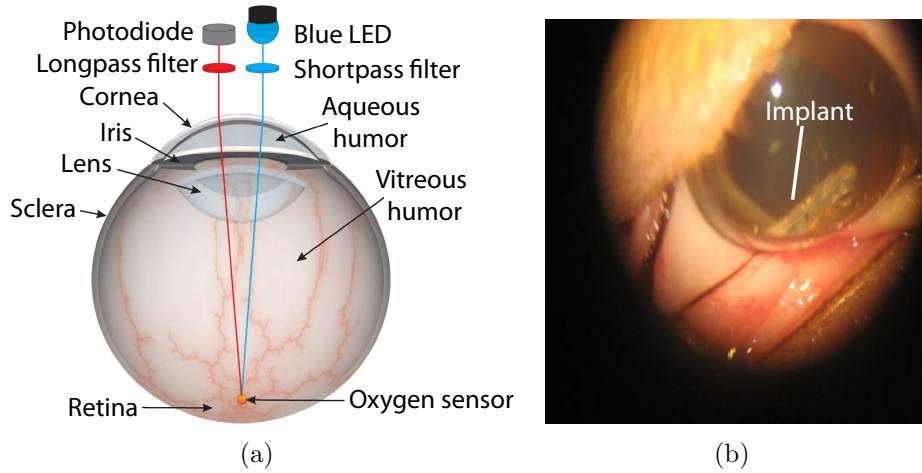


Figure 2.5: (a) An implantable MEMS oxygen-pressure sensor, and (b) luminescence-quenching-based oxygen sensing. Images taken from [Ergeneman *et al.*, 2008b] and [Chen *et al.*, 2008], respectively.

sitivity, and resolution. The biocompatibility of the device was successfully verified through *in vivo* animal studies (Fig. 2.5(b)), showing that this device can be used for long-term monitoring of glaucoma patients. The conclusive report of this research can be found in [Chen, 2008].

Microdevices can be coated with polymers and enable the measurement of oxygen levels in the retinal area [Ergeneman *et al.*, 2008b] (Fig. 2.5(a)). Their sensing works based on quenching of luminescence in the presence of oxygen, and uses a novel iridium phosphorescent complex coating. A frequency-domain half-life measurement approach is employed because of the intrinsic nature of the lifetime of luminescence. The half-life is dependent on the oxygen concentration at the position of the device. The magnetic sensors can be controlled with the OctoMag or another electromagnetic control system, enabling the extraction of oxygen maps for the posterior eye segment.

2.5 Problem Statement

After having examined the engineering problems in ophthalmic surgeries and the existing solutions, we conclude that robotic systems should be capable of undertaking multiple roles in minimally invasive ophthalmic surgeries;

they should enable localized drug delivery in the posterior eye segment, and should safely operate in the small scales of the retinal vasculature.

The microrobotic technology developed at ETH Zurich can assume such roles. Enabling ophthalmic surgeries with magnetically-guided wireless microrobots is the motivation behind this dissertation. More specifically, ensuring the stability of these devices during surgery is a fundamental driver for this research.

Earnshaw's theorem states that there can be no stable static equilibria using ferromagnetism [Cullity and Graham, 2009]. To maintain a "stable" position of a magnetic microrobot, in other words to minimize its drift, position feedback is required to calculate the magnetic field at the robot's position. In order to control magnetic devices, localization information is required [Abbott *et al.*, 2007; Nagy *et al.*, 2008]. In addition, the microrobot needs to be servoed to specified locations.

Contrary to handheld instruments and master robotic systems that can use proprioception for the localization of the end-effector, such information cannot be intrinsically supplied for untethered devices. Additionally, microrobots do not possess sensors that can assist in this task, contrary to, for example, unmanned aerial vehicles. Since the interior of the human eye is observable with an ophthalmoscope, position information in the case of intraocular devices can be obtained by computer vision algorithms. The development of such algorithms is the primary topic of this thesis.

A significant advantage of these microrobotic devices is to enable truly minimally invasive procedures by eliminating the requirement for a vitrectomy. This thesis investigates the ability to move microdevices through the vitreous using gradient forces. Our investigation is supported by *in vitro* experiments with synthetic vitreous humors, and *ex vivo* experiments with cadaver porcine eyes.

Chapter 3

Imaging Intraocular Microdevices

The interior of the human eye is externally observable through the pupil using a variety of methods and ophthalmoscopes that were developed specifically for intraocular observations. The imaging systems, the cornea, aqueous humor, pupil, intraocular lens, and vitreous humor alter the observed field-of-view and affect the formation of images. Figure 3.1 shows the effect of a lens that mimics the optics of the human eye on the perceived image. Objects appear closer and magnified.

Existing work in computer vision attempts to understand this image formation process and estimate the three-dimensional structure of the human retina. One of the first publications in the field, [Deguchi *et al.*, 2000], approximated the eye optics and the fundus camera optics with a single unknown lens. They treated the human retina as a sphere and performed a minimization to estimate the parameters of the sphere and of the unknown lens equivalent from stereo images. Treating the cascade of lenses as a single lens implies the use of paraxial approximations that, as we will see, are not sufficient for considering a wide field-of-view.

[Liu *et al.*, 2009] also suggested treating the cascade of optics as a single lens, and using the correspondences between images to perform auto-calibration on the full optical system. The motion between the camera and the eye was kept minimal to satisfy the assumption that the intrinsic parameters remain constant. Their algorithm was only tested on a cylindrical surface, without any refractive optics to alter the image formation. Auto-calibration is also considered in [Espinosa-Romero and Martinez-Perez, 2005].

In [Lin and Medioni, 2008], the authors perform a four-pass bundle adjustment based on extracted features, initially assuming a flat retinal surface. Even though their method converges to smooth surfaces, there is no account

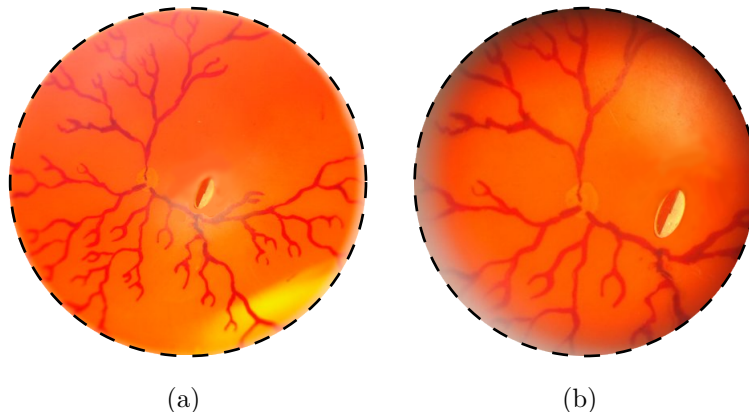


Figure 3.1: The biomedical microrobot of [Yeşin *et al.*, 2006] in a model eye [Gwb International, Ltd., 2010]. The image on the left is the image of the intraocular environment without the optical elements, and the image on the right shows the effect of the model eye optics. Images are taken with a simple digital camera.

for the alteration of the retinal surface by the eye optics. Tomasi-Kanade factorization [Tomasi and Kanade, 1992] and bundle-adjustment is the preferred method in [Chanwimaluang *et al.*, 2009], where the authors do take into account non-linear lens distortions in their minimization.

The variety of approaches shows that there is no consensus as to how the image formation should be modeled, and different groups undertake different methods that are not always consistent. Contrary to the aforementioned work, we are additionally interested in objects that move in the posterior of the human eye, and not only on the retina. Thus, our first step towards intraocular localization needs to be the examination of the image formation of intraocular devices. This chapter examines existing methods of intraocular observation to realize whether there exist preferable ophthalmoscopy techniques, and to understand the advantages and disadvantages of each technique with respect to intraocular device localization.

In order to avoid potential conflicts between the imaging system and the electromagnetic-field-steering system, we would ideally perform imaging with a stationary camera. Allowing motions of the optical system along its optical

axis for image focusing is an acceptable exception. Stereo-ophthalmoscopy is not considered; the discrepancies given by a stereo system still need to be “translated” to depth estimates. This is not intuitive for systems composed of multiple refractive elements, and involves the understanding of image formation as well.

3.1 Comparison of Ophthalmoscopy Methods

Our results are based on Navarro’s schematic eye [Escudero-Sanz and Navarro, 1999]. A schematic eye is an optical model based on biometric data that explains the optical properties of the human eye to a good approximation, contrary to simplified older eye models like the one in [Gullstrand, 1909] that are good only for a limited field-of-view. Navarro’s schematic eye performs well for angles up to 70° measured from the center of the pupil and around the optical axis. For greater angles, the biometric data of each patient should be considered individually. The pupil diameter in [Escudero-Sanz and Navarro, 1999] is 3 mm. The object’s depth is measured along the optical axis. We begin by investigating the feasibility of imaging and localizing intraocular devices using existing ophthalmoscopy methods. For our simulations, we will initially consider only the relaxed (or paralyzed) lens of an emmetropic eye, which focuses parallel incoming rays on the retina. Our optical simulations are performed with OSLO (Optical Lens Design Software), and results are processed with Matlab.

OSLO [Lambda Research Corporation, 2010] is a numerical simulation program that is tailored for optical systems. It enables the quick introduction of optical elements, raytracing, calculation of point-spread functions, modulation transfer functions etc., and, generally, it provides tools for thorough investigation and optimization of optical systems.

The first ophthalmic observation approach involves looking directly into the human eye, and is analogous to direct ophthalmoscopy. The second approach involves the utilization of vitrectomy contact lenses. Finally, we consider the use of a non-contact condensing lens. This method is analogous to indirect ophthalmoscopy.

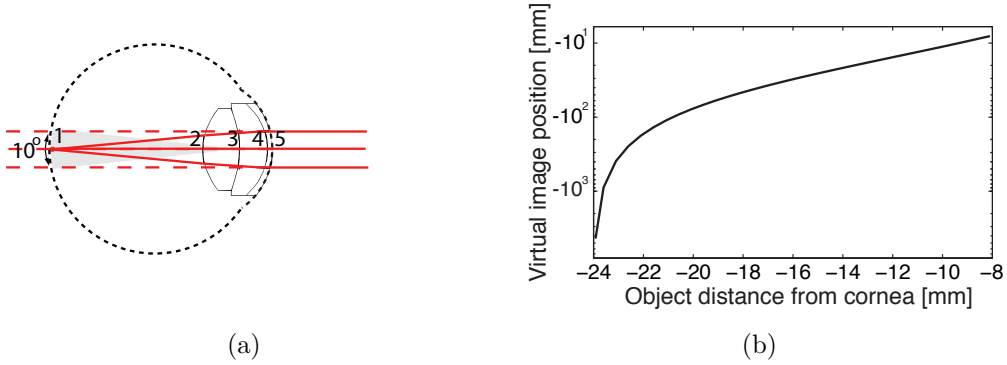


Figure 3.2: (a) Navarro's schematic eye, and (b) virtual image position versus intraocular object position (image distances are measured from surface 5).

Surface	Radius	Conic Constant	Thickness	Refractive Index
1	12.00 mm	0.00	16.32 mm	1.336
2	6.00 mm	-1.00	4.00 mm	1.420
3	-10.20 mm	-3.13	3.05 mm	1.337
4	-6.50 mm	0.00	0.55 mm	1.376
5	-7.72 mm	-0.26	∞	1.000

Table 3.1: Optical parameters for the system of Fig. 3.2(a)

3.1.1 Direct Ophthalmoscopy

In a relaxed state, the retina is projected through the eye optics as a virtual image at infinity. The parallel beams can be captured by an imaging system, and the image of the retina is created. In direct ophthalmoscopy—the simplest method of intraocular observation—the rays are brought in focus on the observer's retina [Snead *et al.*, 1992]. Using the formulas of [Smith and Atchison, 1997], we can calculate the field-of-view for direct ophthalmoscopy at $\sim 10^\circ$ (Fig. 3.2(a)). The optical parameters for direct ophthalmoscopy can be found in Table. 3.1.

Every object inside the eye will create a virtual image. These virtual images approach infinity rapidly as the object approaches the retina. Figure 3.2(b) displays the distance where the virtual image is formed versus different positions of an intraocular object. In order to capture the virtual images that are created from objects close to the retina, an imaging system with

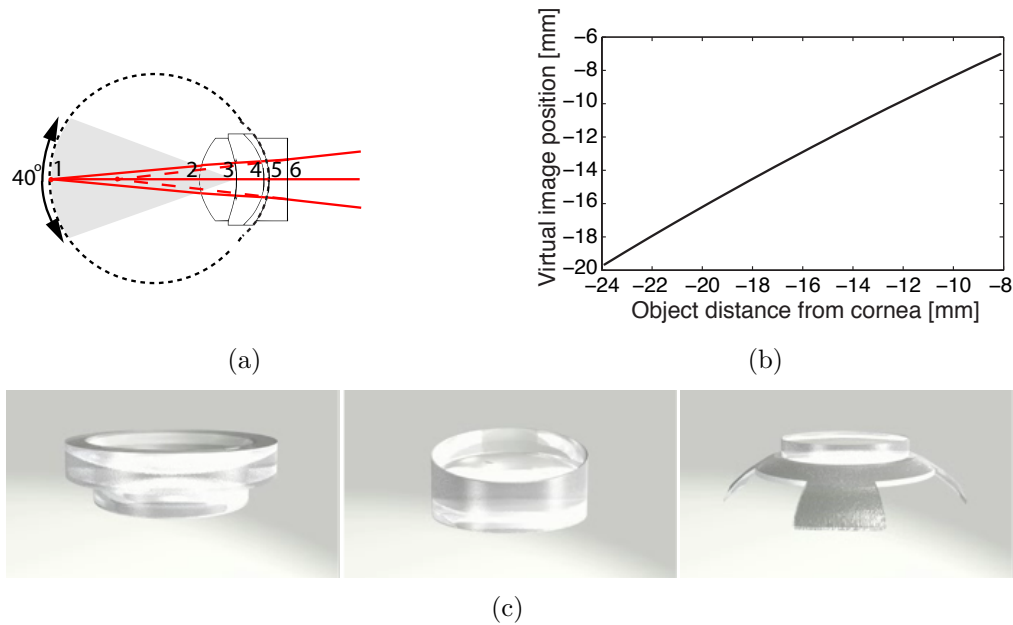


Figure 3.3: (a) Navarro's schematic eye with a vitrectomy lens [HUCO Vision, 2008], (b) virtual image position versus intraocular object position for the vitrectomy case (image distances are measured surface 6), and (c) commercial vitrectomy lenses (images from www.volk.com).

an approximately infinite working distance and depth-of-field is required. Imaging with an optical microscope is impossible due to its limited working distance.

3.1.2 Vitrectomy Lenses

To visualize objects in the vitreous humor of patients, a variety of contact lenses can be used. For robotic agents that operate in the vitreous humor of phakic (i.e. with intact intraocular lens) eyes, only the use of plano-concave lenses (Fig. 3.3(a)) needs to be considered [Snead *et al.*, 1992]. Figure 3.3(c) shows commercial vitrectomy lenses.

Vitrectomy lenses increase the field-of-view (up to 40°), attenuate the virtual images formed by the eye optics, and position them inside the eye. The virtual images are subsequently captured by an additional imaging system. Larger lenses capture more rays that escape the pupil by limiting vignetting

Surface	Radius	Conic Constant	Thickness	Refractive Index
1	12.00 mm	0.00	16.32 mm	1.336
2	6.00 mm	-1.00	4.00 mm	1.420
3	-10.20 mm	-3.13	3.05 mm	1.337
4	-6.50 mm	0.00	0.55 mm	1.376
5	-7.72 mm	-0.26	2.00 mm	1.425
6	∞	0.00	∞	1.000

Table 3.2: Optical parameters for the system of Fig. 3.3(a)

Surface	Radius	Conic Constant	Thickness	Refractive Index
1	12.00 mm	0.00	16.32 mm	1.336
2	6.00 mm	-1.00	4.00 mm	1.420
3	-10.20 mm	-3.13	3.05 mm	1.337
4	-6.50 mm	0.00	0.55 mm	1.376
5	-7.72 mm	-0.26	2.31 mm	1.000
6	11.65 mm	-9.24	13.00 mm	1.523
7	-9.48 mm	-1.07	∞	1.000

Table 3.3: Optical parameters for the system of Fig. 3.4(a)

and increasing the field-of-view. Vitrectomy lenses result in virtual images that span a shorter distance than in direct ophthalmoscopy, allowing the imaging system to have a shorter working distance and depth-of-field.

Based on data given from HUCO Vision SA for the vitrectomy lens S5.7010 [HUCO Vision, 2008], which are shown in Table. 3.2, we simulated the effects of a plano-concave vitrectomy lens on Navarro’s eye. As shown in Fig. 3.3(b), the virtual images are formed inside the eye and span a lesser distance than in direct ophthalmoscopy. Thus, contrary to direct observation, imaging with an optical microscope (short working distance and depth-of-field) is possible. The working distance of such an imaging system must be at least 20 mm in order to capture the virtual images that are formed by the retina.

3.1.3 Indirect Ophthalmoscopy

Indirect ophthalmoscopy uses condensing lenses that create an aerial image of the surface of the retina (Fig. 3.4(a)). Figure 3.4(c) shows different commercial condensing lenses.

Contrary to other ophthalmoscopy methods, indirect ophthalmoscopy al-

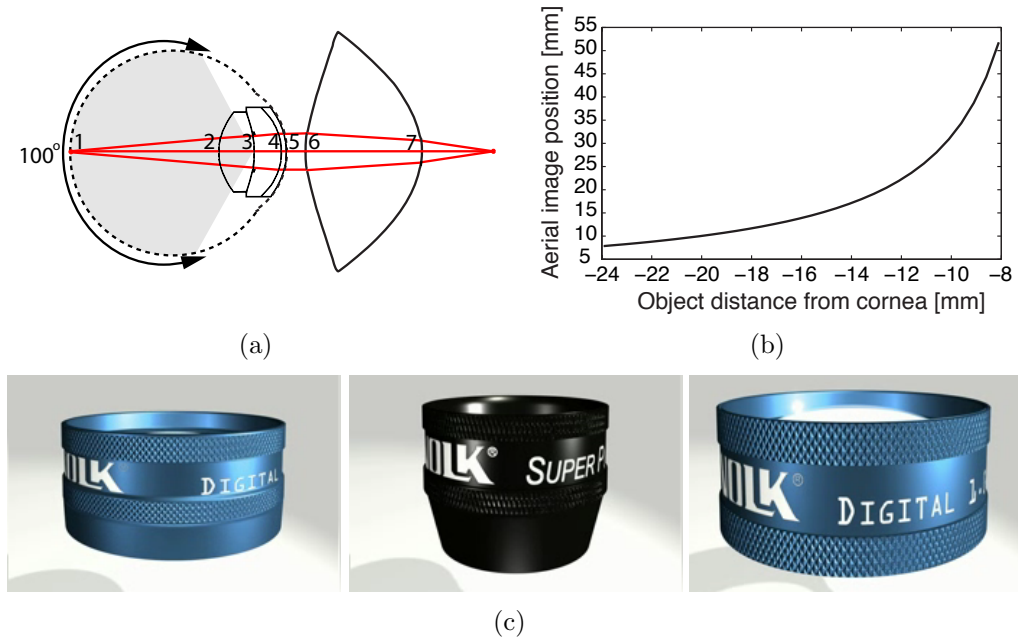


Figure 3.4: (a) Navarro's schematic eye with a condensing lens [Volk, 1998], (b) aerial image position versus intraocular object position for the indirect ophthalmoscopy case (image distances are measured from surface 7), and (c) commercial indirect ophthalmoscopy lenses (images taken from www.volk.com)

allows a wide field-of-view (up to 100°) to be observed. The field-of-view is governed by the refractive index and the shape of the lens' surfaces, by the diameter of the lens itself, and its position with respect to the cornea. Due to vignetting, there are always some rays that escape the eye that are not captured by the lens, thus limiting the maximum achievable field-of-view. Due to the non-contact nature of these lenses, they are usually preferable by surgeons and patients. State-of-the-art condensing lenses and their design considerations are discussed in [Volk, 1998].

From simulations of a system composed of Navarro's schematic eye and a condensing lens (parameters in Table. 3.3), the aerial image position versus the on-axis object position can be estimated (Fig. 3.4(b)). Because of the large field-of-view, non-contact nature, and aerial image formation that enables an arbitrary choice of working distance, indirect ophthalmoscopy is

the preferred method for imaging intraocular microdevices.

3.2 Wide-Angle Image Formation

Until now, our examination of image formation was limited to on-axis. This was sufficient for an impression of the differences of the most basic ophthalmoscopy cases, but does not sufficiently describe the image formation of intraocular devices moving over a wide-angle.

The first approach in examining optical cascades off-axis is to employ first-order (paraxial) approximations for the simplification of the optical system. Paraxial approximations are based on two assumptions: (1) planar objects project into planar images, and (2) the angles between the optical axis and the incoming rays are small.

The human eye cannot be sufficiently examined in a wide-angle using paraxial approximations, because none of the aforementioned assumptions hold. The first assumption is violated because extraocular planar objects are projected on the curved surface of the retina, and, due to inverse light path and the homogeneity of the vitreous humor, we can safely assume that planar objects in the eye will be projected as curved images extraocularly. The second assumption is violated because we want to examine image formation over a large angle, and we cannot assume small angles with the optical axis.

As a result, in order to take into account the full field-of-view that indirect ophthalmoscopy offers, one must go beyond simple paraxial models. We propose a method that is based on raytracing on an optical model of the human eye that can be constructed preoperatively. Methods to extract individual eye parameters are described in [Mejia-Barbosa and Malacara-Hernandez, 2001; Kirschkamp *et al.*, 2004]. Recently, a method that creates personalized eye models from biometric measurements was proposed [Navarro *et al.*, 2006].

The analysis that follows considers a simple imaging system consisting of a condensing lens that creates an aerial retinal image with low curvature. The condensing lens is composed of one aspheric surface and one pure conic surface (Table. 3.4, and Fig. 3.5). The aspheric components were estimated through an iterative procedure that reduced the image's field curvature, for

Surface	Posterior	Anterior
Radius of Curvature [mm]	11.65	-9.48
Conic Constant	-9.24	-1.07
a ₄	4.078 × 10 ⁻⁵	0.0
a ₆	-1.542 × 10 ⁻⁷	0.0
a ₈	-2.647 × 10 ⁻⁹	0.0
a ₁₀	2.023 × 10 ⁻¹¹	0.0
Thickness (mm)	13.00	∞
Refractive Index	1.523	1.000

Table 3.4: Optical parameters for the condensing lens of Sec. 3.2

a field-of-view of 60° to 70°. Since Navarro’s eye is valid for a field-of-view up to 70°, it is not necessary to optimize the condensing lens for a greater field-of-view. The initial lens’ parameters were taken from [Volk, 1998] based on the requirement for a flat aerial retinal image with a high field-of-view. The surfaces of the condensing lens are given by the equation:

$$x = \frac{\frac{y^2}{R}}{1 + \sqrt{1 - \frac{(c+1)y^2}{R^2}}} + a_4y^4 + a_6y^6 + a_8y^8 + a_{10}y^{10} \quad (3.1)$$

where R is the radius of curvature, c is the conic constant, x is measured on the optical axis, y is the distance from the optical axis, and a_4, a_6, a_8, a_{10} are the aspheric coefficients. Initially, we determined a_4 by reducing the image’s field curvature as much as possible, and we proceeded in sequentially determining a_6, a_8, a_{10} to reduce it further. A similar iterative optimization method for condensing lenses is described in [Roffman, 1991].

As previously stated, the condensing lens projects the retinal surface on an aerial image. One expects that different surfaces in the eye will create focused aerial images at different locations on the optical axis. We call the set of intraocular points that come in focus simultaneously an *isofocus* surface. Locations inside the eye correspond to pixels (coordinates on the aerial image) in a way that differs from the perspective projection model; we call the locus of intraocular points that is imaged on the same pixel coordinates an *isopixel* curve. The locations of the isofocus surfaces and isopixel curves are dependent on the condensing lens and the individual eye.

We estimate the isofocus surfaces and the isopixel curves by raytracing.

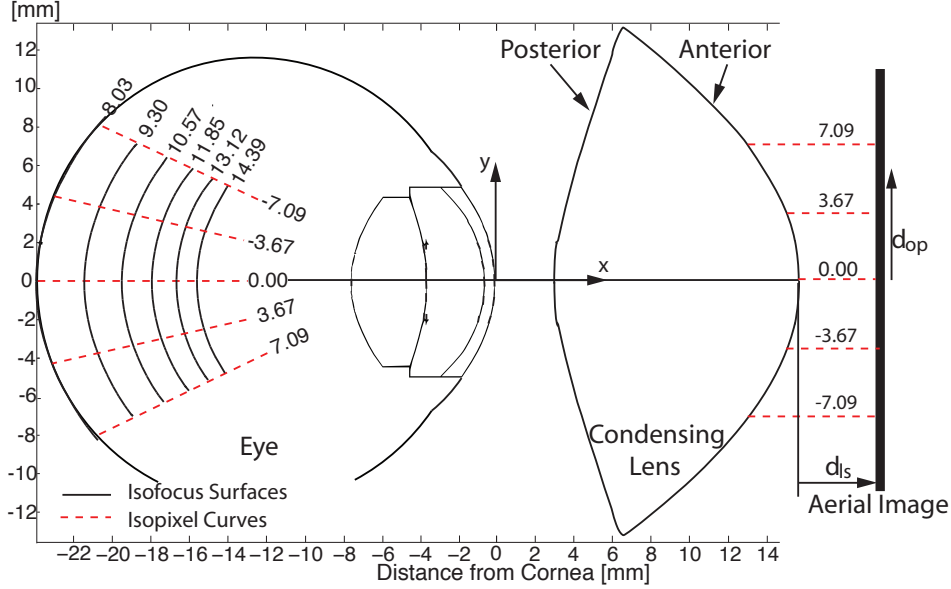


Figure 3.5: Simulation of the isofocus surfaces and isopixel curves for the system of Fig. 3.4(a). The different isofocus surfaces correspond to the distance from the lens to the aerial image (d_{ls}), for uniform image steps of ~ 1.27 mm. The isopixel curves correspond to pixel distances from the optical axis (d_{op}).

Due to the rotational symmetry of the system, we examine the 2D case. For a grid of points inside Navarro's eye, a fan of rays is traced until the spot size created by the rays is minimized (i.e. the image is in focus). The 2D coordinates on the image plane where the rayfan is focused specify the pixel coordinates on the image. With the calculated information we create the isofocus surfaces and isopixel curves. In theory there is an infinite number of isofocus surfaces and isopixel curves. Their number depends on the theoretical resolution of the system that captures the aerial image (its depth-of-field), and on its pixel size, respectively. Results for the area of validity of the Navarro eye can be seen in Fig. 3.5.

Figure 3.5 shows that the isofocus surfaces are denser closer to the retina. Moreover, it shows that the formed image is inverted. From the slope of the isopixel curves, it can be seen that the magnification of intraocular objects increases farther from the retina.

3.2.1 Surface and Curve Parametrization

The isofocus surfaces result from the optics of a rotationally symmetric and aligned system composed of conic surfaces. Therefore, it is assumed that they are also conic surfaces that can be parametrized by their conic constant, radius of curvature, and intersection with the optical axis. Since the isofocus surfaces correspond to a specific aerial image position, their three parameters can also be expressed as functions of this position. The radius of curvature and intersection with the optical axis for the fitted surfaces are displayed in Fig. 3.6(a) as polynomial functions of the aerial image position. For each parameter, we fit the least-order polynomial that captures its variability effectively. Navarro's eye has a retinal surface of zero conic constant (i.e. its retina is spherical). Therefore, the conic constant of the isofocus surfaces is set to zero. Our simulations show that the variation of the isofocus surfaces can be captured successfully by changes in the curvature.

The isopixel curves are lines, and it is straightforward to parametrize them using their slope and their intersection with the y -axis, given a coordinate frame. Each isopixel curve corresponds to one pixel on the image, and its parameters are functions of the pixel's offset (measured from the image center) due to the rotational symmetry of the system. For the 2D case, two parameters are required. The parameters of the fitted lines are shown in Fig. 3.6(b) as polynomial functions of the pixel's coordinate on the image sensor. For each parameter, we fit a third-order polynomial, which was experimentally found to be the least-order polynomial that captured its variability effectively.

With the parametrization of the isofocus surfaces and isopixel curves known, it becomes clear that knowledge of the position of the aerial image of an object and of the object's position in that aerial image provides enough information for localization.

3.3 Conclusions

We studied the image formation on-axis for different cases of ophthalmoscopy, and concluded that ophthalmoscopy using condensing lenses is the

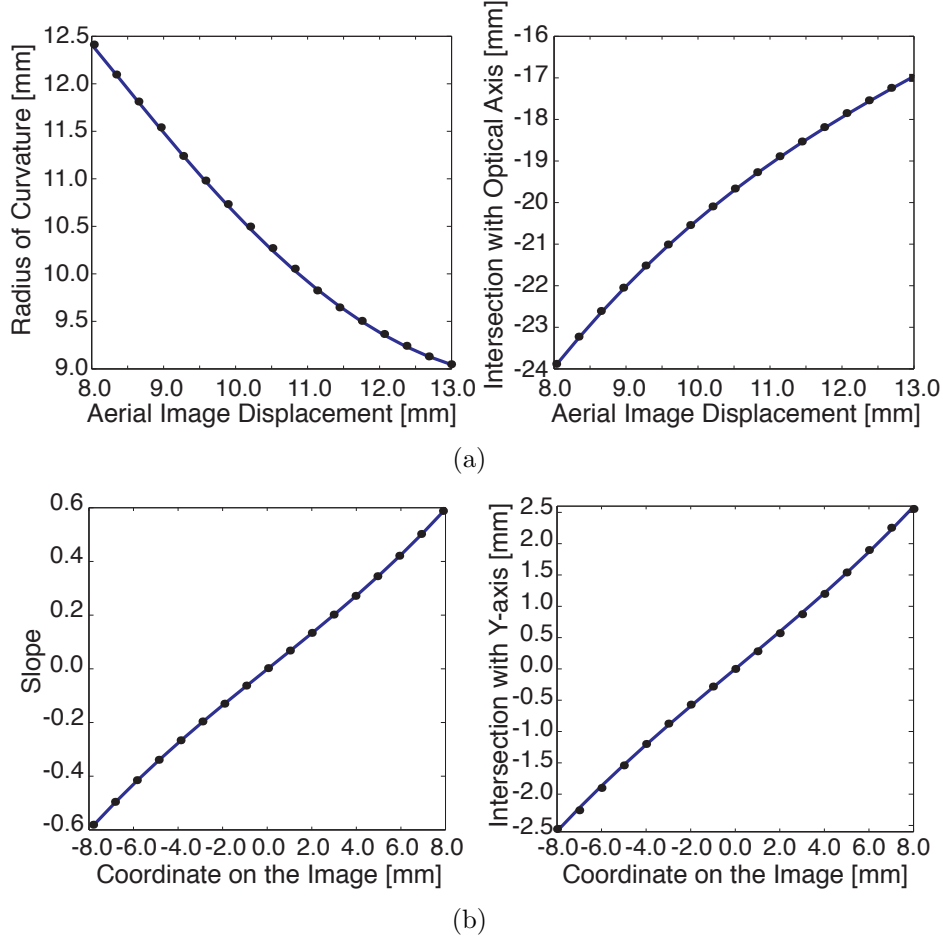


Figure 3.6: Parametrization polynomials for the optical system of Fig. 3.5. (a) Isofocus surface parametrization: Fitted third-order polynomials for the radius of curvature and for the intersection with the optical axis, respectively. (b) Isopixel curve parametrization: Fitted third-order polynomials for the line slope and for the intersection with the y-axis, respectively.

most promising method for intraocular imaging. We further examined the wide-angle image formation for indirect ophthalmoscopy, and extracted functions that describe this procedure. Using these functions and the introduced isofocus surfaces and isopixel curves, we will present a focus-based, and a model-based localization algorithm for intraocular microdevices, in Chapters 4 and 5, respectively.

Chapter 4

Single-Camera Focus-Based Localization of Intraocular Microdevices

In the previous chapter, we extracted the relationship between intraocular points and their created images for different cases of ophthalmoscopy. Our results indicate methods for depth extraction that involve using focus/defocus information [Ens and Lawrence, 1993; Subbarao and Surya, 1994]. These methods do not require a model of the object, but only knowledge of the optical system. Depth-from-focus methods extract depth information by bringing an image into focus, whereas depth-from-defocus methods rely on the amount of defocusing in an image to estimate depth. In [Luo *et al.*, 2006; Wu *et al.*, 2005], methods to track fluorescent particles in fluids using defocus information are presented. Were depth-from-focus/defocus methods applied in the human eye, they could be used to localize not only modeled devices, but also unknown objects such as floaters or foreign bodies. Depth from defocus is proposed in [Yeşin *et al.*, 2004] as a method to visually servo intraocular microrobots, however, in their work, the optics of the eye are not considered.

4.1 Algorithm

In direct ophthalmoscopy, the image rapidly approaches infinity as a device moves closer to the retina. The imaging system that would capture the created images would need an infinite working distance, and as a result, it would also possess a large depth-of-focus. Thus, extracting depth information from focus would be impossible.

The virtual images of intraocular objects when vitrectomy lenses are used span a smaller distance and lie inside the eye. For objects near the retina,

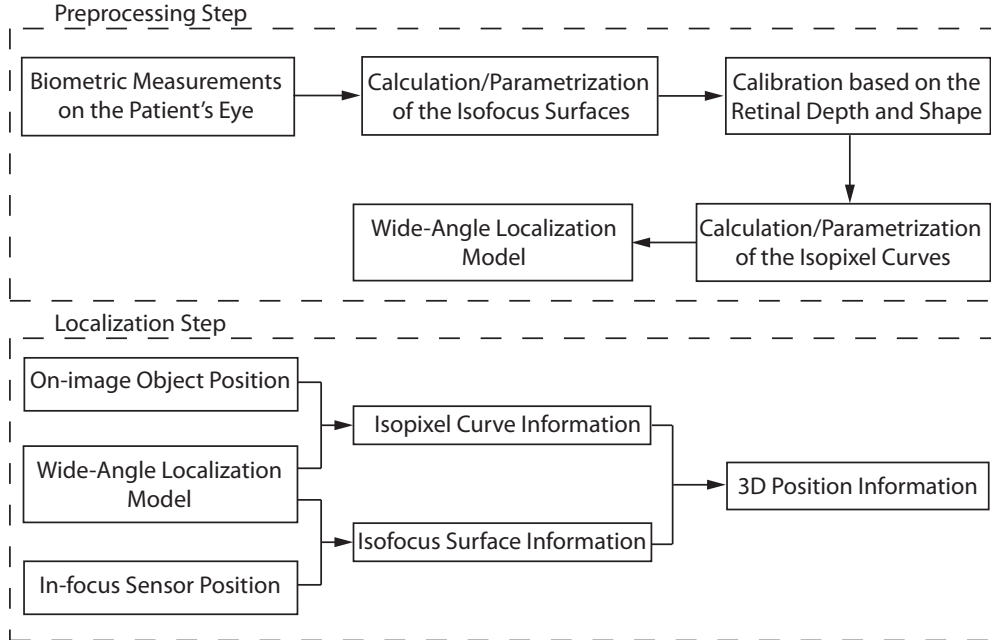


Figure 4.1: Flowchart for the proposed wide-angle localization algorithm.

an imaging system with at least a 20 mm working distance is required. As depth-of-field is proportional to working distance, there is a fundamental limit to the depth-from-focus resolution achievable with vitrectomy lenses.

In indirect ophthalmoscopy, however, if the aerial image is captured by an imaging system with a shallow depth-of-field, both a high field-of-view and accurate focus-based localization can be achieved.

Our localization algorithm involves estimating the position of an intraocular point as the intersection of its isopixel curve (determined from its pixel coordinates on the in-focus image) with its isofocus surface (determined from the displacement of formed aerial image with respect to the condensing lens).

In the following, we will assume that the aerial image is captured directly by an image sensor. This is possible due to the image's low field-of-curvature, which is achieved through the condensing lens optimization that was described in the previous chapter. However, the proposed algorithm can be applied to any type of imaging system that has a shallow depth-of-field. The flowchart of the algorithm can be seen in Fig. 4.1.

In our analysis, we use the condensing lens that was designed in the previous chapter (Table. 3.4). Since our method relies on focus information, we calculate the depth-of-focus for the indirect ophthalmoscopy imaging system of Fig. 3.5. Using paraxial equations [Focal Encyclopedia of Photography, 1965] (p. 404), we have:

$$\delta = \frac{n_v}{A_N}(1 + m)c \quad (4.1)$$

where δ is the depth-of-focus, $m = 0.76$ is the system's magnification (given from OSLO), $n_v = 1.336$ is the refractive index of the vitreous humor, $A_N = 0.159$ is the numerical aperture (given from OSLO), and c is diameter of the circle of confusion. For the case where the image is captured directly by an image sensor with a $6.4 \mu\text{m} \times 6.4 \mu\text{m}$ sensing element, $c = 6.4 \mu\text{m}$. The depth-of-focus is then estimated at $\delta = 95 \mu\text{m}$. Finally, using the slope in Fig. 3.4(b), we can estimate the depth-of-field at approximately $150 \mu\text{m}$; this is the theoretical resolution of this focus-based localization algorithm.

The isofocus surfaces diverge for regions farther from the retina. This divergence leads to an increased depth resolution in these regions. Based on the depth-of-field, the minimum resolution of the isofocus surfaces is also estimated at $150 \mu\text{m}$. Finally, given the calculated slope of the isopixel curves, we conclude that spatial resolution generally increases for positions closer to the intraocular lens.

In order to perform intraocular localization unambiguously, the parameters of the isofocus surfaces and isopixel curves should be injective (“one-to-one”) functions of the sensor position and the pixel coordinates, respectively, which, as seen in Fig. 3.6, holds. Intraocular localization can be unambiguous, and 3D wide-angle localization with this technique is possible.

4.2 Sensitivity Analysis

The proposed algorithm is expected to work when all the optical parameters are known with accuracy. However, even though biometric models for individual patients can be extracted, it is unknown if they are accurate. Esti-

mating the accuracy in the measurement of different eye parameters involves synthesizing information from measurements acquired *ex vivo* and *in vivo*. This results in large errors, and as a result, the data reported on this topic are limited. Moreover, the repeatability and reproducibility of the optical measurements is an ongoing debate among clinicians, and different groups occasionally report conflicting results [Zadnik *et al.*, 1992]. Thus, in order to evaluate the potential of the proposed localization algorithm, we must estimate its behavior with respect to inaccuracies in the modeling.

To achieve this, we first modify the eye model by individually perturbing each of the optical elements of the Navarro model. Next, we raytrace from intraocular points that cover 70° of the eye’s field-of-view to the image. Finally, we use the position where the image is formed (the in-focus sensor position) and the position of the projections on the image (pixel coordinates) to estimate the 3D position of the original intraocular points. In this case, however, we use the isopixel surfaces and isopixel curves estimated for the unperturbed Navarro model. As a result, there are errors in the estimated positions. These errors enable us to understand how uncertainties in the different optical parameters affect the localization results and, therefore, which optical elements most affect intraocular localization.

Since Navarro’s model is based on anatomical data, for the perturbations in the eye parameters we apply the standard deviations reported in the literature. For each optical element, we span its parameter space and calculate the maximum localization error. A similar analysis to estimate the effect of parameter changes in the optic power of the eye and the intraocular lens is conducted in [Atchison and Smith, 2000] and [Norrby, 2008], respectively. However, [Atchison and Smith, 2000] uses thin-lens equations, which are not appropriate for the wide-angle case, and [Norrby, 2008] uses the standard error instead of the standard deviation of the population, and consequently underestimates uncertainties.

The first optical element that rays emanating from intraocular objects pass through is the vitreous humor. The vitreous humor of the human eye is a viscoelastic fluid that is composed of 99% water. The refraction index of water is 1.333, and the refractive index of the vitreous humor in Navarro’s

model is 1.336. We assume a variation of $\pm 2\%$ in this parameter. The maximum localization errors that result by assuming such an uncertainty can be seen in Fig. 4.2(a).

The intraocular lens is a gradient refractive index lens, and its precise characterization is an open research topic [Campbell, 1984; Jones *et al.*, 2005]. This is why schematic eye models typically propose an equivalent intraocular lens with a constant refractive index of 1.42 [Escudero-Sanz and Navarro, 1999; Atchison and Smith, 2000], though there is ongoing work to consider its special refractive index distribution [Liou and Brennan, 1997; Goncharov and Dainty, 2007]. Based on this, it is difficult to establish uncertainty margins for this parameter, so we examine a large variation of constant refractive indices (1.363-1.476). In [Kirschkamp *et al.*, 2004] the anterior and posterior radii of curvature of the intraocular lens were measured using an autokeratometer and the extracted variations were $\pm 4\%$ and $\pm 8\%$, respectively (9 patients). In [Carney *et al.*, 1997] the lens thickness was measured for 30 adult emmetropic eyes and the resulting variation was $\pm 6\%$, whereas in [Kirschkamp *et al.*, 2004] the variation was calculated at $\pm 3\%$. The maximum localization errors that these uncertainties lead to are displayed in Fig. 4.2(b). This figure shows that the greatest errors are caused by uncertainties in the refractive index of the intraocular lens. Maximum uncertainty in this parameter leads to errors of approximately 4.5 mm.

Similarly to the vitreous humor, the aqueous humor consists primarily of water. We assume the same variation in its refractive index ($\pm 2\%$). The thickness of the anterior chamber was measured in [Carney *et al.*, 1997], and the variation between 113 patients was $\pm 10\%$. In [Kirschkamp *et al.*, 2004] this variation was estimated at $\pm 6\%$. The maximum localization errors can be seen in Fig. 4.2(c).

Methods to measure the cornea of the human eye are reported in [Read *et al.*, 2006; Dubbelman *et al.*, 2006]. Both efforts report variations of $\pm 3\%$ for the corneal anterior radius of curvature after measuring 100 and 114 patients, respectively. The variations of the corneal thickness and the posterior radius of curvature are calculated as $\pm 6\%$ and $\pm 4\%$, respectively. The refractive index of the cornea was measured for 10 eyes in [Patel *et al.*, 1995]. The

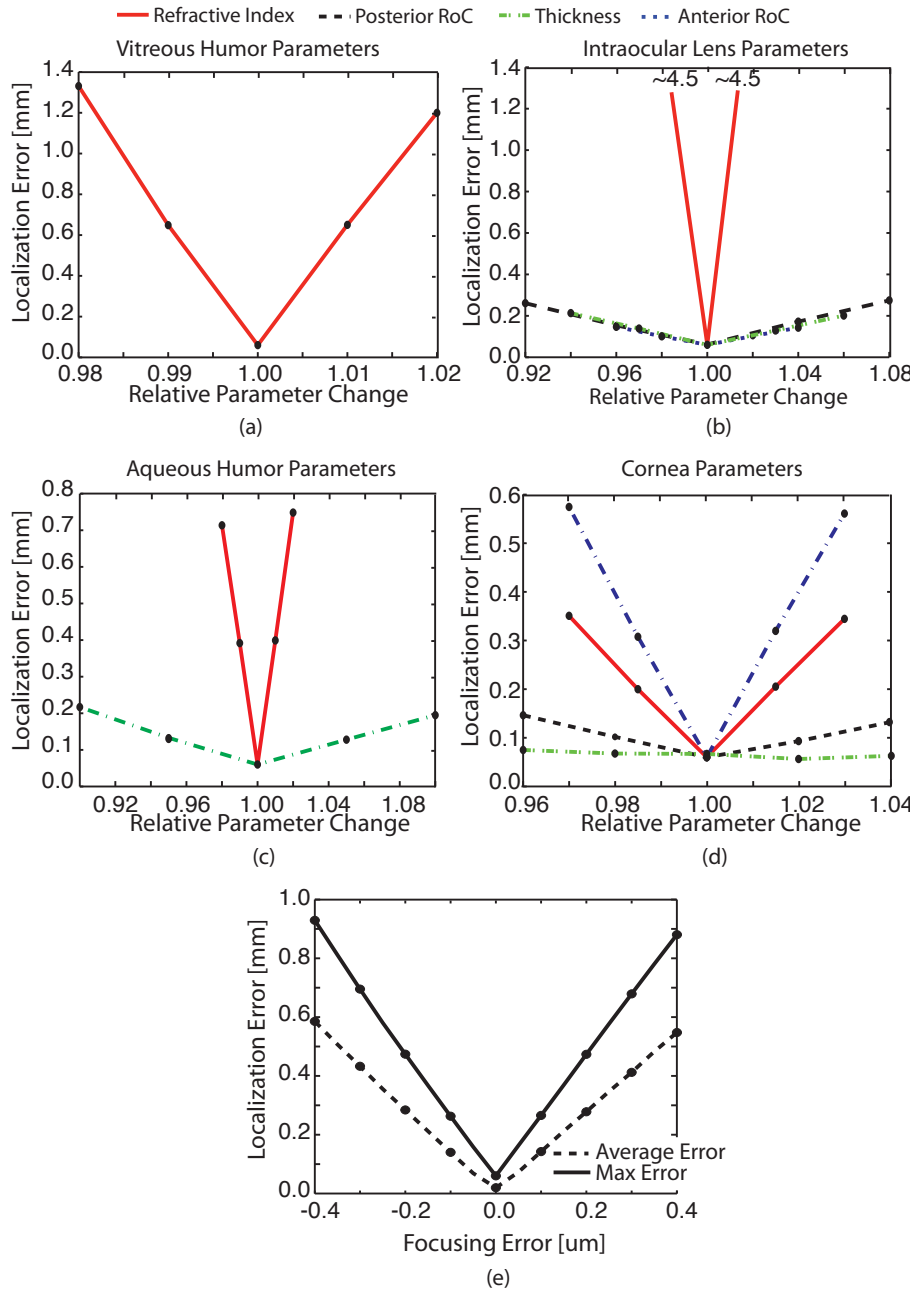


Figure 4.2: Maximum localization errors due to parameter uncertainty: (a) vitreous humor, (b) intraocular lens, (c) aqueous humor, (d) cornea, (e) focusing. (RoC: Radius of Curvature).

conclusion is that the anatomical elements of the cornea (epithelium, anterior surface, posterior surface) have different refractive indices, and their values range from 1.372 to 1.406. Given that the mean corneal refractive index from [Escudero-Sanz and Navarro, 1999] is 1.376, we conclude that the variation in the refractive index is 3%. In Fig. 4.2(d) we show the maximum errors resulting from each uncertainty. The most sensitive parameter is the anterior radius of curvature.

The condensing lens can be machined with μm accuracy (errors less than 0.1% based on personal communication with Sumipro bv. [Sumipro BV, 2010], a lens-manufacturing company), and its refractive index is that of well-known materials. We do not consider variation in its parameters.

In Fig. 4.2(e) we show the mean and maximum localization errors attributed to the miscalculation of focus. Better focus estimation can be achieved by selecting the appropriate focus-measurement algorithm from [Sun *et al.*, 2004].

Based on Fig. 4.2, there are a number of parameters that, if imprecisely known, can lead to high localization errors. The five most important eye parameters are: (1) Refractive index of the intraocular lens, (2) Refractive index of the vitreous humor, (3) Anterior radius of curvature of the cornea, (4) Refractive index of the aqueous humor, (5) Refractive index of the cornea. This sensitivity analysis and our discussion point to the fact that for the localization algorithm to be successful, calibration procedures that account for parameter uncertainties are needed.

4.3 Calibration

Preliminary experiments show that calibration of the isopixel curves is not necessary, because their relative impact on the localization accuracy is low. It is the intersection of the isofocus surfaces with the optical axis (Fig. 3.6(a) right) that has the greatest effect on localization.

Ideally, one would perform an on-optical-axis depth-from-focus experiment, and calibrate for the relationship between the in-focus sensor position and the depth of the object using the full set of data points. However, such

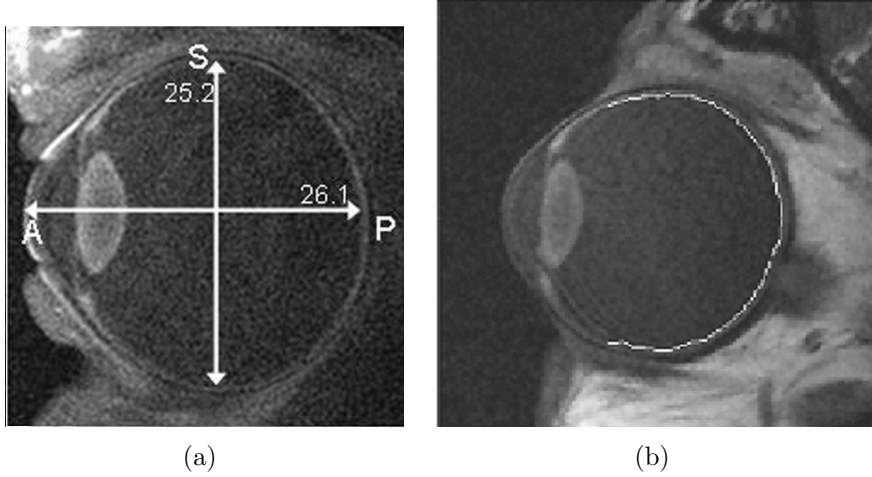


Figure 4.3: Biometric measurements from MRI images: (a) axial length, (b) retinal shape. Images taken from [Atchison *et al.*, 2004] and [Atchison *et al.*, 2005], respectively.

an approach would be invasive and would require a vitrectomy. The depth and shape of the retina, though, can be noninvasively extracted from MRI data [Atchison *et al.*, 2004; 2005] (Fig. 4.3).

The proposed calibration method uses a first-order model of the optics of the system. First-order optics accurately describe the image formation of on-axis objects. We assume that the optical modeling has accumulated errors that can be lumped and included as errors in the estimated image and object positions. Afterwards, we can calibrate the imaging system using only the retinal depth of a patient’s eye. The analysis that follows demonstrates that this method suppresses the errors caused by large uncertainties in the eye’s optical parameters.

We extract the first-order optical model of Navarro’s eye with the condensing lens (Fig. 4.4) by calculating the principle points/planes using OSLO. We verified that OSLO performs the paraxial calculations as described in [Hecht, 2002; Lambda Research Corporation, 2001]. In this framework, each lens is described by three matrices (two refraction matrices \mathcal{R}_1 and \mathcal{R}_2 , and one

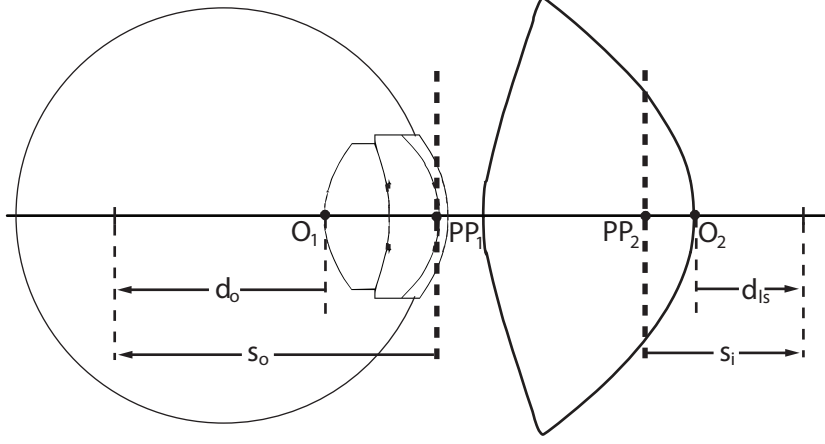


Figure 4.4: Illustration of the first-order optical model for the system of Navarro's eye with a condensing lens. (PP: Principal point).

transfer matrix \mathcal{T}_{21}):

$$\mathcal{R}_1 = \begin{bmatrix} 1 & -\mathcal{D}_1 \\ 0 & 1 \end{bmatrix}, \text{ where } \mathcal{D}_1 = \frac{n_l - n_o}{r_1} \quad (4.2)$$

$$\mathcal{R}_2 = \begin{bmatrix} 1 & -\mathcal{D}_2 \\ 0 & 1 \end{bmatrix}, \text{ where } \mathcal{D}_2 = \frac{n_i - n_l}{r_2} \quad (4.3)$$

$$\mathcal{T}_{21} = \begin{bmatrix} 1 & 0 \\ t/n_l & 1 \end{bmatrix} \quad (4.4)$$

where the subscripts 1 and 2 refer to the posterior and anterior surfaces of the lens, respectively; n_l is the refractive index of the lens; n_o is the refractive index of the environment on the object side; n_i is the refractive index of the environment on the image side; r_1 and r_2 are the radii of curvature; and t is the thickness of the lens. Then, the focal length and the principal points of

the lens can be found by:

$$\mathcal{A} = \begin{bmatrix} a_{11} & a_{12} \\ a_{21} & a_{22} \end{bmatrix} = \mathcal{R}_2 \mathcal{T}_{21} \mathcal{R}_1 \quad (4.5)$$

$$f = -\frac{1}{a_{12}} \quad (4.6)$$

$$[O_1, PP_1] = \frac{n_o(1 - a_{11})}{-a_{12}} \quad (4.7)$$

$$[O_2, PP_2] = \frac{n_i(a_{22} - 1)}{-a_{12}} \quad (4.8)$$

where f is the effective focal length, and the operator $[: , :]$ is the signed distance between two points.

For Navarro's eye equipped with a condensing lens the matrices corresponding to all the lenses are multiplied:

$$\mathcal{A} = \mathcal{R}_{cl_2} \mathcal{T}_{cl_{21}} \mathcal{R}_{cl_1} \mathcal{T}_{air} \mathcal{R}_{co_2} \mathcal{T}_{co_{21}} \mathcal{R}_{co_1} \mathcal{T}_{aq} \mathcal{R}_{il_2} \mathcal{T}_{il_{21}} \mathcal{R}_{il_1} \quad (4.9)$$

where $\{\mathcal{R}, \mathcal{T}\}_{cl}$ are the matrices that correspond to the condensing lens, $\{\mathcal{R}, \mathcal{T}\}_{co}$ are the matrices that correspond to the cornea, $\{\mathcal{R}, \mathcal{T}\}_{il}$ are the matrices that correspond to the intraocular lens, \mathcal{T}_{air} is the matrix corresponding to the air between the condensing lens and the cornea, and \mathcal{T}_{aq} is the matrix corresponding to the aqueous humor between the cornea and the intraocular lens. Then, the effective focal length and the principal points/planes for Navarro's eye equipped with the condensing lens can be calculated from (4.5)-(4.8).

The compound optical system projects an object at s_o to an image at s_i :

$$s_i = d_{ls} + [O_2, PP_2] + e_{d_{ls}} \quad (4.10)$$

$$s_o = -\frac{f n_v s_i}{s_i - f} \quad (4.11)$$

$$d_o = s_o - [O_1, PP_1] + e_{d_o} \quad (4.12)$$

where n_v is the refractive index of the vitreous humor; d_{ls} is the distance from the condensing lens where the image is formed; and e_{d_o} , $e_{d_{ls}}$ are the

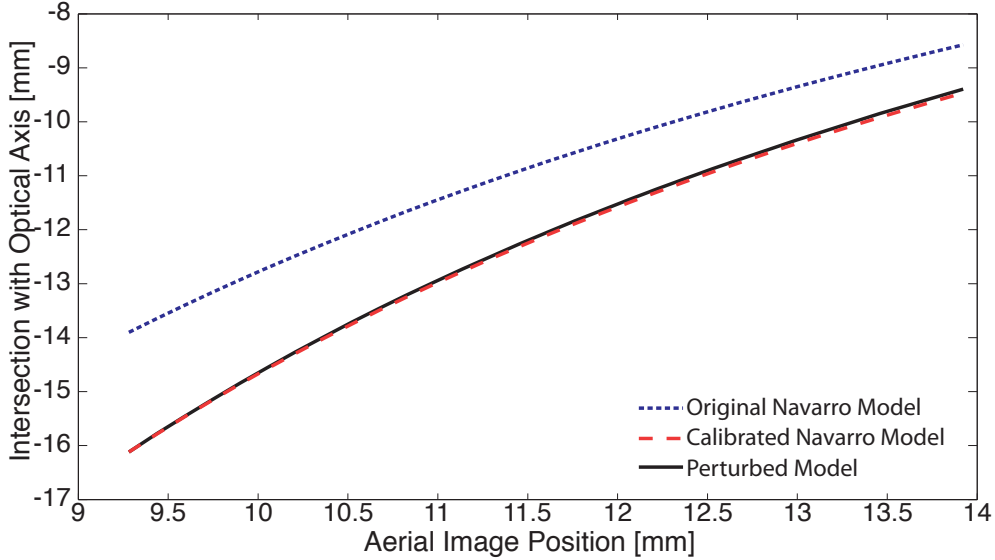


Figure 4.5: Effects of biometric calibration on a system with 3% uncertainty in the refractive index of the intraocular lens. We assume the retinal depth is precisely known.

lumped errors in the estimated object and image positions respectively.

In (4.10)–(4.12) the parameters are calculated using paraxial approximation formulas. However, due to the inclusion of the conic and aspheric components in the condensing lens (Table 3.4), these parameters need to be refined. We use the paraxial calculations as an initial estimation, and perform a minimization so that (4.10)–(4.12) accurately describe the behavior of the intersection of the isofocus surfaces with the optical axis.

Using (4.10)–(4.12) and only the measured retinal depth and its corresponding in-focus sensor position, we estimate $e_{d_{ts}}$ and e_{d_o} that minimize the error in the estimated retinal intraocular depth. Assuming perfect knowledge of the retinal depth, the calibration results for 3% uncertainty in the refractive index of the intraocular lens can be seen in Fig. 4.5.

In [Atchison *et al.*, 2004], after measuring the ocular axial length of 22 adult emmetropes and 66 adult myopes with MRI scans, errors up to 0.3 mm between measurements of the same patient of any category were reported. Comparison of the MRI-based results with A-scan ultrasonography reported

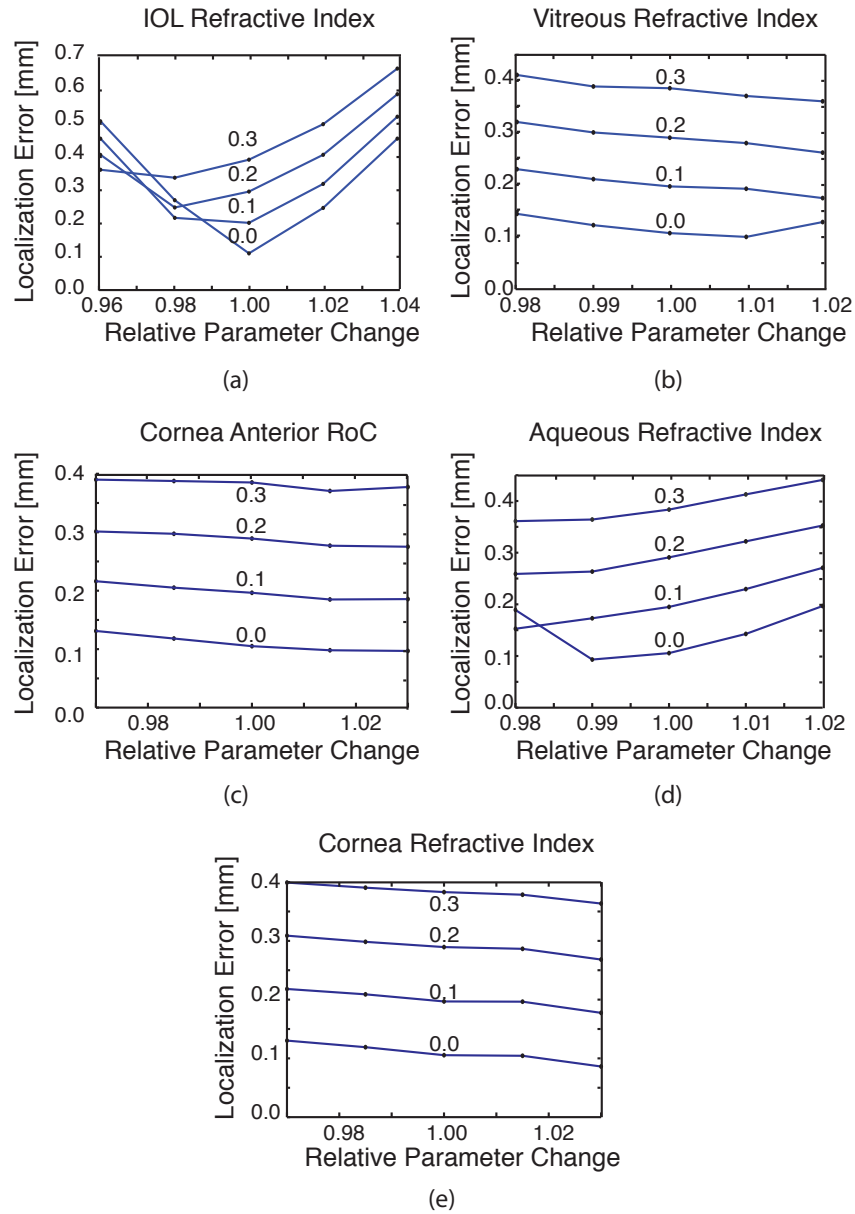


Figure 4.6: Localization error due to parameter uncertainty after calibration for the five most crucial parameters of Fig. 4.2: (a) intraocular lens refractive index, (b) vitreous humor refractive index, (c) cornea anterior radius of curvature, (d) aqueous humor refractive index, and (d) cornea refractive index. The errors (in mm) in the retinal depth estimation are shown above each curve.

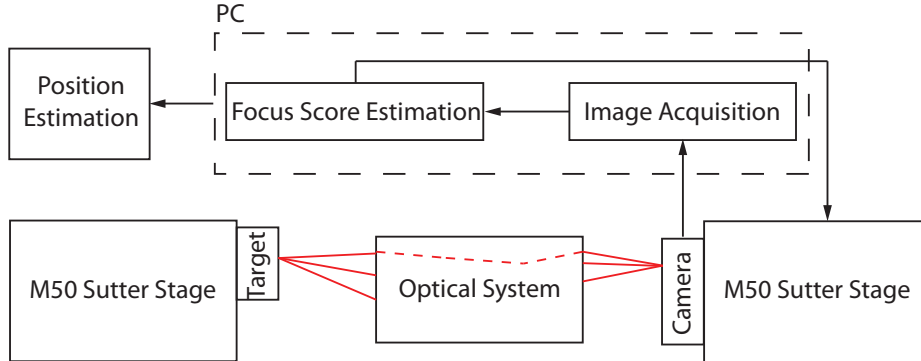


Figure 4.7: Our experimental setup consists of two M50 Sutter micromanipulation stages; one is responsible for moving the target and one for moving the camera to focus. Focus is calculated using the normalized variance, and the position of the camera that gives rise to the sharpest image is used to estimate the target’s position.

good agreement across patients (0.3 ± 0.2 mm). We take these inaccuracies into account and calculate the resulting maximum localization error, after biometric calibration, for variations in the optical eye parameters to which localization is most sensitive. The results can be seen in Fig. 4.6. Comparison with Fig. 4.2 shows that this calibration procedure indeed suppresses localization errors, and accurate retinal depth measurements greatly reduce them. Original error values were on the order of 1 mm and up to 4 mm for the refractive index of the intraocular lens, the most sensitive parameter.

4.4 Experiments in a Model Eye

To demonstrate the proposed wide-angle localization method, we use an appropriate imaging system and perform wide-angle focus-based localization in a model eye.

4.4.1 Experimental Setup

As an experimental testbed, we use the model eye [Gwb International, Ltd., 2010] from Gwb International, Ltd. This eye is equipped with a plano-convex lens that mimics the compound optical system of the human eye. The

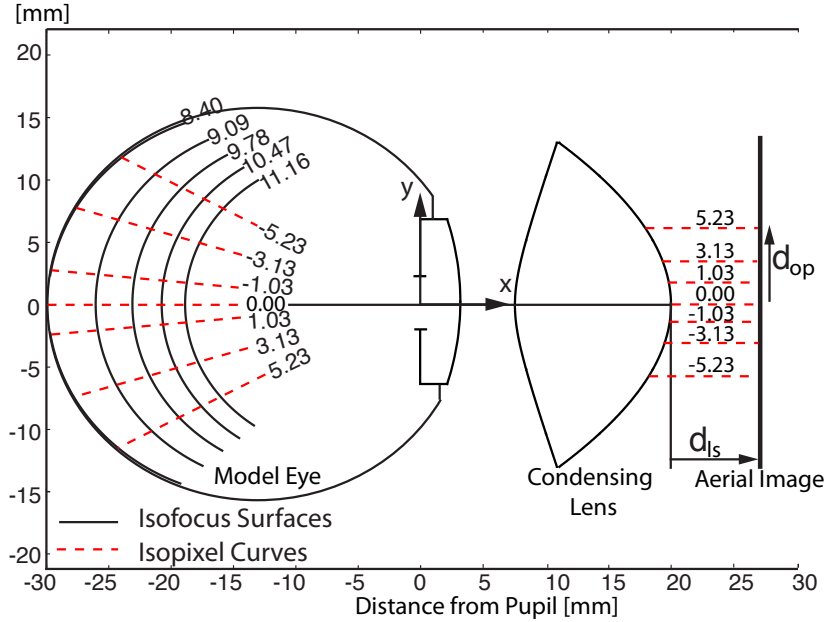


Figure 4.8: Simulation of the isofocus surfaces and isopixel curves for the system composed of the model eye and the condensing lens. The different isofocus surfaces correspond to the distance from the lens to the sensor (d_{ls}), for uniform sensor steps of ~ 0.7 mm. The isopixel curves correspond to pixel distances from the optical axis (d_{op}).

model eye contains no “vitreous”, and thus, the lens can be used by itself. Gwb International, Ltd. disclosed the lens’ parameters so that simulations can be accurately performed. The dimensions of the model eye were measured to estimate its retinal depth and shape. A schematic of our setup is shown in Fig. 4.7.

The imaging device consists of two components. A condensing lens is kept at a constant position with respect to the eye, and a sensor captures the aerial image directly and moves with respect to the lens to focus on objects throughout the eye. The condensing lens is a custom made double conic-convex lens (see Table. 3.3 for parameters, where the refractive index was changed to 1.531). This lens causes a $0.78\times$ magnification, thus, an object of $100\ \mu\text{m}$ near the retina creates an image of $78\ \mu\text{m}$. The image is captured by a firewire Basler A602f camera with a CMOS sensor ($9.9\ \mu\text{m} \times 9.9\ \mu\text{m}$

sensing element, 640×480 non-interpolated resolution). The camera and the object were moved using two M-285 Sutter linear micromanipulation stages. Focus was calculated using the normalized variance of the captured image. According to [Sun *et al.*, 2004], the normalized variance is the most robust image focusing metric for noisy images.

4.4.2 Isofocus Surfaces and Isopixel Curves

The simulated isofocus surfaces and isopixel curves of the composite system are shown in Fig. 4.8. Their parametrization is shown in Fig. 4.9. The behavior of the parameters is similar to the one displayed in Fig. 3.6. The assumed conic constant of the isofocus surfaces is kept constant at -0.175 , which is the value we measured for the retina of the model eye.

4.4.3 Depth-of-focus and Resolution

Using (4.1) we calculate the depth-of-focus for this optical system at $83 \mu\text{m}$. The circle-of-confusion is given from the Basler A602f sensing element, and the remaining parameters can be calculated through OSLO. This is an estimation of the variance in the in-focus sensor position. From the slope of Fig. 4.9(a) (right) we can calculate depth-of-focus at $500 \mu\text{m}$.

4.4.4 Calibration

In order to calibrate the isofocus surfaces for their intersection with the optical axis, we perform a depth-from-focus experiment along the optical axis. The estimated in-focus sensor positions with respect to different depths in the model eye can be seen in Fig. 4.10. We calibrate using the method of Sec. 4.3. The parameters required for (4.10)–(4.12) were measured 30 times for accuracy (retinal depth $33.1 \pm 0.55 \text{ mm}$, inter-lens-distance $d_{ls} = 3.59 \pm 0.18 \text{ mm}$). Figure 4.10 shows the calibration results. The fully calibrated model corresponds to the fit that is generated when all the points from the optical-axis depth-from-focus experiment are used. In a clinical setting, such knowledge would be unavailable. The biometrically calibrated model corresponds to the fit that is generated when only the retinal depth is used. As can be seen,

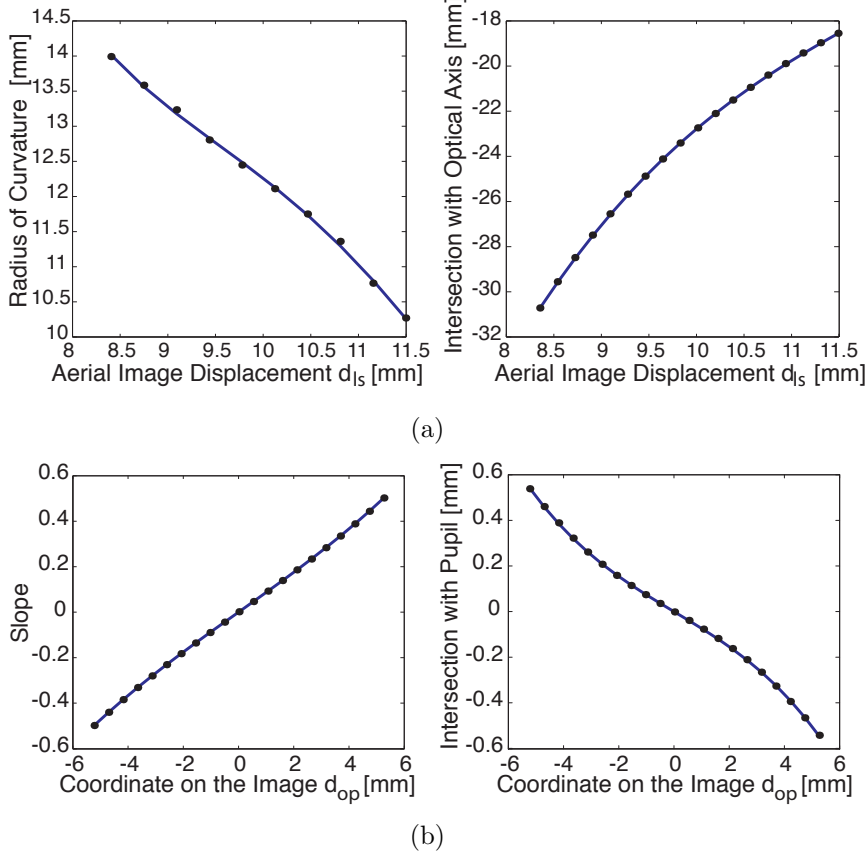


Figure 4.9: (a) Isofocus surface parametrization: Fitted third-order polynomials for the curvature and for the intersection with the optical axis. (b) Isopixel curve parametrization: Fitted third-order polynomials for the slope and for the intersection with the pupil.

biometric calibration adjusts the model to correspond to the experimental observations. The uncalibrated model from Fig. 4.9(a) (right) is shown for comparison.

The remaining two parameters of the isofocus surfaces control the shape of the isofocus surfaces but not their position. Our experiments show that we can capture an overall sharp image of the entire model eye's retina using the condensing lens. Therefore, we conclude that there exists an isofocus surface that corresponds to the retinal surface, and we consider this as the first surface. From Fig. 4.8, we see that the first isofocus surface does in-

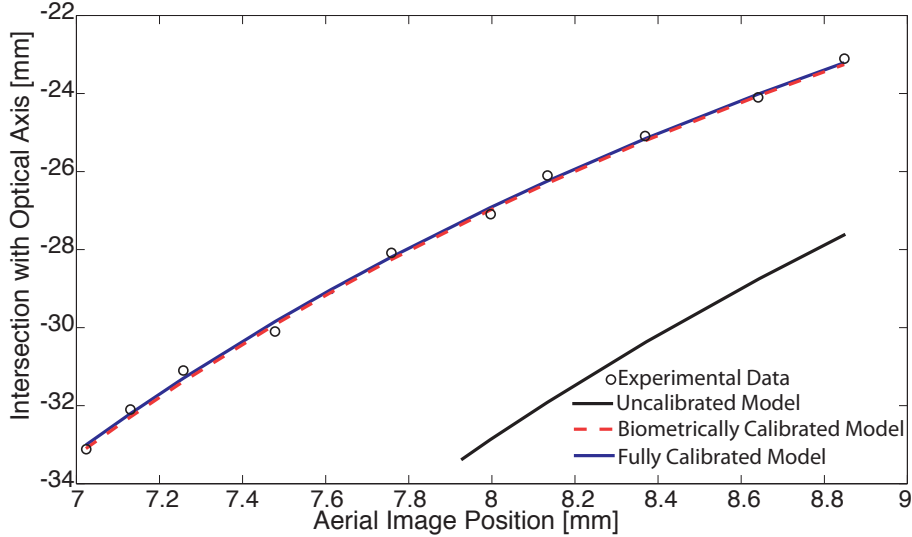


Figure 4.10: Different model fits for the function describing the intersection of isofocus surfaces with the optical axis (measured from the pupil) with respect to the in-focus sensor position.

deed roughly correspond to the retinal shape. As a result, calibration for the conic constant and the curvature is not needed. If the model did not accurately predict the shape of the retina, yet an in-focus image of the retina was obtained, then we would also calibrate the parameters of the first isofocus surface so that it has the same shape as the retina. It is not guaranteed that an isofocus surface corresponds to the entire retina for every eye (i.e. the possibility of an in-focus image of the entire retina is not guaranteed), however, this is also not a requirement for the localization algorithm.

4.4.5 Results

In order to test the wide-angle localization algorithm, we performed a localization experiment for various angles with respect to the optical axis and various distances from the pupil. We repeated the experiment 30 times for each point, and calculated the mean and variance in the in-focus sensor position. The calculated variances for the parameters of the algorithm allow calculation of the uncertainty of the estimations [Joint Committee for Guides

	surfaces				
	1	2	3	4	5
0°	5(102)	201(79)	195(102)	201(119)	271(119)
5°	410(60)	310(52)	285(48)	204(50)	329(85)
10°	125(79)	362(48)	250(60)	331(100)	300(47)
15°	105(156)	100(98)	195(79)	364(55)	394(145)
20°	481(100)	556(73)	381(111)	569(90)	520(364)
25°	126(128)	572(156)	207(55)	393(161)	430(139)
30°	556(153)	162(188)	424(301)	644(186)	405(195)

Table 4.1: Errors(uncertainty) [μm] for the localization experiment.

in Metrology, 2008].

Figure 4.11 displays the results of the proposed wide-angle localization algorithm. For comparison, we show the results when paraxial equations are used for the points on the retina. The predictions of the new localization algorithm remain close to the actual values, but, as expected, the results of paraxial localization deteriorate as the angles increase. The paraxial approximations are co-linear since first-order models assume a plane-to-plane image formation, whereas the condensing lens creates a flat image of the retina.

In Table 4.1 the experimentally measured localization errors with respect to increasing angles and distances from the pupil are shown. The rows show the errors for varying distances from the pupil, and the columns show the errors for varying angles. The errors are calculated using the mean in-focus sensor position. The number in parenthesis is the estimated uncertainty in μm based on the variance in the model parameters and the variance in the in-focus sensor position. The mean error is $325 \mu\text{m}$, and the standard deviation is $158 \mu\text{m}$. Given that the depth-of-field of the experimental optical system is $500 \mu\text{m}$, our errors are within the theoretical limits of the resolution.

4.5 Conclusions

Based on the analysis of the previous chapter concerning intraocular image formation in indirect ophthalmoscopy, we developed an intraocular localization algorithm and evaluated its sensitivity. We performed experiments in a model eye, where the localized object was a planar pattern. The accuracy

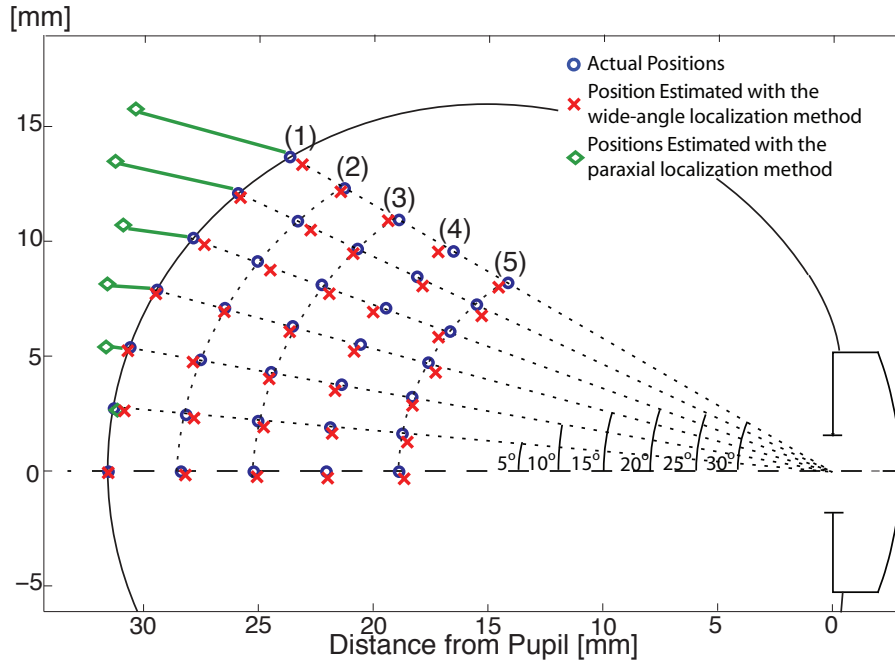


Figure 4.11: Localization experiment showing the performance of the wide-angle localization algorithm. The paraxial model, which loses accuracy away from the optical axis, is also shown for comparison.

and precision of the results agreed with models and data.

The primary issue with focus-based algorithms is the requirement of constant refocusing. Different parts of an object should be brought in focus in order to extract its full 3D shape, and the pixel window that is taken into consideration for the estimation of the focus score is also crucial; small windows will not accurately estimate the degree of focus, and large windows will cover parts of the object that have different depth, and cannot come into focus simultaneously.

These problems are taken into account in the following chapter, where we build on the extracted image model and the robustness of the isopixel curves. We develop a localization algorithm that estimates the pose of a device in a complicated cascade of optics given its 3D representation.

Chapter 5

Single-Camera Model-Based Localization of Intraocular Microdevices

In the previous chapters we discussed the process of image formation in ophthalmoscopy. We introduced the concept of the isofocus surfaces (i.e. the set of points in the interior of the eye that come in focus simultaneously) and the isopixel curves (i.e. the loci of intraocular points that are imaged on the same coordinates in the created image). The isofocus surfaces and isopixel curves were used in the previous chapter in the framework of depth-from-focus in order to perform localization in a model eye. Focus-based methods can be applied for unknown objects, since they do not require any information on the object. However, the necessity for constant refocusing complicates their application.

Common techniques for the localization of objects from monocular images use a 3D rigid-body model of the object of interest. If the imaging system is calibrated, then this model can be projected onto the 2D image plane. The 6 DOF pose of the model is adjusted via a minimization process until the projection fits with the perceived image, thus localizing the object. Examples of this approach in the macroscale and nanoscale are presented in [Drummond and Cipolla, 2002], and [Kratochvil *et al.*, 2009], respectively. In [Pezzeменти *et al.*, 2009], the researchers use known geometrical models of articulated robots to track them during different surgical procedures.

In the case of intraocular objects, there is currently no way to extract the projection model of the imaging system and use it in the algorithms discussed above. Calibrating the entire optical system using conventional techniques is infeasible because of the inaccessibility of the interior of the human eye, as well as because of its unique optics. Structure-from-motion and simultaneous calibration is also an open research problem, as discussed in chapter 3.

In this chapter, we revisit isopixel curves and use them to extract the analytical model of image formation. With a “map” for the projection of intraocular objects onto images, we can use existing rigid-body-tracking/pose-estimation techniques. In other words, we can reduce our open problem of estimating the position of devices under complicated refractive systems to the solved problem of rigid-body pose-estimation.

We briefly consider existing projection models. Then, based on indirect ophthalmoscopy, we account for the effect of the cascaded optics of the eye, the condensing lens, and the observing microscope, and extract the projection model for our optical system. We demonstrate the precision of our algorithm in a human-like model eye consisting of a cornea and intraocular lens.

5.1 Common Projection Models

Let the 3D points be denoted as $\vec{\mathbf{X}} = [x, y, z]^T$, and their homogeneous versions as $\tilde{\mathbf{X}} = [\vec{\mathbf{X}}^T, 1]^T$. Image coordinates in pixels are denoted as $\vec{\mathbf{u}} = [u, v]^T$, their homogeneous counterparts as $\tilde{\mathbf{u}}$, and metric image coordinates as $\vec{\mathbf{m}} = [m_i, m_j]^T$. The intrinsic parameter matrix of a camera is K , and $H \in SE(3)$ is the transformation matrix that relates the camera’s coordinate frame to the world coordinate frame. Finally, $H = e^{\hat{\xi}}$, where $\hat{\xi}$ is a twist, a 4×4 matrix in $se(3)$ that generates H [Murray *et al.*, 1994].

5.1.1 Perspective Projection Model

The most widely assumed projection model is perspective projection (pin-hole camera model), wherein a 3D point $\tilde{\mathbf{X}}$ projects to a 2D point $\tilde{\mathbf{u}}$ through the equation:

$$s \underbrace{\begin{bmatrix} u \\ v \\ 1 \end{bmatrix}}_{\tilde{\mathbf{u}}} = \underbrace{\begin{bmatrix} -\frac{s_u}{k_u} & \sigma & u_0 & 0 \\ 0 & -\frac{s_v}{k_v} & v_0 & 0 \\ 0 & 0 & 1 & 0 \end{bmatrix}}_K \underbrace{\begin{bmatrix} R & t \\ \mathbf{0} & 1 \end{bmatrix}}_{H=e^{\hat{\xi}}} \underbrace{\begin{bmatrix} x \\ y \\ z \\ 1 \end{bmatrix}}_{\tilde{\mathbf{X}}} \quad (5.1)$$

where $[u_0, v_0]^T$ is the image center in pixels; s_u, s_v is the scaling in the directions u, v , respectively; k_u, k_v is the sensor element size in the directions u, v respectively; σ denotes the orthogonality of sensor elements (with $\sigma = 0$ meaning orthogonal pixels); and s is an arbitrary scale factor.

As noted in [Grossberg and Nayar, 2005], the perspective projection model closely corresponds to the original concept of a device that creates an image but has three basic assumptions:

1. Each point in the image corresponds to a ray entering the imaging system.
2. All rays entering the imaging system intersect at a single point called the viewpoint.
3. The correspondence between rays passing through the viewpoint and the image is given by the intersection of the rays with a plane.

Modern imaging systems for which these assumptions do not hold are being developed. In catadioptric imaging systems, for example, the formed image cannot be described by the intersection of rays from their single viewpoint with a plane. These systems are preferred for their increased field-of-view. In systems composed of quadratic surface mirrors there is no single viewpoint [Grossberg and Nayar, 2005; Baker and Nayar, 1999; Swaminathan *et al.*, 2006]. These systems cannot be described using the perspective projection model, and to describe them a new framework is required.

5.1.2 The Raxel-Based Projection Model

A generalized framework for the description of such systems, the “raxel” imaging model, was introduced in [Grossberg and Nayar, 2005]. Its core idea is that, since all imaging systems perform a mapping from rays to photosensitive elements on the image sensor, the theory should be general enough to describe this mapping irrespectively of the optical elements of the imaging system. The introduced concept is the “raxel”, a photosensitive element that measures light in a single direction. Each raxel holds information on the intensity and direction of the incoming light, as well as on the image pixel

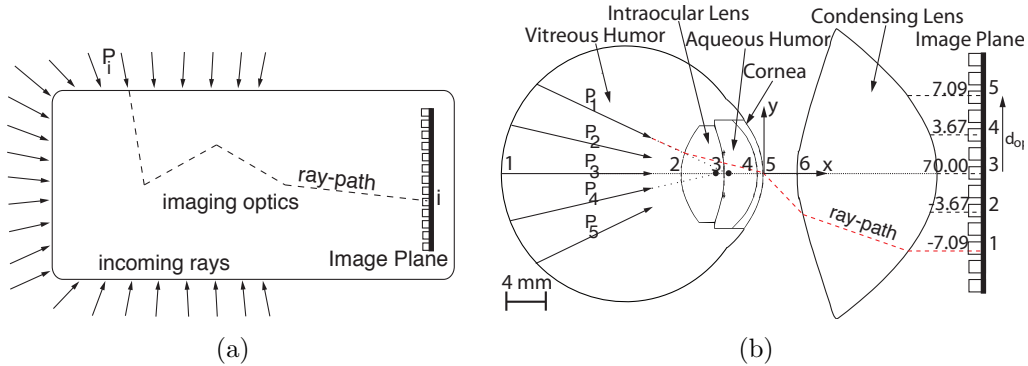


Figure 5.1: (a) The concept of the raxel imaging model (adapted from [Grossberg and Nayar, 2005]). The process of image formation is abstract and simply assumes there exists a map between an incoming ray P_i and the sensing element i . (b) The schematic eye [Escudero-Sanz and Navarro, 1999] equipped with a condensing lens [Volk, 1998]. Each “ray” (e.g. P_1 – P_5) inside the eye is called an “isopixel curve” and corresponds to a single location on the image plane. The isopixel curves correspond to pixel distances from the optical axis (d_{op}) for fixed steps of ~ 3.5 mm. Since the isopixel curves do not intersect at a single point, there are multiple viewpoints.

that it corresponds to. The imaging system is treated as a black box, and as long as the information from the raxels is known, the image formation can be described. This concept is illustrated in Fig. 5.1(a).

5.2 Projecting Through the Eye’s Optics

Figure 5.1(b) shows how our imaging system consisting of the human eye and additional ophthalmic lenses can be treated in a similar fashion. The goal is to find the map between the “incoming rays” and the final pixel coordinates. The isopixel curves extracted with the method presented in chapter 3 are also displayed. The flowchart of our pose-estimation algorithm is shown in Fig. 5.2.

The isopixel curves do not intersect on a single point on the optical axis, making the imaging system a multiple-viewpoint system. Their parametrization polynomials are shown in Fig. 5.3. The current form of the parametrizing functions does not allow for easy analytic estimation of projections. Given an

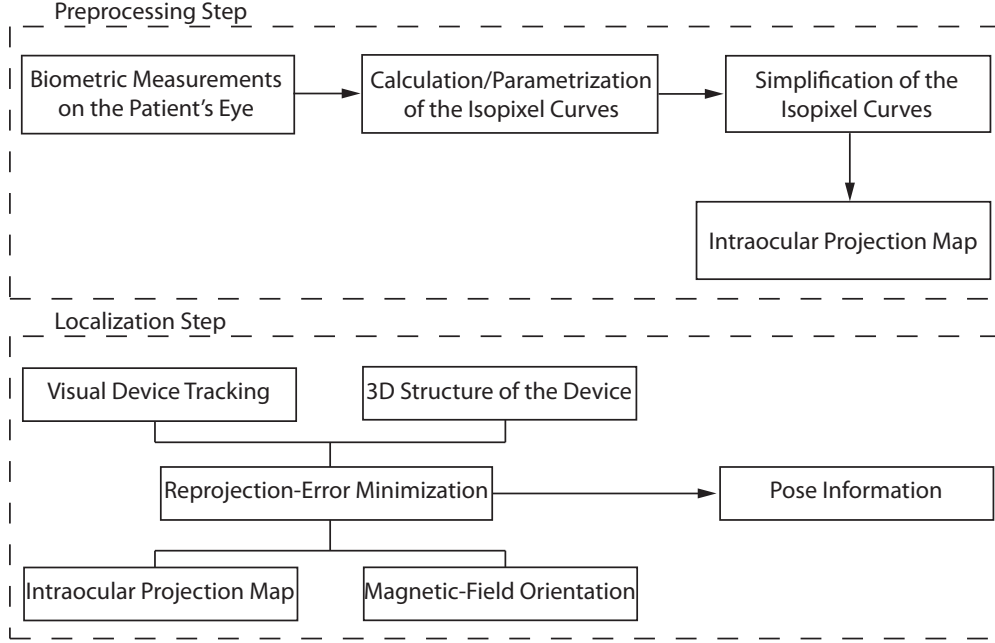


Figure 5.2: Flowchart for the proposed pose-estimation algorithm.

intraocular point we cannot estimate the isopixel curve on which it belongs due to the lack of a known viewpoint on the optical axis.

The solution to this problem comes from the simplification of the isopixel curves and the introduction of a single-viewpoint. A similar technique was developed in [Derrien and Konolige, 2000] for a panoramic imaging system, where the authors adjust the angles of rays that are incoming to the camera after being reflected on a mirror. As noted, the isopixel curves intersect on the optical axis at different points $\vec{p}_c = [p_c, 0, 0]^T$, with $c \in \{1, \dots, n\}$, n being the number of the extracted isopixel curves, and c denoting a single curve. Through error minimization, the slopes can be updated so that all the isopixel curves intersect on the optical axis. The point of intersection is the new viewpoint of the optical system, and is selected to be $\vec{p}_0 = [\text{median}(p_c), 0, 0]^T$. The parametrizing functions of the updated isopixel curves are shown in Fig. 5.3 (dashed line). This simplification solves the projection problem without introducing errors. The isopixel curve for every pixel on the aerial image is estimated from:

$$\lambda = a\|\vec{m}\|^3 + b\|\vec{m}\|^2 + c\|\vec{m}\| + d \quad (5.2)$$

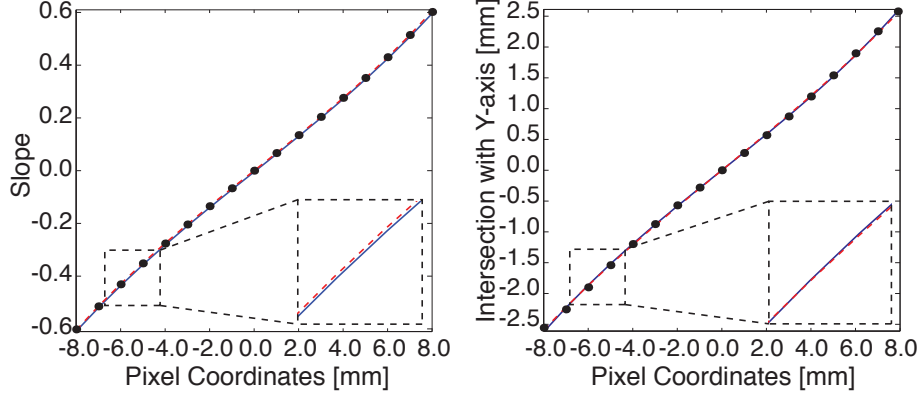


Figure 5.3: Parametrization polynomials for the isopixel curves of the optical system of Fig. 5.1(b). Solid line: Fitted third-order polynomials for the slope and the intersection with the y -axis, respectively. Dashed line: Updated polynomials resulting in a single viewpoint for the system. The solid and dashed lines are barely distinguishable, which justifies the proposed simplification.

where λ is the slope of the isopixel curve; $\vec{\mathbf{m}} = [0, m_j]^T$ are the coordinates on the aerial image (2D case); and a , b , c , and d , are the coefficients of the fitted 3rd-order polynomial. The calculated slope λ is the slope of the ray that connects the intraocular point $\vec{\mathbf{X}}$ with the single viewpoint $\vec{\mathbf{p}}_0$.

The projection in the two-dimensional case is given by the equations:

$$\vec{\mathbf{v}} = \vec{\mathbf{X}} - \vec{\mathbf{p}}_0 \quad (5.3)$$

$$\lambda = \tan(\arccos(\vec{\mathbf{v}}^T \hat{\mathbf{x}})) \quad (5.4)$$

$$\|\vec{\mathbf{m}}\| = -\frac{b}{3a} - \frac{1}{3a} \sqrt[3]{S_1} - \frac{1}{3a} \sqrt[3]{S_2} \quad (5.5)$$

where $\hat{\mathbf{x}} = [1, 0, 0]^T$ is the unit vector along the x -axis, and:

$$S_1 = \frac{A + D}{2} \quad (5.6)$$

$$S_2 = \frac{A - D}{2} \quad (5.7)$$

$$A = 2b^3 - 9abc + 27a^2(d - \lambda_c) \quad (5.8)$$

$$D = \sqrt{A^2 - 4(b^2 - 3ac)^3} \quad (5.9)$$

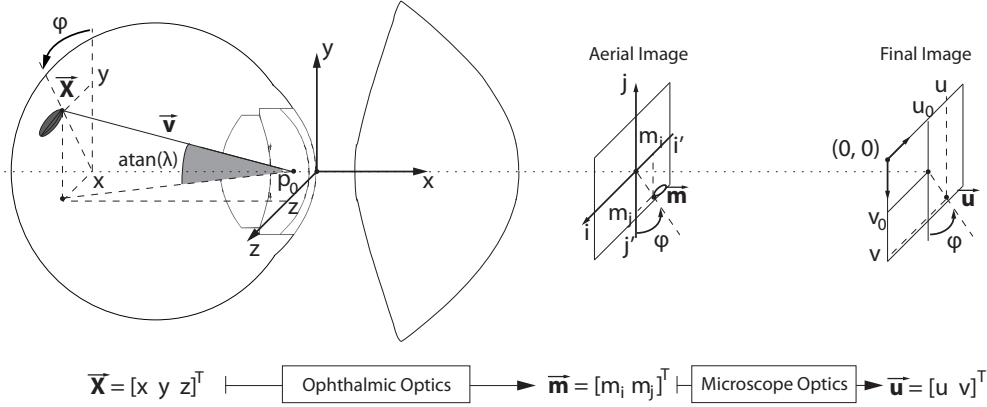


Figure 5.4: Projection of intraocular objects in three dimensions: The 3D point $\vec{\mathbf{X}}$ is projected through the eye optics and the condensing lens to the aerial image point $\vec{\mathbf{m}}$, with the angle ϕ preserved due to the rotational symmetry. The aerial image point $\vec{\mathbf{m}}$ is orthographically projected through the microscope's optics to the image sensor plane at the pixel coordinates $\vec{\mathbf{u}}$. The scale of the orthographic projection is assumed to be unity for ease of illustration.

i.e., the real solution of (5.2). Since the parametrizing functions of Fig. 5.3 are “one-to-one” the projection of an intraocular point is unambiguous. The projections of objects, however, can be ambiguous, as is also the case in perspective projection.

The three-dimensional case is a simple extension due to the rotational symmetry of the optical system; the azimuth angle ϕ between vector $\vec{\mathbf{X}}$ and the y -axis is equal to the angle between $\vec{\mathbf{m}}$ and the jj' -axis on the image plane (Fig. 5.4). Thus:

$$m_i = \|\vec{\mathbf{m}}\| \cos(\phi + \pi) = -\frac{\|\vec{\mathbf{m}}\|}{\sqrt{1 + \tan^2 \phi}} \quad (5.10)$$

$$m_j = \|\vec{\mathbf{m}}\| \sin(\phi + \pi) = -\frac{\|\vec{\mathbf{m}}\| \tan \phi}{\sqrt{1 + \tan^2 \phi}} \quad (5.11)$$

where $\tan \phi \equiv z/y$.

The above algorithm describe the creation of the aerial image. Normally, an additional camera or microscope is used to capture this image. Thus, one needs to consider the cascaded optics; the image created by the optics of the

eye and the condensing lens is transformed by the additional imaging system.

Due to the sizes of the objects of interest, the most commonly used system is the optical microscope. A microscope performs an orthographic projection, i.e. a scaling of the observed scene, based on the equations:

$$\underbrace{\begin{bmatrix} u \\ v \\ 1 \end{bmatrix}}_{\tilde{\mathbf{u}}} = \underbrace{\begin{bmatrix} -\frac{s_u}{k_u} & \sigma & u_0 \\ 0 & -\frac{s_v}{k_v} & v_0 \\ 0 & 0 & 1 \end{bmatrix}}_K \underbrace{\begin{bmatrix} m_i \\ m_j \\ 1 \end{bmatrix}}_{\tilde{\mathbf{m}}} \quad (5.12)$$

where m_i, m_j are given from (5.10)–(5.11), and $\tilde{\mathbf{u}} = [u, v]^T$ are the final pixel coordinates on the microscope’s image sensor (Fig. 5.4). In orthographic projection, the depth of the scene does not affect the image formation.

Finally, the mapping of intraocular points to image coordinates is as follows:

$$\tilde{\mathbf{u}} = K \mathcal{P}(\tilde{\mathbf{X}}) \quad (5.13)$$

where K is the 3x3 microscope matrix from (5.12), and \mathcal{P} is the intraocular projection map from (5.10)–(5.11). Comparison of (5.13) with (5.1) shows that (5.13) can be used in computer vision algorithms that require a known projection model.

5.3 Rigid-Body-Based Intraocular Localization

As mentioned in the introduction, rigid-body pose-estimation works by projecting a model (i.e. a representation of the 3D structure) of the object of interest onto the image based on a known camera projection matrix, and then adapting an estimate of the object’s pose until the projection agrees with the cues perceived on the image. Given a set of vertices $V = \{\tilde{\mathbf{X}}\}$ from the rigid-body model, and a rigid body transformation matrix $e^{\hat{\xi}}$, we estimate the projections of $\tilde{V} = \{e^{\hat{\xi}}\tilde{\mathbf{X}}\}$ on image pixels:

$$\tilde{\mathbf{u}} = K \mathcal{P}(e^{\hat{\xi}}\tilde{\mathbf{X}}) \quad (5.14)$$

	Posterior Radius of Curvature	Thickness
Vitreous Humor		
Intraocular Lens	$\pm 8\%$	
Aqueous Humor		$\pm 10\%$
Cornea	$\pm 4\%$	$\pm 6\%$
	Anterior Radius of Curvature	Refractive Index
Vitreous Humor		$\pm 2\%$
Intraocular Lens	$\pm 4\%$	$\pm 8\%$
Aqueous Humor		$\pm 2\%$
Cornea	$\pm 3\%$	$\pm 3\%$

Table 5.1: Uncertainties in the optical parameters of Navarro’s eye

If O is the set containing the pixels of the segmented object in the image, and $I = \{\vec{u}\}$, then the boundaries ∂I and ∂O are the silhouettes of the projected object and on-image object, respectively.

The goal is to estimate $\hat{\xi}$ so that silhouette ∂I matches ∂O . The discrepancy between ∂I and ∂O gives the error to be minimized. When the minimization converges to a $\hat{\xi}$ value, the new pose is calculated and used in the next frame for initialization. It should be noted that instead of the object contour other cues may be used as well. The minimization function depends on the application.

Magnetic microrobots behave like compass needles when they move in the electromagnetic field; when the orientation of the field changes, they instantly align with the new field orientation. As a result, their orientation can be given from the (known) electromagnetic field orientation, and the pose estimation can be simplified to minimizing only the translational component.

5.4 Sensitivity Analysis

In a clinical setting, the parameters of the optical elements can be measured individually with methods that were summarized in the previous chapter. As discussed in the previous chapter, we need to check our algorithm against uncertainties in the optical modeling.

The sensitivity analysis is a four-step process:

1. Modify the Navarro model by individually perturbing each of the op-

	Posterior Radius of Curvature	Thickness
Vitreous Humor	$\mu_{\max} = 282, \sigma_{\max} = 105$	$\mu_{\max} = 466, \sigma_{\max} = 240$
Intraocular Lens		$\mu_{\max} = 481, \sigma_{\max} = 96$
Aqueous Humor	$\mu_{\max} = 272, \sigma_{\max} = 80$	$\mu_{\max} = 295, \sigma_{\max} = 162$
Cornea		
	Anterior Radius of Curvature	Refractive Index
Vitreous Humor	$\mu_{\max} = 266, \sigma_{\max} = 89$	$\mu_{\max} = 364, \sigma_{\max} = 6$
Intraocular Lens		$\mu_{\max} = 616, \sigma_{\max} = 160$
Aqueous Humor	$\mu_{\max} = 361, \sigma_{\max} = 76$	$\mu_{\max} = 422, \sigma_{\max} = 98$
Cornea		$\mu_{\max} = 283, \sigma_{\max} = 82$

Table 5.2: Worst-case mean errors and standard deviations [um] due to uncertainties in the optical parameters

tical elements.

2. Estimate the new isopixel curves and their parametrization.
3. Project an intraocular object using the perturbed isopixel curves on the image.
4. Use the calculated projection to estimate the position of the object. However, in this case, use the isopixel curves estimated from the unperturbed Navarro model.

We assume a 1 mm-diameter sphere moving in $2D$ in the interior of the perturbed eye in a field-of-view of 70° , and use the algorithm to find its position. The localization errors show how uncertainties in the optical parameters affect our algorithm's performance. Since Navarro's model is based on anatomical data, for the perturbations in the eye parameters we apply the standard deviations reported in the literature. The uncertainties were collected in the previous chapter from various ophthalmology references and are summarized in Table 5.1. Existing calibration techniques can estimate the intrinsic parameters, matrix (K), of the microscope. Thus, we assume no uncertainty in these parameters.

In the previous chapter, it was observed that the isopixel curves are generally robust to optical uncertainties. The sensitivity analysis conducted here supports this conclusion as well. For the creation of Table 5.2, we calculate

the mean error across the entire trajectory for each uncertainty case, and report the worst-case scenario for each parameter. We also report the worst case for the standard deviation. It can be seen that in all examined scenarios, the mean errors across the whole trajectory are usually less than $500\ \mu\text{m}$. Moreover, the maximum standard deviations are on the order of $100\ \mu\text{m}$ in the majority of the examined scenarios. In other words, the expected precision of the algorithm is always high. The mean errors (the accuracy) can be accounted for through calibration. As our discussion in the previous chapter pointed out, biometric measurements of the human retina can be used to improve the accuracy of the localization. For example, the estimated position of a microdevice when resting on the retina should be equal to the axial length of the human eye (i.e. the retinal depth), which can be determined from MRI data.

5.5 Experiments

In this section, we estimate the precision of the proposed algorithm. Our implementation is in Matlab for easy post-processing of the recorded data. The reprojection error is minimized with a version of the Levenberg-Marquardt nonlinear least-squares minimization method [Balda, 2009]. Our experimental setup consists of the electromagnetic control system and an eye model (Fig. 5.5).

The OctoMag electromagnetic control system [Kummer *et al.*, 2010] comprises 8 electromagnetic coils positioned in a hemispherical array, and allows precise 5-DOF control of magnetic microrobots. Localization of the microrobots is required in order to accurately set the electromagnetic field at the robot's position. The orientation can be taken from the magnetic field controller.

For visual feedback, the OctoMag has two orthogonally positioned microscopes. A Leica M80 microscope at 2.0x magnification observes the workspace from the top, and a Basler A602fc camera equipped with an Edmund Optics VZM 200i 0.5x zoom lens observes the workspace from the side. Through calibration, the effective pixel size for both imaging systems can be calculated.

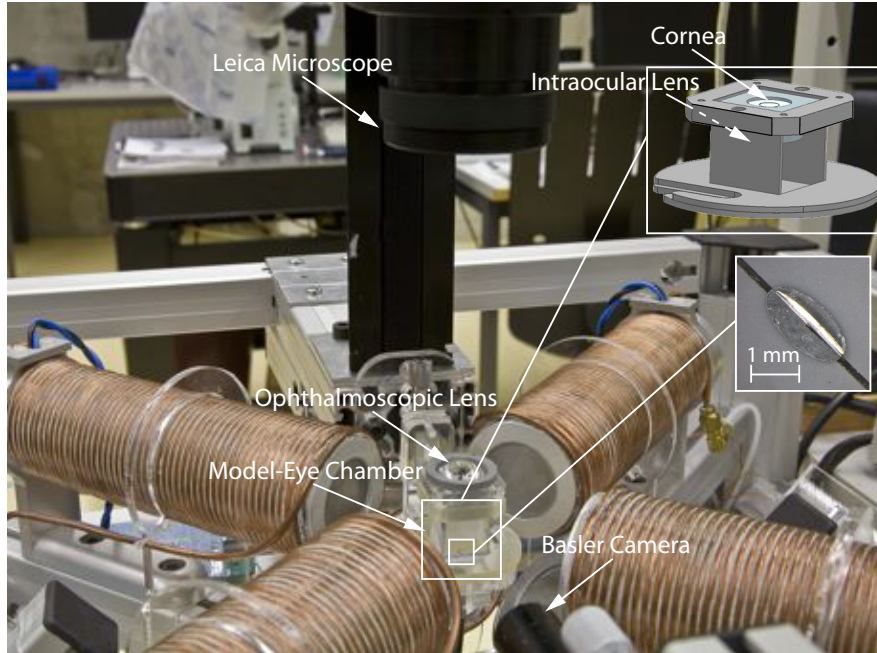


Figure 5.5: The OctoMag control system, equipped with two cameras. The top camera is mounted on a Leica M80 microscope, and the side camera is mounted on a Edmund Optics VZM 200i zoom lens. The chamber with the fabricated model-eye lenses can also be seen.

The microdevice moves in a transparent chamber. Tracking is performed on the image domain using simple background subtraction and morphological filtering. The existence of the orthogonal cameras allows easy 3D localization through triangulation.

The work presented in the previous chapter, where we discussed focus-based localization, uses a model eye with a single lens that works in air. In this chapter we conduct experiments in liquids, and thus, a new model eye is designed. It consists of two double-convex lenses that act as the cornea and the intraocular lens, respectively (Fig. 5.6). The optical parameters are selected based on the population-based parameters of Navarro’s schematic eye. However, adjustments are necessary because the refractive indices of the cornea and lens are difficult to find in solid materials (if at all) ¹. The model

¹For example, the refractive index of the cornea is close to that of cryolite, an uncommon mineral.

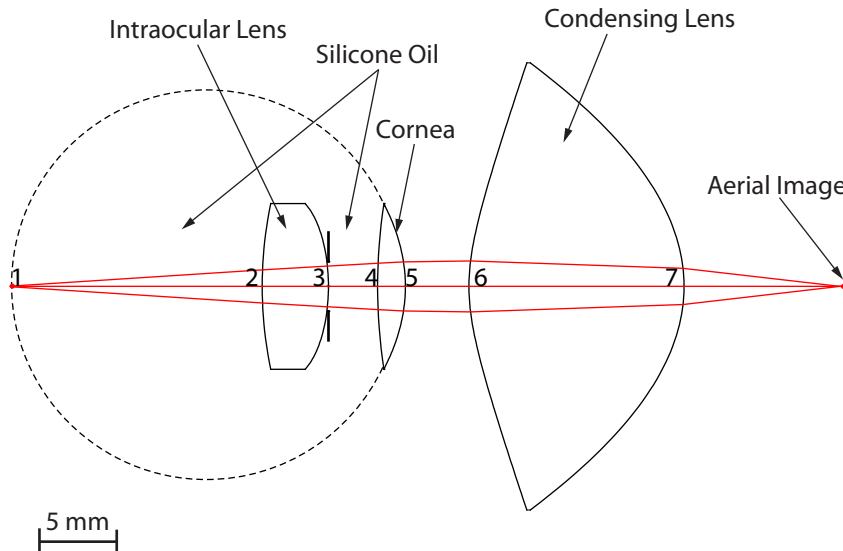


Figure 5.6: The lenses of the new model-eye system. For the precision-evaluation experiments, the lenses are aligned in a transparent chamber that allows observation from the top and the side. Later, the lenses are positioned in the model eye of [Gwb International, Ltd., 2010], allowing the microrobot to move on the eye’s hand-painted retina but with no side imaging available.

eye is filled with silicone oil. The focal length is ~ 26 mm, and the diameter of the pupil is 3 mm, as is also in Navarro’s eye. The optical parameters are given in Table 5.3. The lenses and pupil are aligned mechanically in a scaffold, and the eye is positioned in the center of the workspace of the OctoMag. All the lenses are fabricated by Sumipro BV. The isopixel curves and the projection model for the optical system is extracted using the method described in the previous sections.

In our set of experiments, the camera mounted on the Leica microscope is a Basler A602f camera that has a $9.9 \mu\text{m} \times 9.9 \mu\text{m}$ sensing element. The top camera observes the scene through the pupil, and the image is affected by the cascade of lenses and microscope. The side camera, a Basler A602f as well, observes a simple orthographic projection of the “interior” of the eye. The recorded images are post-processed to estimate the actual position from the top-camera images and compare it with the estimates from the orthographic projection of the side camera, which gives the ground truth values.

Surface	Radius	Conic Constant	Thickness	Index
1	11.5 mm	0.00	15.50 mm	1.403
2	24.73 mm	0.00	4.00 mm	1.492
3	-12.27 mm	3.80	2.97 mm	1.403
4	32.36 mm	0.00	1.68 mm	1.415
5	9.48 mm	-1.20	3.84 mm	1.000
6	11.65 mm	-9.24	13.00 mm	1.531
7	-9.48 mm	-1.07	∞	1.000

Table 5.3: Optical parameters of the new eye system.

Both cameras were calibrated using a calibration pattern, and the effective pixel size was calculated as $2.07 \mu\text{m} \times 2.07 \mu\text{m}$ and $2.04 \mu\text{m} \times 2.04 \mu\text{m}$, for the top imaging system and the side imaging system, respectively. The top camera was calibrated before introducing the eye model.

The closed-loop control of the microrobot is handled by a simple PD controller. The z -component of the position is given online by the side camera, and x , y components are given by a simple scaling from the top camera. These estimates are erroneous, since the optics are not considered online in this experiment. However, the closed-loop microrobot-position controller successfully servos the microrobot to these erroneous estimates.

The trajectories we examine are spirals spanning approximately 6 mm top-to-bottom and 7 mm side-to-side. The diameter of the spirals increases as the microrobot moves towards the intraocular lens. We perform experiments with a $2 \text{ mm} \times 1 \text{ mm} \times 1 \text{ mm}$ microrobot composed of two elliptical CoNi plates and with a $500 \mu\text{m}$ -diameter NdFeB sphere. The CoNi microrobot is steered in two different orientations that are given by the magnetic field. Both devices are modeled as ellipsoids and their projected silhouettes as ellipses. We use this information to build the minimization error for localization:

$$F = (\alpha_I - \alpha_O)^2 + (\beta_I - \beta_O)^2 + (u_I - u_O)^2 + (v_I - v_O)^2 + (\phi_I - \phi_O)^2 \quad (5.15)$$

where $\{\alpha_i, \beta_i, u_i, v_i, \phi_i\}$ with $i \in \{I, O\}$ are the major axis, minor axis, center coordinates, and orientation of ellipses fitted to the silhouettes ∂I and ∂O , respectively. The errors can be assigned different weights, e.g. the angle error can be attenuated, since it is mainly governed by the magnetic field

Experiment	1	2	3
	x-axis		
Mean Error	93 ± 49	46 ± 30	80 ± 54
Maximum Error	248	145	280
	z-axis		
Mean Error	249 ± 177	310 ± 192	171 ± 119
Maximum Error	721	836	530

Table 5.4: Mean error, standard deviation, and maximum error [um]

orientation.

In the first experiment (Fig. 5.7(a)) the microrobot is aligned with the x -axis. The microrobot appears bigger near the intraocular lens, and this is leveraged by our algorithm. It is nontrivial to estimate not only the depth of the device (recall that we study single-camera localization), but also the x and y coordinates; this is not a perspective projection scenario. In the second experiment (Fig. 5.7(b)) the microrobot is aligned with the z -axis. Since it is composed of two elliptical plates, it is harder to track in this orientation, and tracking errors have a greater impact on the fitted ellipse used for localization. Moreover, notice that even though the device looks perpendicular when at the center of the image, it appears “tilted” as it moves to the image side; this is an artifact of the cascaded optics, and our algorithm interprets it successfully. In the third experiment (Fig. 5.7(c)) we evaluate the algorithm’s capabilities with a smaller device. We use a 0.5 mm-diameter NdFeB sphere and keep the magnification constant.

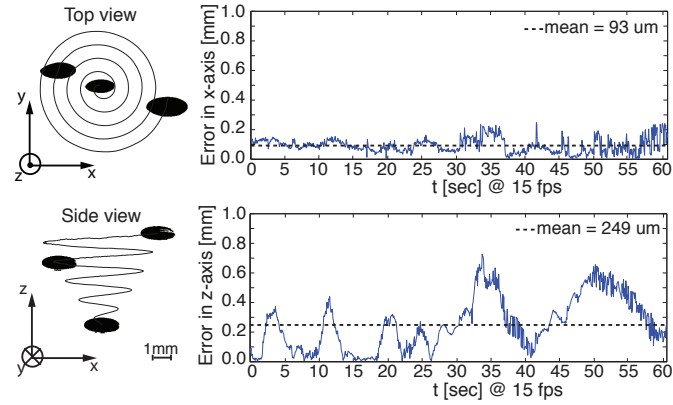
The mean errors and standard deviations are reported in Table 5.4. The experimental results verify our approach, as our algorithm takes into account all the elements of the refractive optical system, and performs robustly at different scales. The extracted position information has even greater precision than what is required by the electromagnetic control system.

5.6 Conclusions

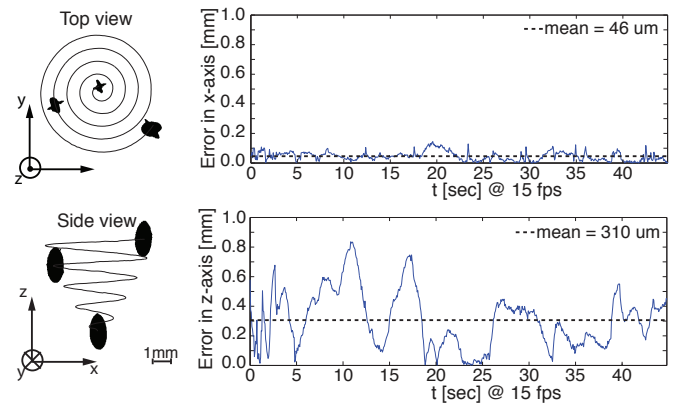
We presented a model-based localization algorithm for the system of the human eye and tested it in a fabricated human-like eye model for different

microrobots under different orientations. This algorithm can be generalized, as the concept of the isopixel curves can be extended for various systems with refractive elements. In systems where stereo-imaging is not available and where focus-based methods seem inappropriate, careful consideration of the optics can allow monocular device localization with high accuracy.

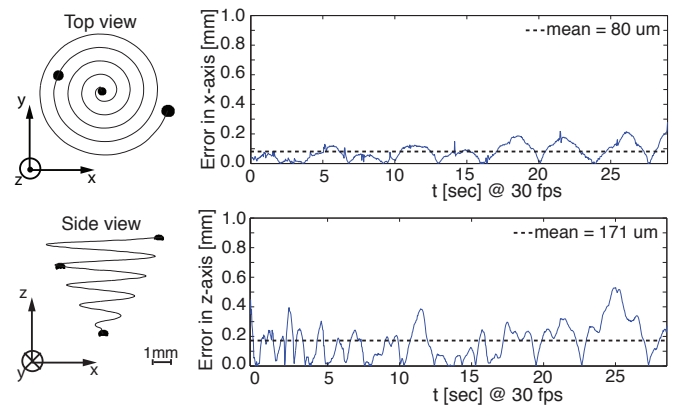
In the following chapter, we apply our methodology for visual servoing using the electromagnetic field and the microrobotic devices.



(a)



(b)



(c)

Figure 5.7: All errors are with respect to the values given from the side camera. (a) Results for a $2\text{ mm} \times 1\text{ mm} \times 1\text{ mm}$ CoNi microrobot aligned along the x -axis, (b) Results for a $2\text{ mm} \times 1\text{ mm} \times 1\text{ mm}$ CoNi microrobot aligned along the z -axis, and (c) Results for a $0.5\text{ mm} \times 0.5\text{ mm} \times 0.5\text{ mm}$ NdFeB bead.

Chapter 6

Monocular Visual Servoing of Intraocular Microdevices

In the previous chapter we developed and evaluated a localization algorithm, which, using a rigid-body model of the microdevice of interest, leverages the cascade of refractive optics and performs three-dimensional localization. In this chapter, we use this algorithm to provide feedback to the electromagnetic field controller. Additionally, we perform monocular visual servoing in a model eye in a fully-automated and supervised mode.

Visual-servoing approaches are traditionally classified as position-based or image-based [Hutchinson *et al.*, 1996]. Visual servo systems typically use one of two camera configurations: end-effector mounted or fixed in the workspace. The first type of systems is called an eye-in-hand configuration. Since the above classification was published, a variety of new visual servoing techniques have been reported. An updated classification can be found in [Chaumette and Hutchinson, 2006; 2007].

In position-based visual servoing features are extracted from images and are used to estimate a target pose. Then, an error between the current configuration of the robot and its desired pose is calculated. The error is defined in the task-space. Position-based visual servoing separates the computer vision task of estimating the target pose from the control task, which involves moving the manipulator to the desired position.

In image-based visual servoing, the error is calculated in the image space. Based on a calibrated camera matrix, the image Jacobian that relates the end-effector motion to feature motion on the image is calculated. The inverse of the Jacobian matrix can provide motion directives to the actuators in order for the image error to be minimized. Usually, image-based servoing requires a reference image.

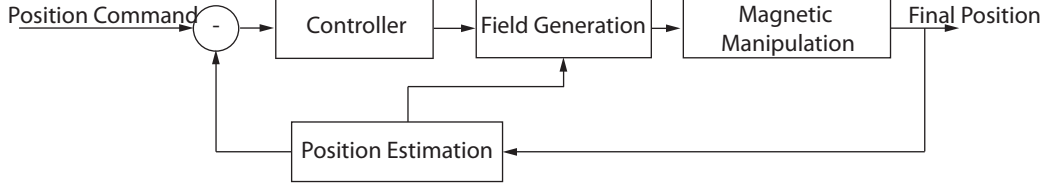


Figure 6.1: Schematic diagram of the different components involved in the servoing of the microrobots using the electromagnetic control system.

The visual-servoing problem that we address has a camera fixed on the workspace. It is unique in that it involves two servoing loops. The information of the position of the microrobot is required to generate the desired electromagnetic field. In addition, the microrobot is servoed to a desired position. Figure 6.1 illustrates the servoing problem.

Our visual servoing algorithm is implemented in C++ for real-time experiments. The pose is estimated with a C++ version of the algorithm of the previous chapter, and the reprojection error is minimized with the Levenberg-Marquardt nonlinear least-squares minimization method [Lourakis, 2004]. The devices are modeled as ellipsoids, and their projections as ellipses. We perform image processing using OpenCV, a C/C++ computer vision library that enables real-time image processing.

Our code is a plugin for Daedalus, a GUI package written in Qt 4.3. It allows software to be written in a decoupled fashion, and enables rapid exchange and sharing of modules. Daedalus defines a number of class interfaces for different tasks commonly performed in the system, such as acquiring images, logging data, tracking images, visual servoing, or editing system parameters. These interfaces are then implemented by a series of plugins, which are entirely separate from the main system. This loose-coupling allows for plugins to subscribe or publish data pipelines for transmission through the system. Each plugin can then be selectively used or omitted depending on the task at hand [Kratochvil, 2008].

The plugin tracks the robot, estimates its position, and sends it to the electromagnetic field controller. Figure 6.2 shows a screenshot of the interface

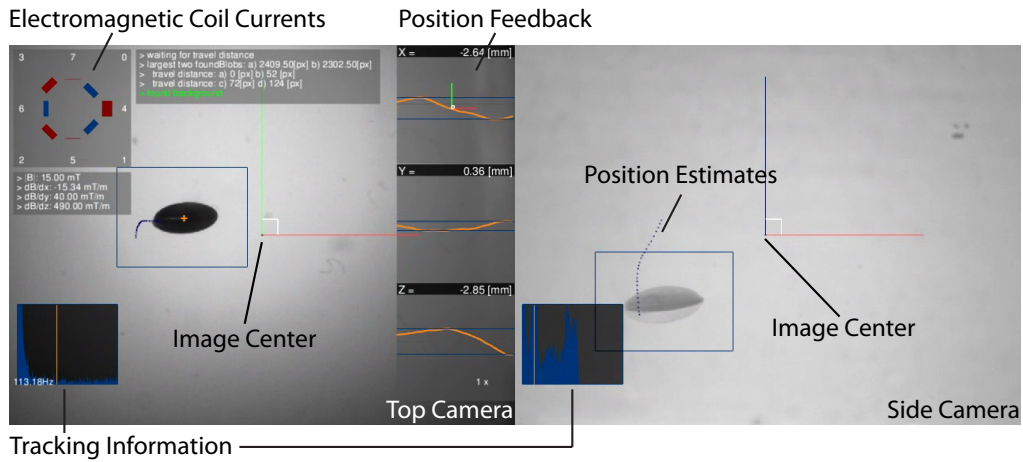


Figure 6.2: Screenshot of the implemented interface. The image on the left taken by the top camera is the scene observed through the pupil of the eye, and the image on the right is observed by the side camera. The dotted lines on the left image show the history of the device’s location. The dotted lines on the right image show the projection of the estimated pose on the side camera.

and the reported visual data.

6.1 Visually Servoing the Electromagnetic Field

Earnshaw’s theorem states that there can be no stable static equilibria using ferromagnetism [Cullity and Graham, 2009]. To maintain a “stable” position of the microrobot, in other words to minimize its drift, position feedback is required to calculate the magnetic field at the robot’s position.

Even though we have a projection map for our optical system that could relate the motion of the microrobot to motions in the image features (from the previous chapter), we cannot employ image-based visual servoing for our problem. This is a position-based visual-servoing problem in which what is being “servoed” is the electromagnetic field. There is no error minimization, but the device’s position is an intrinsic parameter required by the field controller.

The microrobot sinks under its own weight, and this is an inherent dif-

Location	Velocity		
	Open loop	Single-camera	Orthogonal cameras
upper-middle	264 ± 15	53 ± 14	106 ± 15
middle-middle	258 ± 193	82 ± 47	101 ± 68
lower-middle	159 ± 9	62 ± 6	62 ± 19
upper-right	486 ± 11	140 ± 10	147 ± 10
middle-right	609 ± 4	178 ± 2	207 ± 8
lower-right	495 ± 53	129 ± 2	208 ± 4

Table 6.1: Mean velocity and standard deviation [$\mu\text{m}/\text{sec}$] due to magnetic drift for different cases of position feedback

ference of our system with traditional robotic systems, where each motor causes an identifiable motion. Additionally, traditional systems possess proprioception, which means that the position of the end-effector can be known through the values of the individual actuators and the forward kinematics. In our case, in order to understand the effect of the individual coil-currents to the microrobot’s position, we need the ability to estimate changes in its location.

In [Kummer *et al.*, 2010] the drift of the OctoMag was examined as well. For various microrobot orientations, the worst drift at the center of the workspace during open-loop control is $150 \mu\text{m}/\text{s}$ for a 2 mm-long CoNi microrobot and $50 \mu\text{m}/\text{s}$ for a smaller 500 μm -long Ni microrobot. At the boundaries of the workspace these values increase to $720 \mu\text{m}/\text{s}$ and $140 \mu\text{m}/\text{s}$, respectively. With position feedback for field generation, the drifts at the workspace boundaries reduce to $550 \mu\text{m}/\text{s}$ and $60 \mu\text{m}/\text{s}$ for the CoNi and Ni microrobot, respectively. Scaling the robot down leads to a reduction in the drift and improves the device’s stability. However, this leads to an inability to apply high forces, as magnetic forces scale with respect to volume.

We use a 2 mm-long CoNi microrobot aligned along the x -axis. This configuration is the hardest-case scenario for the electromagnetic control system. The microrobot is manually controlled to several locations in the workspace (upper-middle, middle-middle, lower-middle, upper-right, middle-right, lower-right), and is left to drift for 3 seconds. We examine three cases: (a) the electromagnetic field is constant, (b) the electromagnetic field is cal-

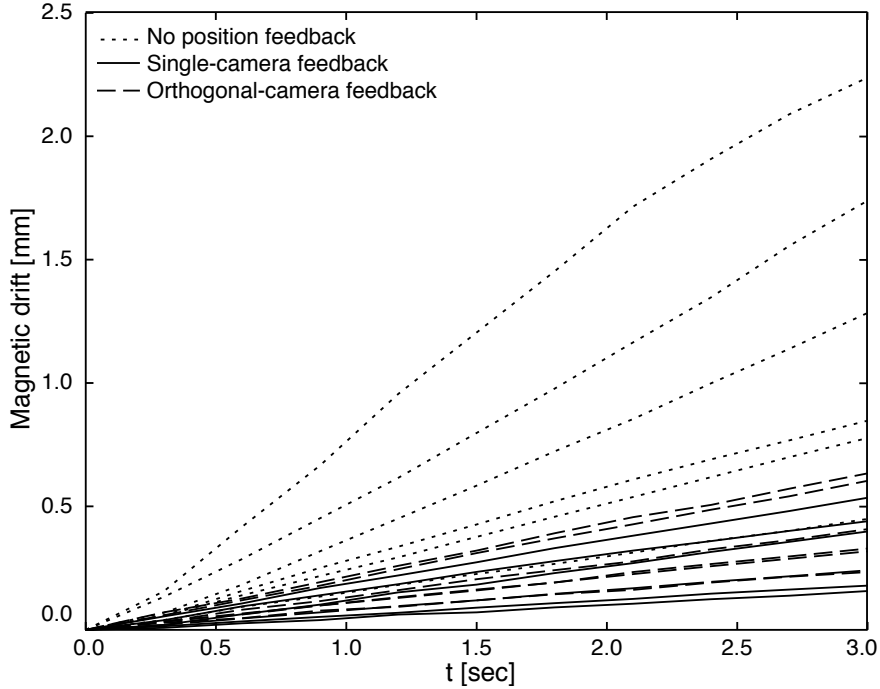


Figure 6.3: Magnetic drift for a $2\text{ mm} \times 1\text{ mm} \times 1\text{ mm}$ CoNi microrobot aligned along the x-axis.

culated at the position of the microrobot which is given by our localization algorithm, and (c) the electromagnetic field is calculated at the position of the microrobot which is given through the orthogonal camera system with the model-eye optics removed. The electromagnetic field is manually adjusted for local stability at the center of the workspace and each case is examined 5 times. We are using two Basler A602f cameras for imaging.

Figure 6.3 shows the drift for all experiments, and Table 6.1 shows the mean velocity and the standard deviation from the 5 experimental runs, for each of the 6 examined positions, and the 3 different feedback cases. Figure 6.3 and Table 6.1 indicate that position feedback from the proposed single-camera localization algorithm diminishes the drift to the levels achieved by the orthogonal-camera localization method.

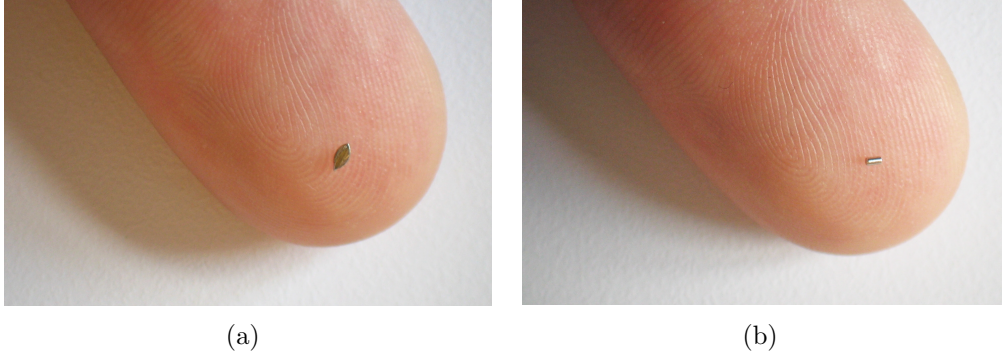


Figure 6.4: (a) A 2mm-long CoNi microrobot, and (b) a 1 mm-long NdFeB microrobots.

6.2 Visually Servoing Microrobots

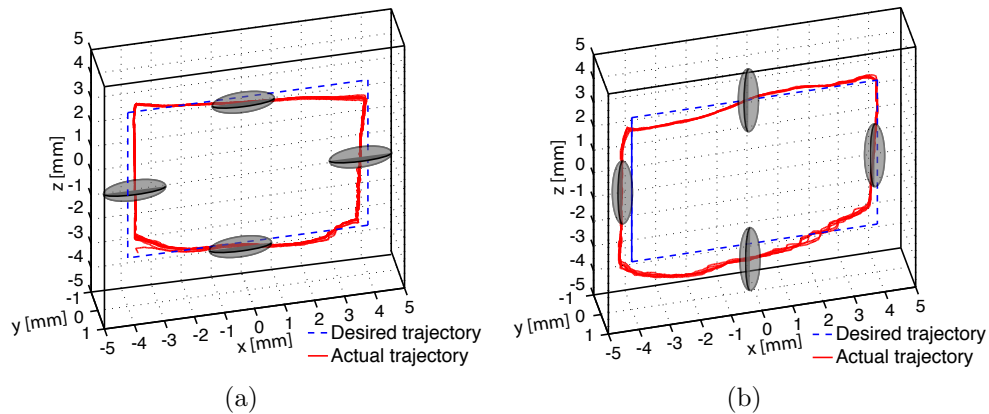


Figure 6.5: Results of positioned-based visual servoing of a 2 mm-long CoNi microrobot aligned with (a) the x -axis, and (b) z -axis.

Using the microrobot's position estimated by our algorithm, the magnetic field and the position of the microrobot can be controlled. The latter can be achieved through an additional feedback controller that minimizes the error between the estimated position of the microrobot and its desired position. This constitutes the secondary visual-servoing problem, where what is being "servoed" is the actual microdevice. We performed fully automated servoing of a 2 mm-long CoNi microrobot in two orientations, and semi-automated

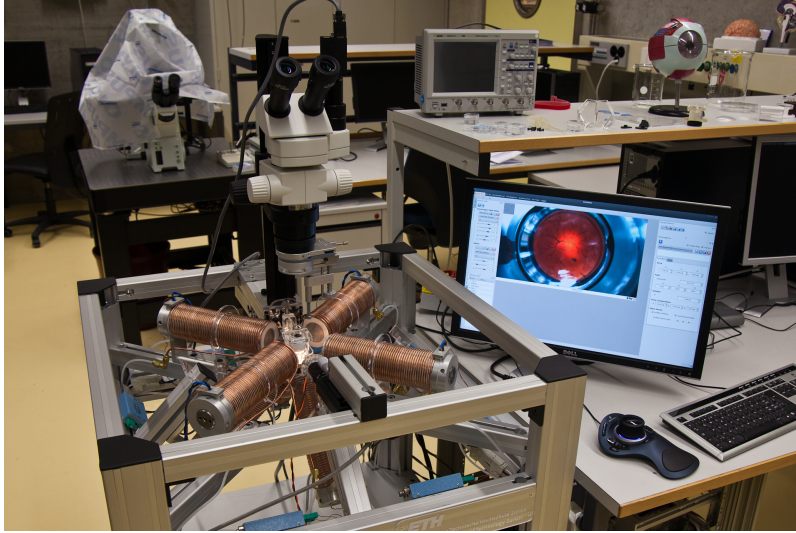


Figure 6.6: The OctoMag control system, equipped with two Basler A602f cameras. The top camera is mounted on a Leica M80 microscope, and the side camera is mounted on a Edmund Optics VZM 200i zoom lens. This image was taken using the model eye of [Gwb International, Ltd., 2010] and the BIOM, a system that enables fine-focusing motions of a condensing lens.

servoing of a 1 mm-long NdFeB cylinder in a model eye with a hand-painted retina. The devices can be seen in Fig. 6.4.

Figures 6.5 shows the results of servoing the CoNi microrobot using a PD controller. The actual trajectory is estimated from the values of the side camera, and the desired trajectory is an $8\text{ mm} \times 6\text{ mm}$ square. The errors are due to inaccuracy in the estimates of the localization algorithm. These experiments could also be conducted as image-based visual servoing using the projection model and the detected microrobot. However, the position information is readily available. The side camera is a Basler A602f model as in the previous experiments, but on the Leica microscope we mount a Grasshopper-14S5M/C from Point-Grey to achieve higher resolution and field-of-view. The sensing element is $6.45\ \mu\text{m} \times 6.45\ \mu\text{m}$. The effective pixel size is calculated at $14.3\ \mu\text{m} \times 14.3\ \mu\text{m}$. The data are recorded at 15 fps.

In our final experiment, we place the lenses in a model eye with a hand-painted retina [Gwb International, Ltd., 2010] (Fig. 6.6). No side imaging is available. We use a $1\text{ mm} \times 0.5\text{ mm} \times 0.5\text{ mm}$ NdFeB cylindrical microrobot,

which is tracked using background subtraction and is modeled as a superquadric. The dimensions of the model eye are known, and we can calibrate the algorithm by estimating the microrobot's position when it lies on the known retinal depth. We use the extracted 3D position to control the electromagnetic field, and a PD controller to control the x and y position of the microrobot. The z component can be manually controlled by the user. The estimated depth is shown in the form of a bar: the user can set a depth as a "zero-level", and the bar indicates the proximity of the device to this "zero-level", alerting the user when the distance is small. Such a system can be easily accepted by clinicians as it allows supervisory control of the system, direct interaction with the microrobotic device, and gives additional information about the device's proximity to the retina. Figure 6.7 shows screenshots of the microrobot moving towards the optic disk of the model eye. Figure 6.8 shows the interface presented to the user.

6.3 Conclusions

In this chapter we have demonstrated how our localization method can minimize the drift in the OctoMag electromagnetic control system using a single camera. We also performed visual-servoing experiments in a model eye, both in a fully-automatic mode and under supervision.

By designing lenses and coupling them with a microscope, the localization algorithm can provide position information to magnetic-field controllers. This demonstrates the potential for a localization method of microdevices in electromagnetic control systems that are not equipped with stereo imaging.

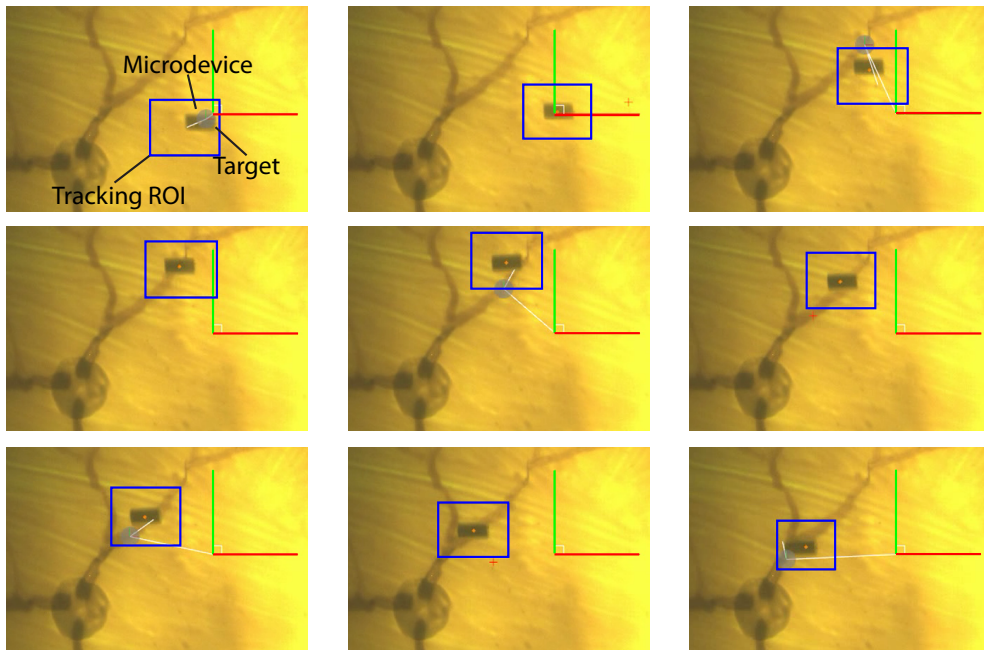


Figure 6.7: The microrobot is tracked using background subtraction, and its 3D position is sent to the electromagnetic field controller to minimize the drift. Additionally, its 2D position is used to servo the device to user specified points which are represented as gray circles. Images are parts cropped from the original sequence.

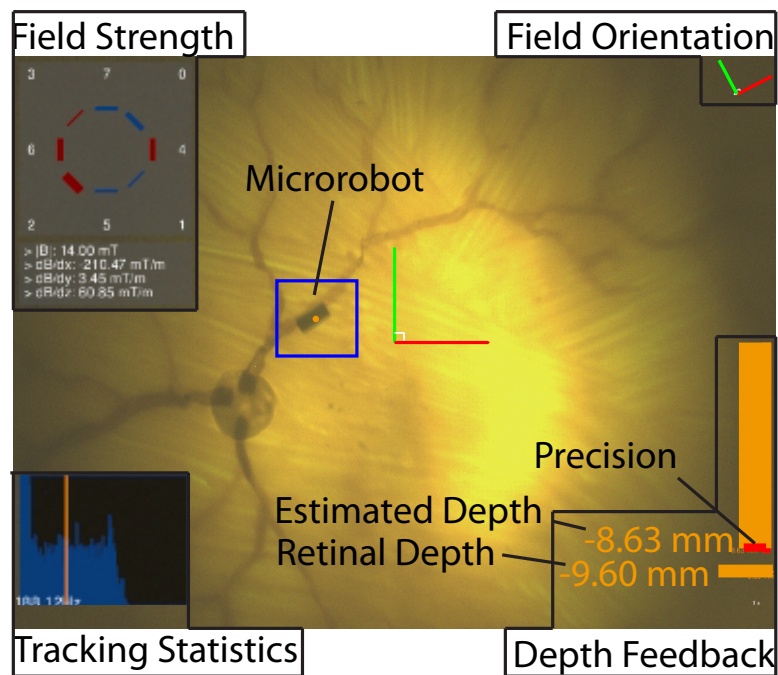


Figure 6.8: The microrobot is tracked using background subtraction, and its position is calculated from the intraocular localization algorithm. The depth is presented to the user as a bar in orange or red depending on whether the robot is past a threshold of proximity to the retina. The precision, the variance of a moving average filter on the depth, is shown in inverse color. The depth information is fed to the electromagnetic field controller for drift minimization, and can be used to control the position of the microrobot. This allows for a teleoperated system that visually provides the extracted information to the surgeon.

Chapter 7

In Vitro and Ex Vivo Experiments with Intraocular Microdevices

At this point in the dissertation we have performed a theoretical examination of the image formation for intraocular microdevices, and we have developed algorithms that use this information to perform image-based localization. Our algorithms were tested in existing and fabricated human-eye models with success.

In this chapter, we investigate the feasibility of performing intraocular operations using microrobots. More specifically, we are interested in understanding whether microrobotic agents are able to move in the interior of the human eye without requiring a vitrectomy. We only consider magnetic microrobots that move by gradient forces using the Octomag; in other words, we do not consider helical microswimmers like the ones reported in [Zhang *et al.*, 2009]. We conduct experiments in synthesized vitreous humor to evaluate the device's motion capability in the viscoelastic environment of the vitreous humor, and ex-vivo experiments in porcine cadaver eyes in order to understand the real-life complexities of our approach.

What should be noted beforehand, is that there are several pathological cases that require the removal of the vitreous humor regardless of the subsequent surgery. For example, in diabetic retinopathy, the vitreous can become opaque due to bleeding. In all these cases, a vitreous substitute can be selected (e.g. it can be silicone oil), so that microrobotic devices can easily operate in it.

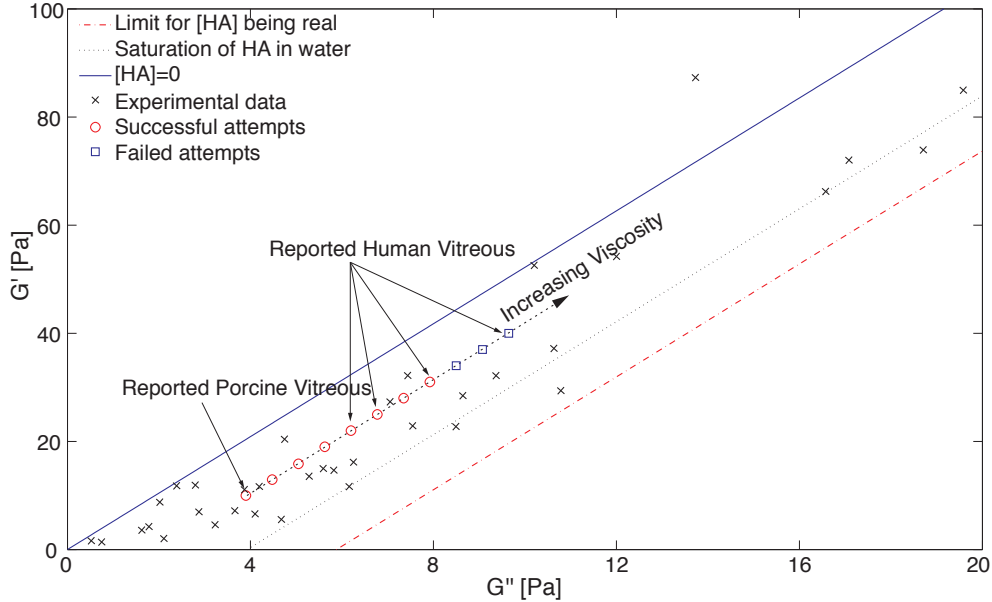


Figure 7.1: Motion experiments with artificial vitreous humor. The storage and loss moduli are from [Kummer *et al.*, 2007]. The red circles indicate successful movement attempts and the blue boxes indicate that the insert was unable to translate. The crosses are the different fluids examined in [Kummer *et al.*, 2007] to extract the relationship between A_g , HA, storage and loss. Image adapted from [Kummer *et al.*, 2007].

7.1 Experiments with Artificial Vitreous Humors

As already mentioned in the introductory chapters, the vitreous humor is a viscoelastic gel-like substance that fills the posterior cavity of the human eye. During ophthalmic surgery, the vitreous needs to be removed and exchanged with a less viscous fluid. The substitute needs to be biocompatible, and with similar density and refractive index as the natural vitreous. Historically, vitreous substitutes ranging from collagen and hyaluronic acid to gases, silicone oils, and hydrogels have been considered. The viscoelastic properties of these materials differ from that of the human-eye vitreous however, and finding an optimal vitreous substitute is an open research problem [Soman and Banerjee, 2003].

In [Kummer *et al.*, 2007], a protocol is presented that can be used to create fluids that have the desired viscoelastic properties. These fluids consist of

Case	1	2	3	4	5	6	7
AG (mg/mL)	1.098	1.27	1.42	1.56	1.68	1.80	1.91
HA (mg/mL)	2.21						
Comment	Pig Eye [2]					Human Eye [2]	

Table 7.1: Quantities of AG, and HA for 100 mL of water. Cases 1–7.

Case	8	9	10	11
AG (mg/mL)	2.014	2.11	2.21	2.30
HA (mg/mL)	2.21			
Comment	Human Eye [2]			Human Eye [2]

Table 7.2: Quantities of AG, and HA for 100 mL of water. Cases 8–11.

water (H₂O), agar (AG), and hyaluronic acid (HA). Water is 99% of the natural vitreous humor, and hyaluronic acid gives it some of its mechanical properties [Nickerson, 2005]. In synthetic vitreous humor, agar is added to give elasticity to the mixture. Varying amounts of these elements affect storage modulus and loss modulus for the final mixture in a defined way.

Based on this protocol, we synthesized 11 fluids with varying degrees of viscoelasticity (Fig. 7.1), starting from a fluid that resembles porcine-eye vitreous humor, and covering varying cases of human vitreous humors as reported in [Nickerson, 2005]. The viscoelastic properties measured for the human eye vitreous are scarce and not statistically relevant. Nevertheless, the data is one of the few reported in the literature, and synthesizing fluids with similar properties provides an understanding of our ability to move microrobots in fluids of varying viscosity and elasticity. It should be noted that the human vitreous liquifies with age, and this is expected to facilitate moving microrobotic devices.

According to the protocol of [Kummer *et al.*, 2007], we can fix the amount of HA in solution, and vary only the amount of AgG to achieve the desired mechanical properties. The procedure starts with heating the water near 100°, and then adding the agar and hyaluronic acid. The amounts are measured with a balanced microscale. The mixture is stirred rigorously with magnetic steerers while it sits on a hotplate that guarantees a temperature for the water near boiling. Once the solution is fully transparent, it is re-

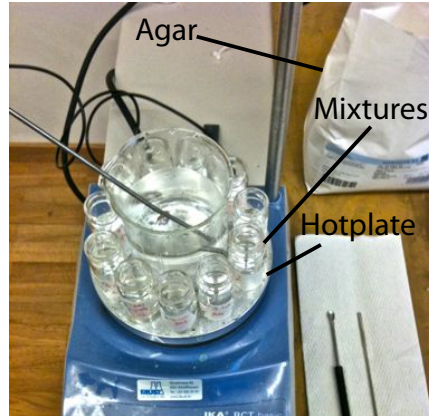


Figure 7.2: The different fluids were prepared by mixing water, agar, and hyaluronic acid at appropriate quantities. The image shows the prepared vials on a hotplate.

moved from the hotplate and left to cool overnight. Table. 7.1 and Table. 7.2 report the amounts of agar and hyaluronic acid for the different fluids. The mixtures were placed in glass vials (Fig. 7.2).

Figure 7.1 shows the storage and loss moduli for different synthesized vitreous humors. The crosses correspond to mixtures that were prepared in [Kummer *et al.*, 2007] in order to extract the relationship between the amount of HA and AG, and the storage and loss moduli. This relationship was quantified with formulas that can be satisfied when the values of HA lie between the solid and dotted lines in Fig. 7.1. Our experiments are depicted as circles and squares; successful attempts are shown as circles, and failed attempts as squares.

We experimented using 2 mm-long CoNi devices, and 1 mm-long NdFeB microrobots. The devices were controlled using the OctoMag. Figure 7.3 shows that even in the thinnest of the synthesized fluids, a fluid with similar viscoelastic properties to the porcine vitreous, the CoNi microrobots are able to move only by tumbling. The NdFeB microrobot was able to move in a greater range of mediums, from the simulated porcine vitreous to reported human-eye values.

These results indicate that it is difficult to use CoNi microdevices intraocularly without performing a vitrectomy, but based on our experimental

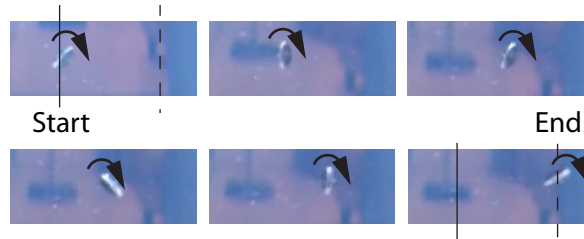


Figure 7.3: A 2 mm-long CoNi microrobot that moves in a simulated porcine vitreous humor by tumbling.

conditions, this is possible with NdFeB microrobots. This is not surprising since much higher forces can be exercised on the permanent magnetic microrobot (NdFeB) than on the soft-magnetic one (CoNi). Of course, re-engineering the electromagnetic field generation system can lead to increased forces as well, but there are clear limits to this approach.

7.2 Experiments with Cadaver Porcine Eyes

Porcine eyes (Fig. 7.4(a)) have similar properties with the human eye and possess similarly structured vasculature. Porcine eyes are used as a model for the human eye. They are easily available from slaughterhouses and, contrary to sheep eyes, are safe to use concerning the transmittance of diseases. They differ from the human eye in a reduced thickness of the aqueous chamber (1.5 mm contrary to 3 mm on average), and an increased thickness of the intraocular lens (8 mm contrary to 4 mm on average) [Coile and O’Keefe, 1988]. [Vilipuru and Glasser, 2001] has examples of lenses with 10 mm thickness (Fig. 7.4(b)). This thickness complicates the experimental procedure (e.g. when inserting needles).

Eyes from older pigs are preferred, as the mechanical properties of the vitreous will be similar to those of an aging human², but it can be difficult to ensure older eyes are available. Additionally, the typical procedure for animal slaughtering, i.e. killing the animal, placing it in hot water to loosen the hair and skin, and skinning it, adversely affects the optical elements of the eyes. Ideally, the eyes are removed prior to the boiling-water process.

²Known through personal communication with ophthalmic surgeons

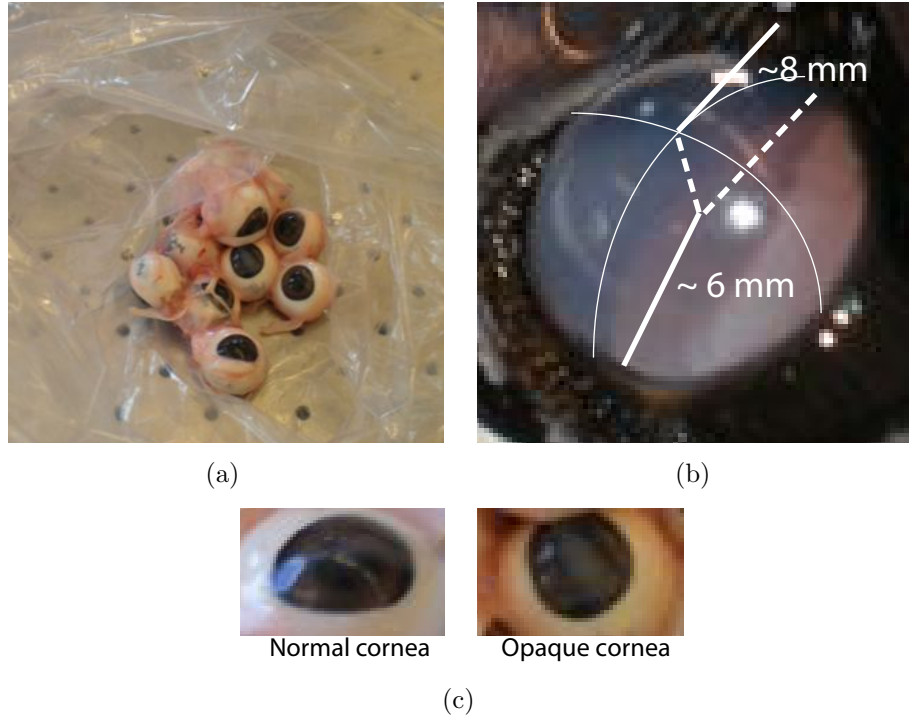


Figure 7.4: (a) The pig eyes, as purchased from the slaughterhouse, (b) dissected porcine eye showing the thickness of the intraocular lens, and (c) a normal and an opacified cornea.

Usually, the process is supervised by a veterinary doctor, who guarantees that proper procedures are followed.

The freshly enucleated eyes are purchased from the slaughterhouse of Zurich around 7:00 am, and are transported to the laboratory within 30 mins. The suggestion of [Nickerson, 2005] is to place the eyes in isotonic saline solution (9 g NaCl per L H₂O) and keep them in ice. In practice, we found that the saline solution deteriorates the optical elements much faster than if the eyes were in regular tap water. Moreover, we observed that keeping the eyes at low room temperature was sufficient.

The eyes cannot be frozen for later use. This completely destroys not only the optical components, but also the muscles that hold the intraocular lens in position; inserting a needle in previously frozen eyes usually causes the intraocular lens to detach.

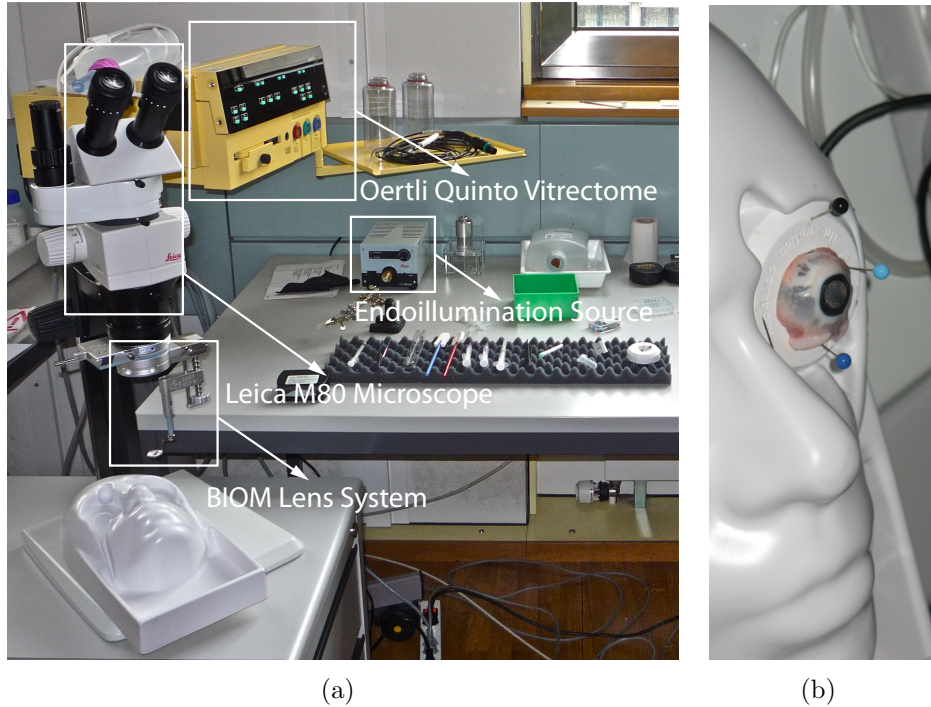


Figure 7.5: (a) Experimental setup to handle cadaver eyes, and (b) model head for cadaver-eye fixation.

We usually have around 3-4 hours to conduct experiments. Outside this time window the cornea and the intraocular lens are too opaque to enable intraocular observation. Moreover, the retinal vessels are drained of their blood, and very little structure can be observed. Figure 7.4(c) shows the effect of time on the transparency of the cornea. To delay this effect, the cornea needs constant moisturizing, which is the reason that the eyes are kept in water.

We have set up a workstation with the necessary surgical tools and observation systems (Fig. 7.5(a)). We can fixate the eyes on a human-head model, as shown in Fig. 7.5(b).

7.2.1 Vitreous Humor Experiments

We are interested in evaluating the motion capabilities of magnetic microdevices in porcine vitreous humor. The obvious approach would be to

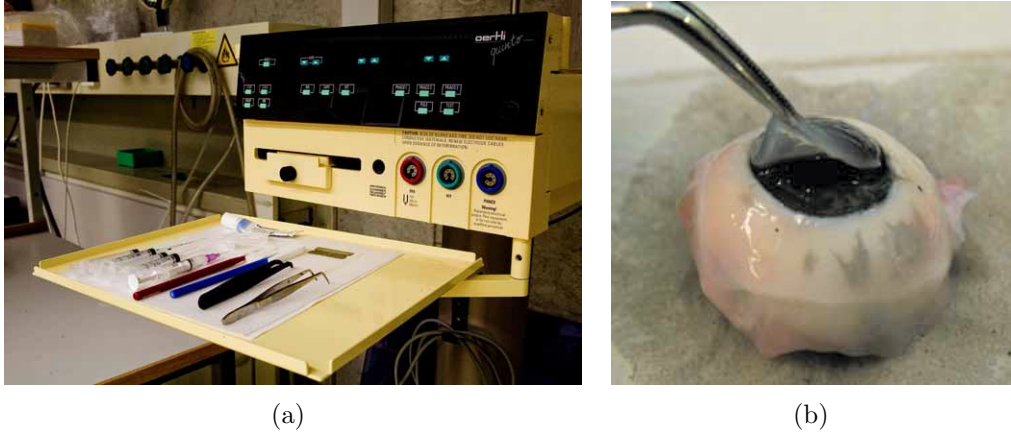


Figure 7.6: (a) Close-up of the surgical tools that we use for the experiments, and (b) removal of the cornea (and subsequently of the intraocular lens) from a cadaver eye.

remove the vitreous humor from the eye, place it in a container, and perform experiments in the container. However, [Nickerson, 2005] points out that the vitreous humor rapidly loses hyaluronic acid and its mechanical properties change upon removal from the eye cavity.

Thus, we need to perform our experiments in the cavity of the porcine eye leaving the vitreous humor intact. As in [Gupta *et al.*, 1999], we remove the cornea and lens of the cadaver eye, in order to expose the anterior chamber and the iris. This is achieved by dissecting the eye at the rim of the cornea above the *pars plana* (Fig. 7.6(b)) using a common cutter. Subsequently, the intraocular lens and the iris can be removed. The aqueous humor leaks out of the eye cavity directly, but the vitreous humor stays intact.

After the removal of the optical elements, we can insert a microrobot in the vitreous humor using a syringe equipped with a glass pipette. Our full set of tools can be seen in Fig. 7.6(a). The pipettes have a diameter of 24 G so that they can fit a 1 mm-long and 500 μm -wide NdFeB cylindrical magnet. After insertion of the microdevice, the eye is positioned under the OctoMag for experimentation.

The imaging system consists of a Leica M80 microscope equipped with an Oculus BIOM 120° lens system for wide-angle observation. This system

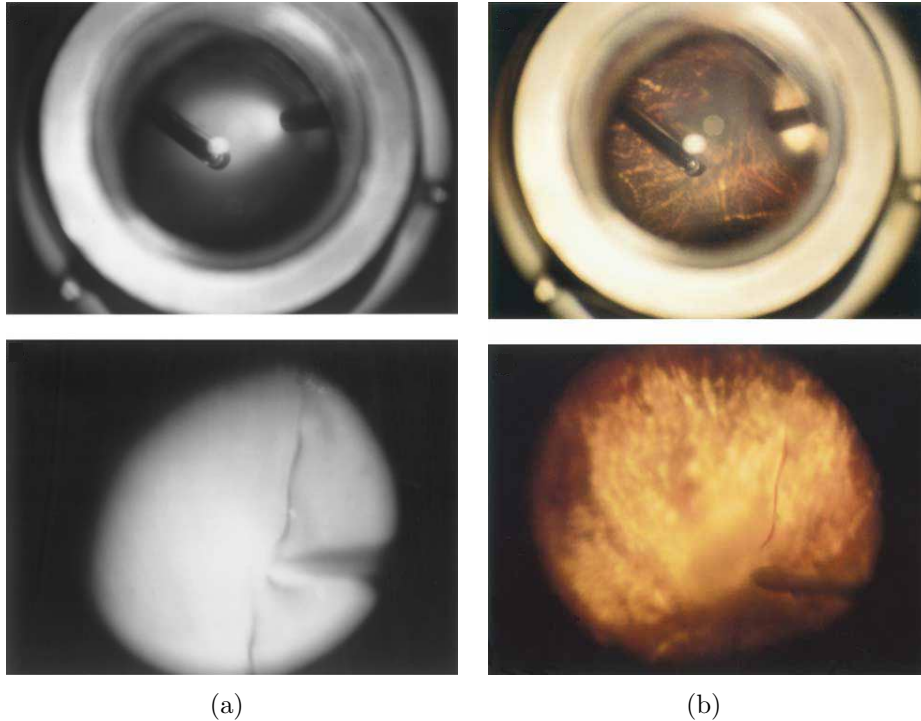


Figure 7.7: (a) Illumination using an optic fiber inserted in the eye cavity, and (b) illumination using an optic fiber shining light transsclerally from the bottom of the eye. Images taken from [Uhlig and Gerding, 2004].

is an indirect ophthalmoscopy system, commercially available. Even though the BIOM (the condensing lens) is not necessary for retinal imaging after the removal of the optical elements, it does provide a wider field-of-view. The images are recorded at 15 fps using a Grasshopper-14S5M/C from Point-Grey.

We use a transscleral illumination method where we direct the light intraocularly through the bottom of the eye's sclera. This approach has been used in [Uhlig and Gerding, 2004], where the authors presented a cadaver-eye holder for training in vitreoretinal surgery. They show that with this type of illumination, images similar to endoillumination with an optic fiber can be achieved (Fig. 7.7). Additionally, transscleral illumination provides more detail on the choroidal structure. Our illumination unit is a Leica CLS100 LED lamp.

Our results vary depending on the quality and age of the received eyes.

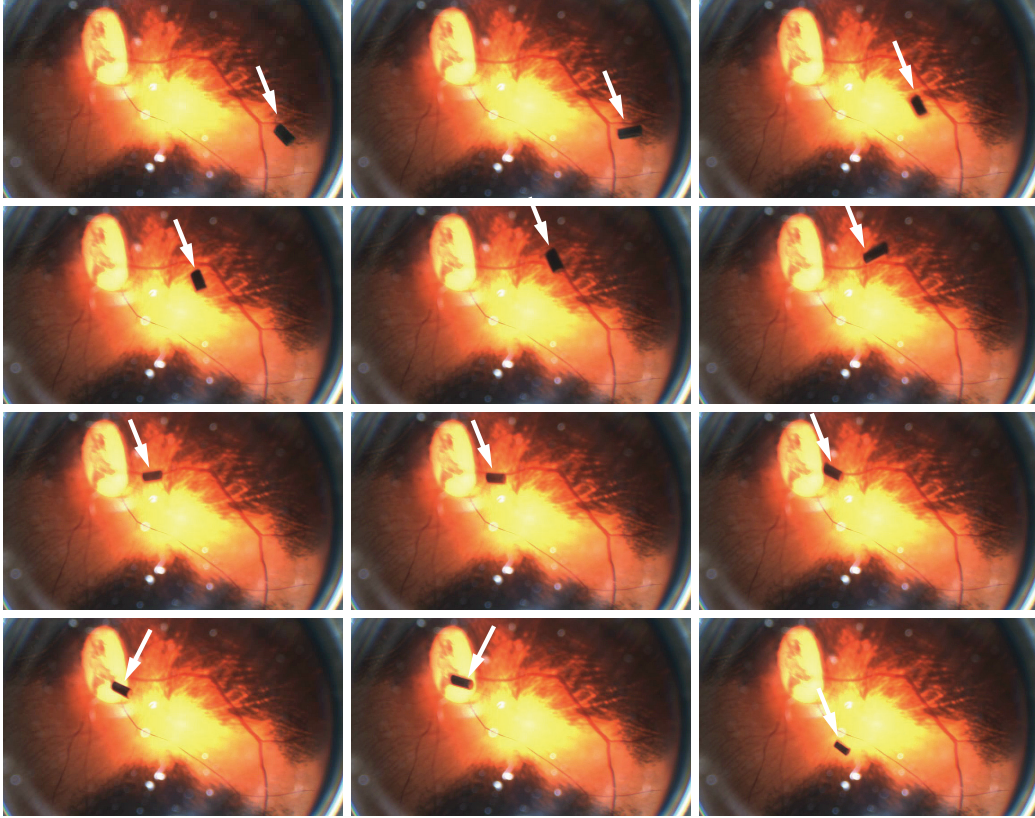


Figure 7.8: Sequence of frames showing a 1 mm NdFeB microrobot moving in the vitreous humor of a cadaver porcine eye.

There have been cases where the microrobots were unable to move and cases where the microrobots were able to move within the area of interest. Results are shown in Fig. 7.8, and Fig. 7.9. The exact age and health status of the eyes is unknown. Based on our knowledge that the vitreous is a thick gel in newborns and liquifies with age, we assume that the microdevices can move in the vitreous humor of older pigs. However, these pigs are meant for consumption, which means that they cannot be of a very old age, unless they have some pathology.

Through personal communication with vitreoretinal surgeons, we learned that the human vitreous of an elderly person compares favorably to the vitreous humor of a pig. This is a good indication that with the appropriate strength of the electromagnetic fields, there will be no need for a vitrectomy.

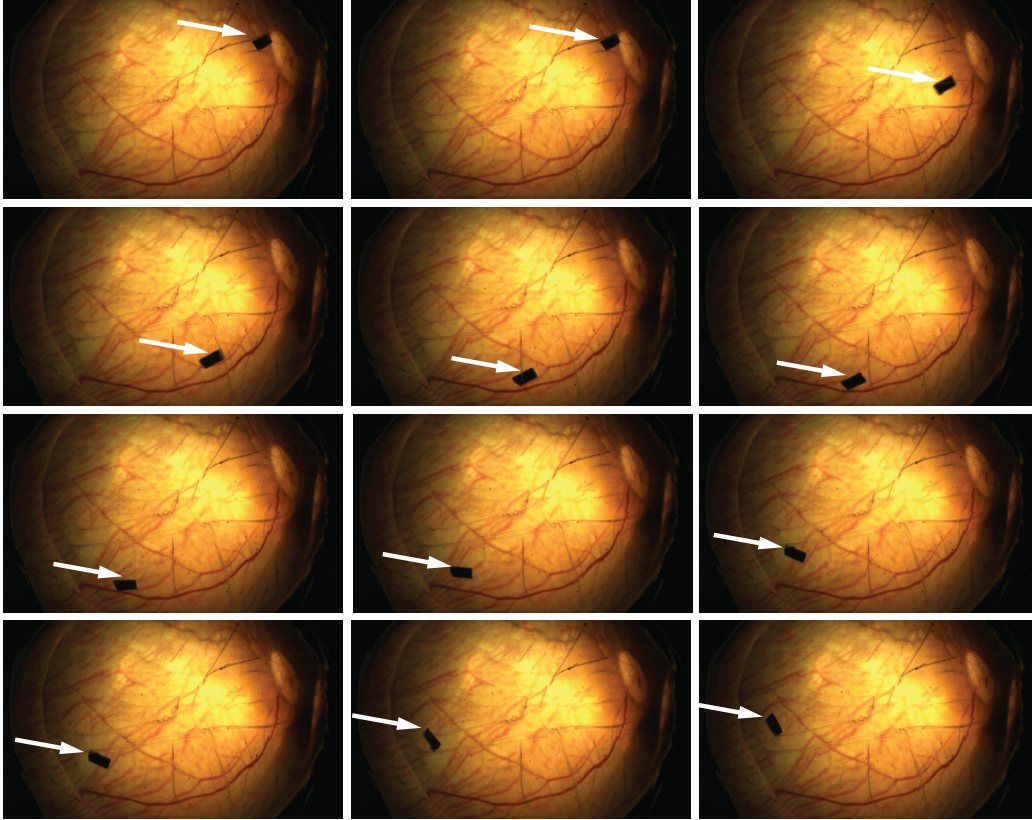


Figure 7.9: Sequence of frames showing a 1 mm NdFeB microrobot moving in the vitreous humor of a cadaver porcine eye.

7.3 Tracking Experiments

While the microrobot moves through the vitreous humor, it exerts small traction forces on the retina. Moreover, transscleral illumination does not require moving an endoilluminator that clutters the perceived images and potentially causes retinal traction. The background in the captured images (i.e. the retina) does not change over time, and the microrobot stands out from the background. This allows the application of a background subtractor for tracking. As with the experiments in the model eye, tracking is performed in a region of interest to achieve the appropriate speed. Examples of tracking a NdFeB device *ex vivo* are shown in Fig. 7.10.

The position of the microrobot can be used for basic control of the device

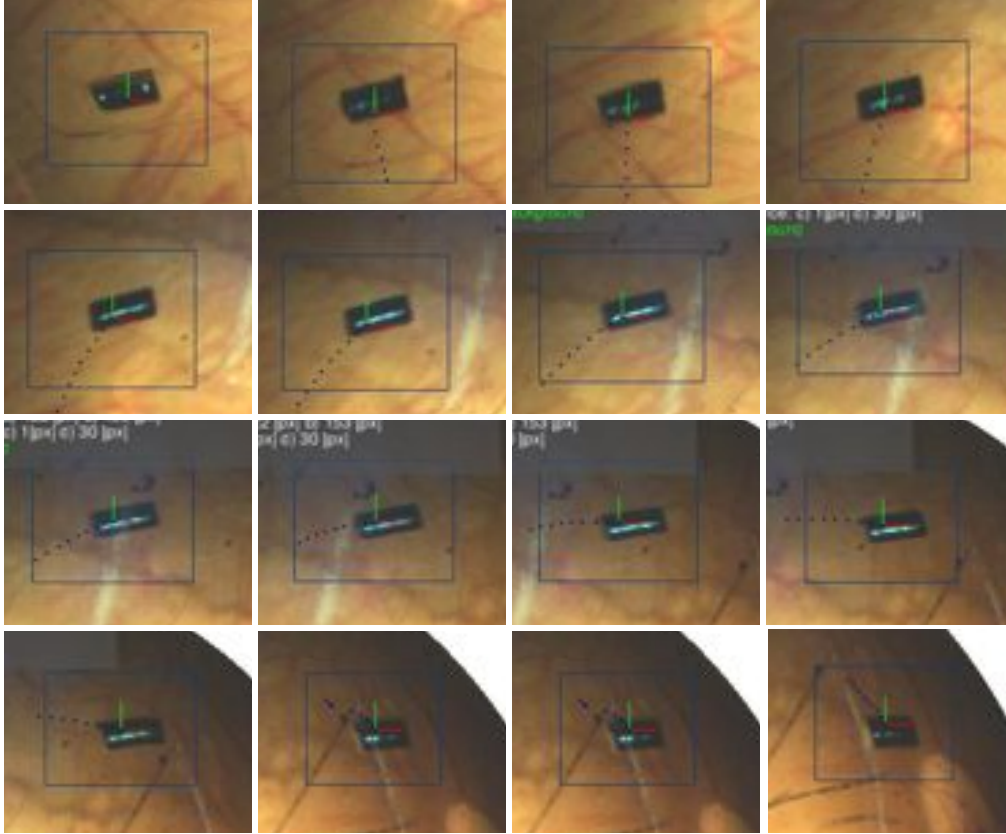


Figure 7.10: Sequence of frames showing a 1 mm NdFeB microrobot tracked in the vitreous humor of a cadaver porcine eye.

in image space. However, the simple PID position controller that is used in the OctoMag is not sufficient for this scenario; the elasticity of the vitreous humor results in high overshoot and oscillation of the microrobot. A velocity controller would be preferable. Additionally, the use of Kalman filters could be considered.

7.4 Protocol for *In Vivo* Experimentation

In experiments that aim to understand the complexities of *in vivo* tests, the optical elements of the porcine eyes are left intact. Moreover, we switch from transscleral illumination to endoillumination. This introduces additional challenges to imaging and handling of the cadaver eyes. Transscleral

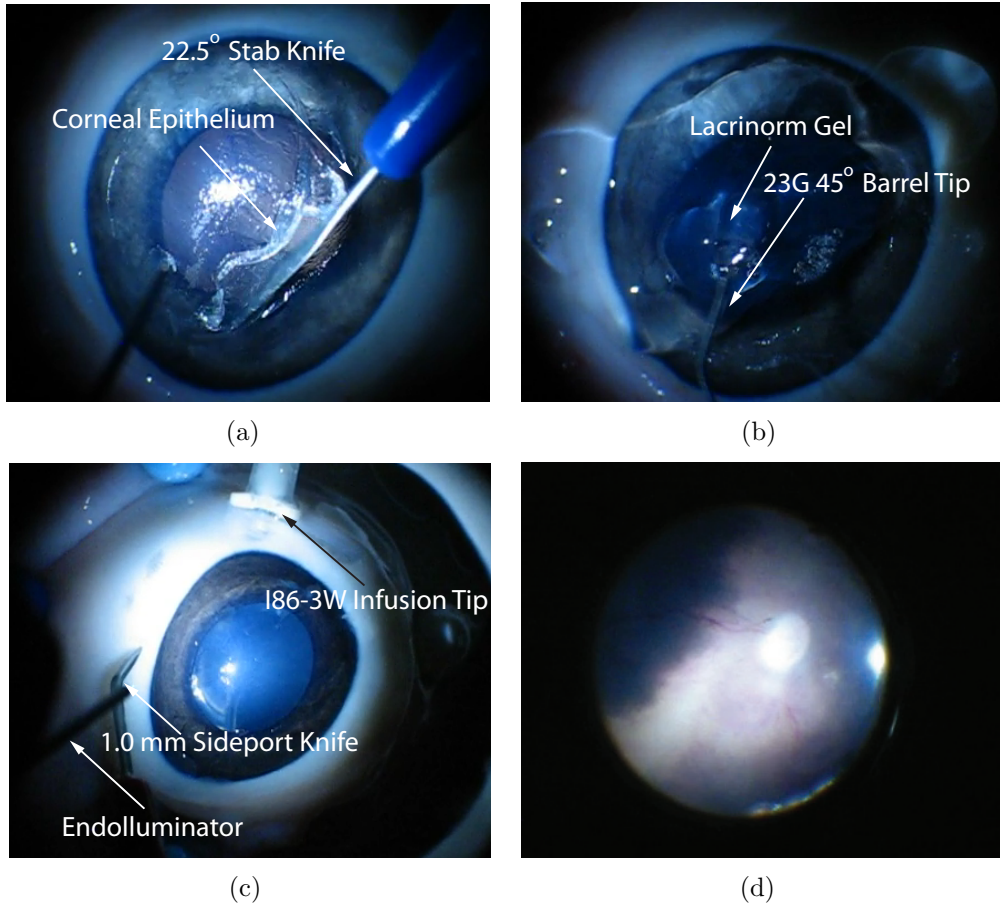


Figure 7.11: (a) Removal of the epithelium membrane of the cornea enables clearer visualization of the retina, (b) the cornea needs constant moisturizing, which is guaranteed by using Lacrinorm gel, (c) all incisions are performed at the *pars plana* region with a 1 mm sideport knife, and (d) the retina of a cadaver eye as observed through the Leica microscope.

illumination can be used in our experimental setup, and there exist methods that can increase the transmittance of light through the sclera. For example, [Bakutkin *et al.*, 1987] mentions a 76% solution of verografin introduced under the conjunctiva of a rabbit results in clarification of the sclera within 1.5 – 2 mins, while it reverts to the original state after 15 – 25 mins. Additionally, [Genina *et al.*, 2006] reports results on using a 40% aqueous glucose solution to achieve similar effects.

The corneal epithelium needs to be removed to improve visualization. The epithelium is a thin layer of cells that covers and protects the cornea. It is removed using a 22.5° stab knife (Fig. 7.11(a)).

Eyes under operation need to be constantly moisturized. Commonly, in the surgical room, Lacrinorm gel is applied on the eye by an assistant at regular intervals. Alternatively, water can be used. The gel, however, is more viscous and tends to stay on the cornea; this makes moisturizing easier. It is applied on the eye using a 45° 23 G barrel tip (Fig. 7.11(b)).

To keep the intraocular pressure constant we use tap water infused in the eye with a I86-3W infusion tip, donated by Oertli Instruments Switzerland (Fig. 7.11(c)).

Light is directed in the eye with a 20 G wide-angle endoilluminator (Oertli Instruments Switzerland). The endoilluminator has a magnetic metallic tip, and care needs to be taken not to approach close to the microrobot. We perform an incision at the *pars plana* region of the porcine eye to insert the endoilluminator. This and all incisions are performed with a 1 mm sideport knife from Medilas AG.

The retina of the eye is observed using a Leica microscope and a BIOM lens. The focusing procedure is easy but not intuitive. First, without the indirect ophthalmoscopy lens (the BIOM), we need to focus on the iris of the eye. Afterwards, the BIOM lens is introduced, and we move the condensing lens until the retina comes in focus. Finally, changing the working distance of the microscope results in increasing or decreasing the field-of-view, but does not affect focusing. The magnification of the retina depends on the condensing lens used; in our case, we observe a high field-of-view with limited magnification (Fig. A.5(b)). Figure 7.12 was taken during our experimentation with cadaver eyes.

Finally, we need to determine if a vitrectomy must be performed. We carried out experiments with 2 mm-long CoNi microrobots that require a vitrectomy. To insert the vitrectome, a 1 mm incision is required. We performed vitrectomies using the Klöti vitrectome, by Oertli Instruments Switzerland. Oertli trained us in vitrectomies at their facilities. In order to mark the dead vitreous for removal, we use a 0.05% Trypan blue solution. Trypan

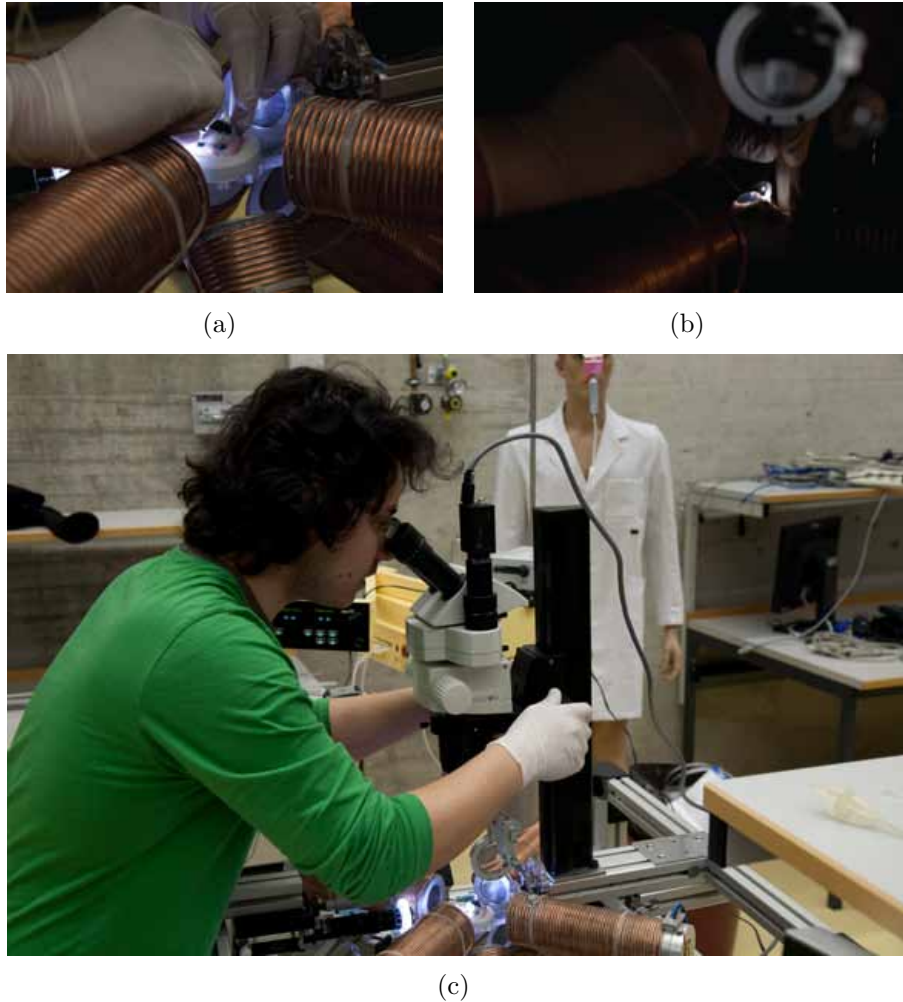


Figure 7.12: Pictures of the *ex vivo* experimental process: (a) The cadaver eye is fixated under the Leica microscope, in the workspace of the OctoMag, (b) using the endoilluminator for external illumination, we focus the microscope on the iris of the eye, and (c) our experimental setup.

blue cannot be used in a real surgery due to its toxicity. Alternatively, crystalline cortisone suspension can be used. Figure 7.13(a) shows a 2 mm-long CoNi microrobot near a retina vein. This image was taken using a S5.7030u disposable vitrectomy lens from FCI Ophthalmics, and an Olympus 10 MP camera.

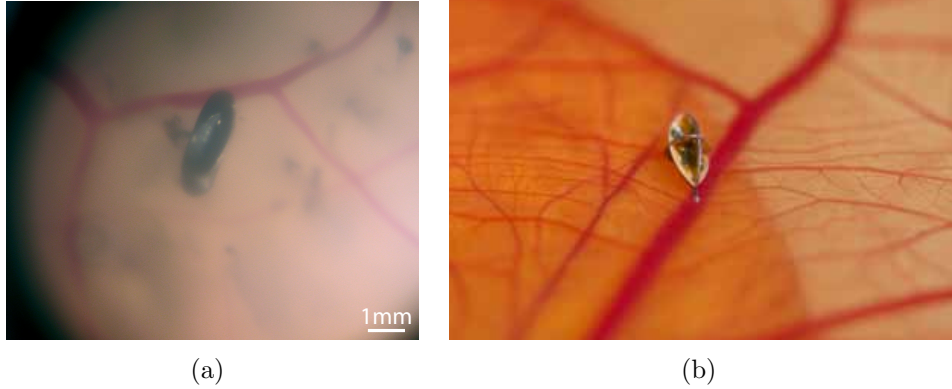


Figure 7.13: (a) A 2 mm-long CoNi microrobot close to a retinal vein. Visualization achieved with a disposable vitrectomy lens. (b) A 1 mm-long microrobot docked on a CAM vein. Both images have been recorded with a 10 MP Olympus camera.

7.5 Conclusions

The work in this chapter was a necessary feasibility study for performing intraocular surgery with microrobots. More specifically, we examined the potential of magnetic agents moving in the posterior of the human-eye cavity by gradient forces (i.e. pulling and pushing). Our results from *in vitro* experiments with simulated vitreous humor show that soft-magnetic bodies will be unable to move without a vitrectomy. Permanent magnetic microrobots, on the other hand, are likely not to require a vitrectomy, especially given that the vitreous humor of the human eye liquifies with age. We supported these conclusions with *ex vivo* experiments on cadaver porcine eyes. Moreover, we developed a protocol for fully handling cadaver eyes. This protocol can be directly applied for additional *ex vivo* experiments, and later, for *in vivo* experiments.

Chapter 8

Color/Shape-Based Tracking of Microdevices

Successful ophthalmic surgeries using intraocular untethered microrobots or tethered robotic microtools require methods to robustly track the microdevices in the posterior of the human eye. The dimensions and specularities of the microdevices are major obstacles for accurate tracking. Keeping intraocular objects constantly in focus is challenging, and the captured images are often blurry and noisy. The unstructured illumination that reaches the interior of the eye, either through transpupillary or transscleral means, can deteriorate the images with uneven brightness and backreflections. Due to the noisy nature of the images edge-based algorithms do not operate well.

If the tracked device has a color similar to background structures, or the background changes, then background subtraction techniques cannot be used. In this chapter, we examine a method to evaluate different colorspace for microdevice tracking. After selection of the appropriate colorspace, thresholds that ensure maximum separation of the device from the background are calculated. Based on trained color histograms, level sets are used to track in real time. Additionally, we demonstrate a way to incorporate statistical shape information in the existing tracking framework.

We demonstrate the developed algorithm by tracking microdevices during microhandling and microrobots in human-eye models.

8.1 Colorspace Selection

The utilization of different colorspace for image segmentation and visual tracking can significantly enhance algorithmic performance. Each colorspace provides a different representation of color information, and as a result, some

are more appropriate for specific applications. In [Stern and Efros, 2005] the authors propose a method to choose the best colorspace on-line, and in [Moreno-Noguer *et al.*, 2006] the authors create (off-line) a colorspace tailored for specific object tracking. In the field of minimally invasive surgery, [Doignon *et al.*, 2005] proposes using the Hue and Saturation channels of the HSV colorspace to track surgical instruments in the abdominal cavity. In [Ascari *et al.*, 2004] image binarization and Hue/Saturation channels are used in order to segment the lumen, nerves and endoscope in the spinal coord, and in [Tjoa *et al.*, 2001], Hue and Homogeneity are used to segment endoscopic images. We are mainly interested in tracking microtools in the posterior of the human eye. We proposed colorspace selection as a preprocessing step based on training data.

8.1.1 Colorspace Evaluation

The object of interest Ω_{o_j} is manually segmented from $j = 1 \dots k$ images. The complement of this region, Ω_{b_j} , corresponds to the background in the images. Using the segmented regions, the object's and background's joint-histograms for the channels/colorspace of interest are calculated, resulting in the probabilities $P(\mathbf{u} \mid \mathbf{x} \in \Omega_o)$, and $P(\mathbf{u} \mid \mathbf{x} \in \Omega_b)$, where \mathbf{x} is the pixel of interest, Ω_o is the object region, Ω_b is the background region, and $\mathbf{u}(\mathbf{x}) \in \mathbb{R}^n$ is the observed intensity values vector for the n channels of interest. We define an extended region $\Omega_{e_j} = \Omega_{o_j} \oplus \omega$ where ω is the structural element of preference, such that $\Omega_{o_j} \subset \Omega_{e_j}$. The set $\Omega_{n_j} = \Omega_{e_j} \setminus \Omega_{o_j}$ corresponds to the background in the object neighborhood in image j .

The simplest object-from-background separation criterion is a decision function $F(\mathbf{u}(\mathbf{x})) : \mathbb{R}^n \rightarrow \mathbb{R}$, where the pixel \mathbf{x} is classified as belonging to the object ($F > 0$) or as belonging to the background ($F < 0$). The value of this function is based on the previously calculated probabilities.

The desired colorspace is the one that minimizes the misclassifications of background pixels as object pixels, while maximizing the correct classifications. We consider as object pixels the region Ω_{o_j} in each image. The

colorspace quality for each image j is calculated by:

$$r_j = c_o + c_n - m_o - m_n \quad (8.1)$$

where c_o is the ratio of correct object classifications to object size (in pixels), c_n is the ratio of correct neighborhood classifications to neighborhood size, and m_o, m_n the respective misclassification ratios. By comparing the mean and variance of r for different colorspace, the most appropriate colorspace can be selected.

8.1.2 Maximum Separability Thresholding

The classification of a pixel as belonging to the object or the background depends on the value of the decision function F . Instead of using a binary criterion for the classification, we estimate decision thresholds above which a pixel is treated as part of the object, and below which a pixel is considered as part of the background. For values between the two thresholds, no direct decision should be made. However, a decision can be made based on the neighbors, similar to hysteresis thresholding. The thresholds are estimated by minimizing, for each segmented image and colorspace, the objective function:

$$r_j(t_l, t_h) = (c_o - 1)^2 + (c_n - 1)^2 + m_o^2 + m_n^2 \quad (8.2)$$

where t_l and t_h are the lower and higher thresholds, respectively. Minimizing this function for each image for different colorspace ensures the maximum correct classifications and the minimum misclassifications. The thresholds for each colorspace are finally averaged and can be used for more accurate pixel classification together with the appropriate colorspace representation. Depending on the significance of each term of (8.2), weights can be added.

8.2 Level-Set Tracking using Statistical Information

The most common approaches in tracking use active contours, evolving either as parameterized snakes [Kass *et al.*, 1988], or as higher-order level-set functions [Osher and Fedkiw, 1987]. The first approach is computa-

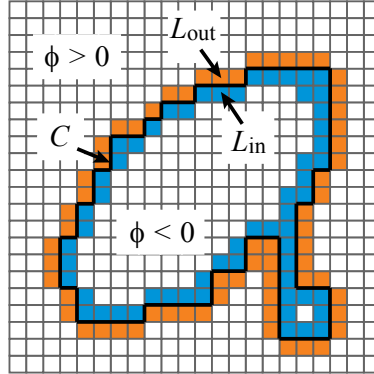


Figure 8.1: The sets of pixels where the level-set function ϕ is updated. C is the propagating front. This level-set function can represent a tracked microrobot and an erroneously segmented part of the background.

tionally efficient, but needs explicit methods to handle re-parameterization and topology changes. The second approach is independent of topology and parametrization, but is computationally more complex. Recently, a real-time tracking algorithm based on level sets has been proposed [Shi and Karl, 2005], and thus, the computational complexity of tracking using level sets can be overcome.

8.2.1 Real-Time Tracking Using Level Sets

The efficacy of the algorithm in [Shi and Karl, 2005] lies in the idea that instead of updating the full level-set function, one can update pixels near the propagating front, similarly to the narrow band algorithm presented in [Osher and Fedkiw, 1987], or the HERMES algorithm presented in [Paragios and Deriche, 2000]. The algorithm [Shi and Karl, 2005] also avoids the computational overhead of solving the curve evolution PDE. The propagating-front pixels belong to two sets (see Fig. 8.1):

$$\begin{aligned}
 L_{\text{out}} &= \{\mathbf{x} \mid \phi(\mathbf{x}) > 0, \exists \mathbf{y} \in N_4(\mathbf{x}) \text{ such that } \phi(\mathbf{y}) < 0\}, \\
 L_{\text{in}} &= \{\mathbf{x} \mid \phi(\mathbf{x}) < 0, \exists \mathbf{y} \in N_4(\mathbf{x}) \text{ such that } \phi(\mathbf{y}) > 0\}
 \end{aligned}$$

where $N_4(\mathbf{x})$ are the 4-connectivity neighbors of \mathbf{x} , and ϕ is a level-set function:

$$\phi(\mathbf{x}) = \begin{cases} +3 & \text{if } \mathbf{x} \text{ is an exterior pixel,} \\ +1 & \text{if } \mathbf{x} \in L_{\text{out}}, \\ -1 & \text{if } \mathbf{x} \in L_{\text{in}}, \\ -3 & \text{if } \mathbf{x} \text{ is an interior pixel.} \end{cases}$$

Two procedures *switch_in()* and *switch_out()* are defined:

- *switch_in*(\mathbf{x}) switches the pixel $\mathbf{x} \in L_{\text{out}}$ to L_{in} , and adds its 4-neighboring exterior pixels to L_{out} .
- *switch_out*(\mathbf{x}) switches the pixel $\mathbf{x} \in L_{\text{in}}$ to L_{out} , and adds its 4-neighboring interior pixels to L_{in} .

The evolution of the sets is carried out in two cycles:

- Cycle One: The decision whether a pixel \mathbf{x} from L_{in} and L_{out} should be switched depends on function F . A decision function can be $F = \log \left(\frac{P(\mathbf{u}(\mathbf{x})|\Omega_o)}{P(\mathbf{u}(\mathbf{x})|\Omega_b)} \right)$, where $\mathbf{u}(\mathbf{x})$ is the feature vector defined at pixel \mathbf{x} , Ω_o is the object of interest, and Ω_b is the background. The probabilities are calculated based on the joint-probability histograms that are determined in the training phase, and the features used correspond to the channels of the colorspace that exhibited the maximum quality in Sec. 8.1.1. A pixel \mathbf{x} belonging to L_{out} is passed to *switch_in* if $F(\mathbf{x}) > t_h$, and a pixel \mathbf{x} belonging to L_{in} is passed to *switch_out* if $F(\mathbf{x}) < t_l$. The thresholds t_l and t_h are calculated in the preprocessing step of Sec. 8.1.2. This is a deviation from the original algorithm of [Shi and Karl, 2005], and increases the tracking robustness.
- Cycle Two: The switches occur depending on smoothness restrictions. Instead of smoothing the whole level-set function, only the values at L_{out} and L_{in} are smoothed (see [Shi and Karl, 2005] for details).

The presented tracking algorithm makes use of statistical color information based on training images, but does not use information about the shapes of

the objects of interest. We further increase the tracking robustness by adding a third evolution cycle so that the evolving curve resembles a known shape. In this way, desired objects can be segmented from noisy environments using both color and shape information.

8.2.2 Creating a Statistical Shape Model

Algorithms that use known shape information (shape prior) consist of three stages. At the first stage, a training set is created from representations of the desired object. These object representations can be the ones that are used in order to create the joint-probability histogram required for tracking. In order for the images to be used for the shape prior extraction, they should be registered. We register the level-set surfaces corresponding to the binary images of the segmented objects [Rousson and Paragios, 2002], using the method presented in [Guizar-Sicairos *et al.*, 2008] for the 2D translation registration, followed by scale and rotation registration.

The second stage consists of creating a model of the desired object. In [Leventon *et al.*, 2000], the singular value decomposition of a matrix consisting of the vectorized registered level-set functions results in the extraction of eigenshapes. A linear combination of eigenshapes creates a shape prior with the desired precision:

$$\bar{\phi}(\mathbf{a}, \mathbf{p}) = \mu(\mathbf{p}) + \sum_{i=1}^k a_i v_i(\mathbf{p}) \quad (8.3)$$

where $\bar{\phi}$ is the shape prior, μ is the mean level-set function, \mathbf{p} is a vector containing pose parameters, v_i are the k extracted eigenshapes, and $\mathbf{a} = \{a_1, \dots, a_k\}$ are the weights of the eigenshapes. This representation of the shape prior enables it to be used in a statistical fashion, and in accordance with the level-set tracking algorithm of Sec. 8.2.1.

The third stage consists of estimating the most probable shape prior (i.e. estimate its eigenweights \mathbf{a} and pose parameters \mathbf{p}) based on the current evolving level-set function. In [Leventon *et al.*, 2000], this problem is formulated as an *a posteriori* probability maximization problem. We reformulate

this approach in order to make it fit the probabilistic evolution of the presented tracking algorithm.

The best estimates for the shape eigenweights \mathbf{a} , and pose parameters \mathbf{p} are given as:

$$\langle \mathbf{a}^*, \mathbf{p}^* \rangle = \arg \max_{\mathbf{a}, \mathbf{p}} P(\mathbf{a}, \mathbf{p} \mid \phi, I) \quad (8.4)$$

where ϕ is the current level-set function, and I represents image information (e.g. gradient, histogram). Based on Bayes' rule, the previous equation can be rewritten as:

$$P(\mathbf{a}, \mathbf{p} \mid \phi, I) = \frac{P(\phi \mid \mathbf{a}, \mathbf{p})P(I \mid \mathbf{a}, \mathbf{p}, \phi)P(\mathbf{a})P(\mathbf{p})}{P(\phi, I)} \quad (8.5)$$

where for simplification it is assumed that pose and shape are independent (no projective distortion), and thus, $P(\mathbf{a})$ and $P(\mathbf{p})$ can be calculated separately.

Term $P(\phi \mid \mathbf{a}, \mathbf{p})$ is the probability that a given level-set function ϕ is observed based on shape-prior parameters \mathbf{a} and \mathbf{p} (the estimated shape prior is $\bar{\phi}(\mathbf{a}^*, \mathbf{p}^*) = \phi^*$). Contrary to [Leventon *et al.*, 2000], since the shape prior will be used for tracking, we cannot assume that the evolving zero level set of ϕ lies inside the estimated zero level set of ϕ^* . The term can be equal to the Laplacian of the difference between the current level-set function, and the estimated shape prior:

$$P(\phi \mid \mathbf{a}, \mathbf{p}) = \exp(- \|\phi - \phi^*\|) \quad (8.6)$$

which takes its maximum value when ϕ and ϕ^* are identical.

Term $P(I \mid \mathbf{a}, \mathbf{p}, \phi)$ is the probability of observing certain image features given the current and estimated level-set functions. In [Leventon *et al.*, 2000], the observed feature in the image is the gradient, whereas here, the features are the intensity values of the channels of the chosen colorspace. The interior of the estimated shape prior ϕ^* should have a color histogram that is similar to the one of the evolving level-set function ϕ . As a result, the value of this

term can be the Laplacian of this similarity:

$$P(I \mid \mathbf{a}, \mathbf{p}) = \exp(- \| h - h^* \|) \quad (8.7)$$

where h and h^* are the joint-probability histograms for the objects segmented by ϕ and ϕ^* respectively.

For the terms $P(\mathbf{a})$ and $P(\mathbf{p})$ in (8.5), we use [Leventon *et al.*, 2000]:

$$P(\mathbf{a}) = \frac{1}{\sqrt{(2\pi)^k |\Sigma_k|}} \exp\left(-\frac{1}{2} \mathbf{a}^T \Sigma_k^{-1} \mathbf{a}\right) \quad (8.8)$$

$$P(\mathbf{p}) = U(-\infty, \infty) \quad (8.9)$$

where Σ_k is a $k \times k$ diagonal matrix containing the eigenvalues corresponding to the extracted eigenshapes, and U denotes the uniform distribution.

The denominator term of (8.5) has no dependency on shape or pose, and can be disregarded from the probability maximization.

8.2.3 Evolution Using Statistical Shape Information

The estimated shape prior ϕ^* is used as an evolutionary force acting on the propagating front. The estimation can be done using the sets L_{in} and L_{out} to speed up the minimization process. In the framework of the algorithm of Sec. 8.2.1, pixels belonging to the background (object) should be subjected to a negative (positive) force. The predicted shape prior ϕ^* is a level-set function, and, as such, if C is its zero-level curve, it is negative in the interior of C and positive in its exterior. Based on this, a third cycle can be introduced in the level-set tracking algorithm:

- Cycle Three: Pixels \mathbf{x} belonging to L_{out} are passed to *switch_in* if they are inside the estimated shape prior ϕ^* , and pixels \mathbf{x} belonging to L_{in} are passed to *switch_out* if they are outside the estimated shape prior.

Cycle three iterates until convergence or until a maximum number of iterations is reached. Convergence is achieved when the evolving level-set function ϕ coincides with the estimated shape prior ϕ^* . This might not be desirable if

- Compute the shape prior with the maximum *a posteriori* probability ϕ^* , based on (8.5) and the current level-set function ϕ .
 - For $i = 1:N_s$ do
 - $\forall \mathbf{x} \in L_{\text{out}}$, if $\phi^*(\mathbf{x}) < 0$, then *switch_in*(\mathbf{x}).
 - $\forall \mathbf{x} \in L_{\text{in}}$, if $\forall \mathbf{y} \in N_4(\mathbf{x}), \phi(\mathbf{y}) < 0$, delete \mathbf{x} from L_{in} , and set $\phi(\mathbf{x}) = -3$.
 - $\forall \mathbf{x} \in L_{\text{in}}$, if $\phi^*(\mathbf{x}) > 0$, then *switch_out*(\mathbf{x}).
 - $\forall \mathbf{x} \in L_{\text{out}}$, if $\forall \mathbf{y} \in N_4(\mathbf{x}), \phi(\mathbf{y}) > 0$, delete \mathbf{x} from L_{out} , and set $\phi(\mathbf{x}) = +3$.
-

Table 8.1: Cycle Three of the Level Set Tracking Algorithm

ϕ should capture object variability as well. Thus, selecting the appropriate number of iterations requires some experimentation. The exact structure of the third cycle of the algorithm can be seen in Table 8.1.

8.3 Experiments

We implemented our algorithm in Matlab and in C++ for experimental validation and on-line tracking. We conducted several experiments with microrobots during micromanipulation and microrobots moving in human-eye models.

8.3.1 Tracking Microrobots during Micromanipulation

In the first experiment, we demonstrate how the algorithm can track a microrobot while it pushes disks on a surface. The microrobot is a MagMite [Vollmers *et al.*, 2008; Frutiger *et al.*, 2010], and this manipulation task is one of the challenges at the Nanogram League of Robocup [Robocup, 2009]. Tracking can be done at 30 – 60 fps, depending on the zoom level. Higher zoom levels require a larger propagating front for the microdevice, and this leads to a drop in the frame rate. The microdevice and three disks can be successfully tracked at 15 fps. The imaging system is a Basler A602f camera equipped with a zoom lens.

We can perform tracking using grayscale information, and ignore shape. The histograms are trained by manually segmenting the different objects in a sequence of images. Afterwards, detection and tracking can be done automatically. Based on the trained histograms and the decision function, the algorithm assigns a probability to all pixels in the image; the pixels can belong to either the object or the background. Then, based on the calculated thresholds the probability map is binarized, and the object of interest is extracted based on additional heuristic criteria (e.g. size, eccentricity, proximity to center). Different objects can be distinguished based on their color (Fig. 8.2).

Objects of the same color can be distinguished as well. Consider the case where the microdevice has the same color information as the manipulated disks. We can train and initialize one tracker for detecting the microrobot and one for all three disks. In the first image, all objects are successfully detected. Afterwards, the tracker that handles the microrobot receives images where the detected disks are masked out. The tracker that detects the disks receives images where the microrobot is masked. The object's position in the previous frames and additional morphological filtering leads to separation of the objects even if they are in contact (Fig. 8.3). This is not achievable with simple background subtraction techniques, since all the manipulated objects move.

8.3.2 Tracking in Silicone Oil Using Shape Information

In the second experiment, we track a microrobot of the type presented in [Yeşin *et al.*, 2006] in silicone oil, but we add an artificial occlusion in the images. With shape information the microrobot is tracked successfully despite the occlusion (see Fig. 8.4). The imaging system is a Basler A602fc camera with a Fujinon HF9HA-1B lens.

8.3.3 Tracking in a Model Eye Using Color Information

In the third experiment, we place the biomedical microrobot in a model eye [Gwb International, Ltd., 2010] that is commonly used for training by

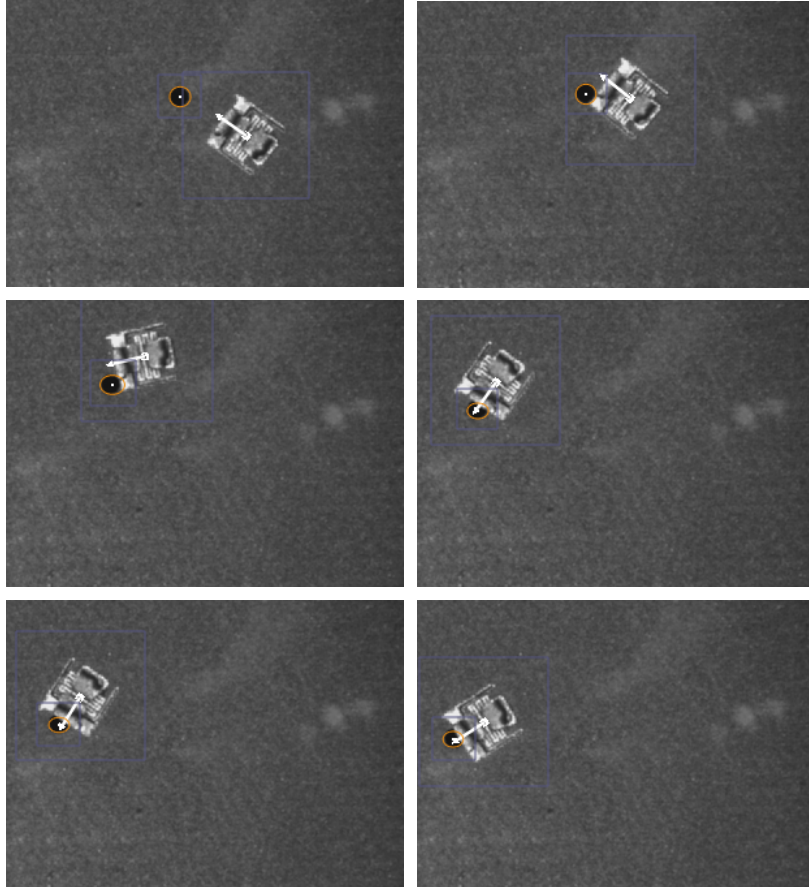


Figure 8.2: Pushing disks using a MagMite. The disk and the MagMite are distinguished through their different color histograms. The arrow on the microrobot indicates that the device is tracked and shows its orientation. Similarly, the orange circle and the white dot denote the position of the disk.

ophthalmologists. The eye is filled with silicone oil.

Imaging microdevices in the posterior of an eye has been discussed in previous chapters. Depending on the application, specific ophthalmic lenses must be considered. Here, we require a compromise between high field-of-view and high magnification. We use the Digital High Mag[®] lens [Volk, 2008] from Volk Optical Inc., which enables a field-of-view of $\sim 60^\circ$, and a magnification of $1.30\times$. This lens is designed for retinal imaging. Capturing the images with a camera ensures a larger depth-of-field (see Fig. 8.5).

8 COLOR/SHAPE-BASED TRACKING OF MICRODEVICES



Figure 8.3: Pushing disks using a MagMite. The disk and the MagMite have the same color information but can be distinguished even when they are joined using prior information on each object's position. The arrow on the microrobot indicates its orientation. Similarly, the orange circle and the white dot denote the position of the disk. The squares show the region of interest where the tracker is updated for each object.

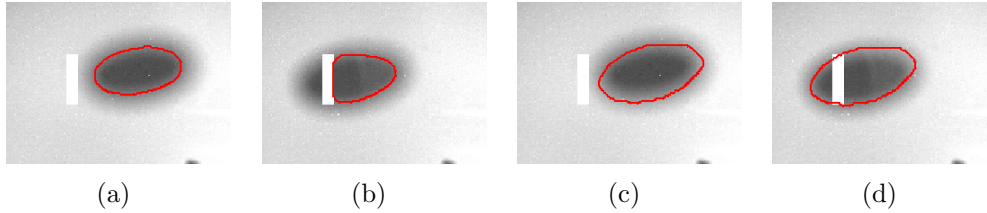


Figure 8.4: Microrobot moving from right to left in silicone oil with an artificial occlusion. In (a), (b) the tracking fails, but in (c), (d) the statistical shape information results in successful tracking.

For illumination inside the model eye we constructed an apparatus based on transscleral illumination principles consisting of multiple LEDs arranged in a circle around the model eye sclera. Transscleral illumination is non-invasive and limits backreflections from the lens surfaces.

We evaluate the quality of every two-channel combination for basic colorspace (see Table 8.2). Using all channels of a colorspace will lead to a large overhead, and we want to examine the efficacy of the tracker with limited information. In Fig. 8.6(a), and Fig. 8.6(b), the quality of the channels for the RGB and HSV colorspace can be seen, respectively. For the RGB colorspace, the highest quality is exhibited by the R-G channel combination. The combination of the H-S channels for the HSV colorspace leads to worse object-from-background separation, even though the H-S channels have been shown to be suitable for tracking tools and endoscopes in the human body [Doignon *et al.*, 2005; Ascari *et al.*, 2004; Tjoa *et al.*, 2001]. This indicates that different biomedical applications might benefit from the use of specific channels/colorspaces, and thus, their selection is an important preprocessing step.

In Table 8.2, we show the quality mean and variance for channel combinations of typical colorspace. The channels R-G of the RGB colorspace are the most suitable for tracking, since they have the highest mean quality and the lowest quality variance. Another good selection is the channels Y-V of the YUV colorspace. We also perform an experiment using the H-S channels of the HSV colorspace, since this selection is appropriate for other biomed-

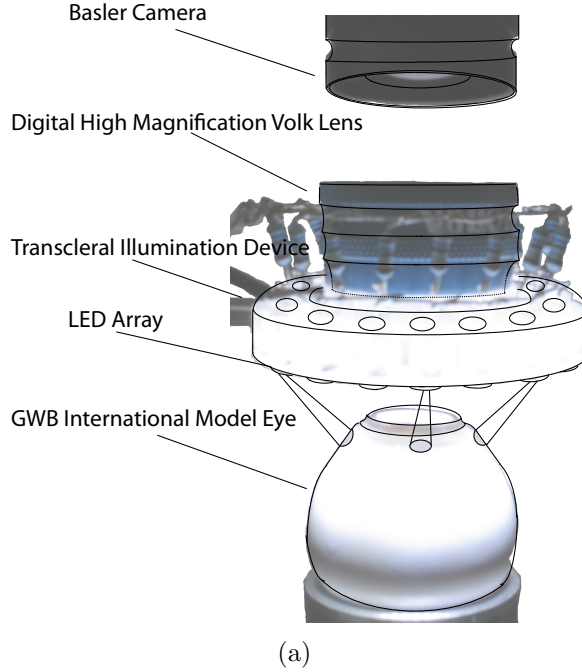


Figure 8.5: The experimental imaging setup of Sec. 8.3.3.

cal applications. Figure 8.7(a) shows tracking results for the R-G channels, and Fig. 8.7(c) shows the results for the Y-V channels; using the best channels/colorspace leads to reduced vein segmentation. Tracking in H-S leads to very poor results (see Fig. 8.7(e)).

Next, we impose calculated thresholds to the R-G ($t_l = -0.17, t_h = 1.71$), the Y-V ($t_l = -0.11, t_h = 1.69$), and the H-S ($t_l = -0.77, t_h = 0.77$) tracking cases. Successful tracking occurs at around 25 fps in our Matlab implementation, and typical frames can be seen in Fig. 8.7(b), Fig. 8.7(d), and Fig. 8.7(f), respectively. It can be seen that in the R-G, and Y-V cases (i.e. when the chosen channels/colorspace exhibits high quality) thresholding increases the tracking robustness. In the H-S case, the thresholds result in the tracker losing the microrobot.

To accurately estimate the accuracy achieved, we establish ground truth values by manually segmenting the microrobot in 40 equally spaced frames. The microrobot's contour is an ellipse, and the relative errors are calculated

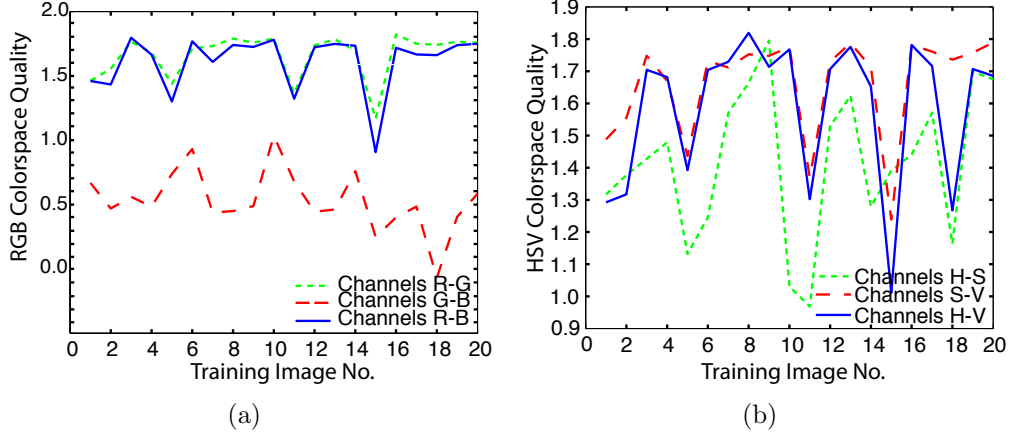


Figure 8.6: Quality measure for the (a) RGB colorspace, and (b) HSV colorspace. The lowest points in the graphs correspond to images where the microrobot is occluding or in the vicinity of a retinal vein.

	1 – 2	2 – 3	1 – 3
RGB	1.66 ± 0.03	0.53 ± 0.06	1.61 ± 0.05
YUV	1.52 ± 0.08	1.63 ± 0.05	1.64 ± 0.04
YIQ	1.63 ± 0.04	1.63 ± 0.03	1.56 ± 0.03
HSV	1.41 ± 0.06	1.66 ± 0.07	1.58 ± 0.06
XYZ	1.59 ± 0.06	1.50 ± 0.07	1.59 ± 0.06
nRGB	1.49 ± 0.05	1.47 ± 0.05	1.49 ± 0.05

Table 8.2: Colorspace mean quality and standard deviation for different channel combinations

with respect to the ellipse’s center (X_c, Y_c) , the major (A) and minor (B) axis, and the orientation angle (ϕ) . Moreover, in order to quantify the importance that thresholding has on a non-optimal colorspace, we track the microrobot using the Y-U channels of the YUV colorspace ($t_l = -0.13, t_h = 1.64$). The errors can be seen in Table 8.3, and show that even though thresholding has a great impact on proper tracking, carefully selecting both the colorspace and the thresholds leads to the best results.

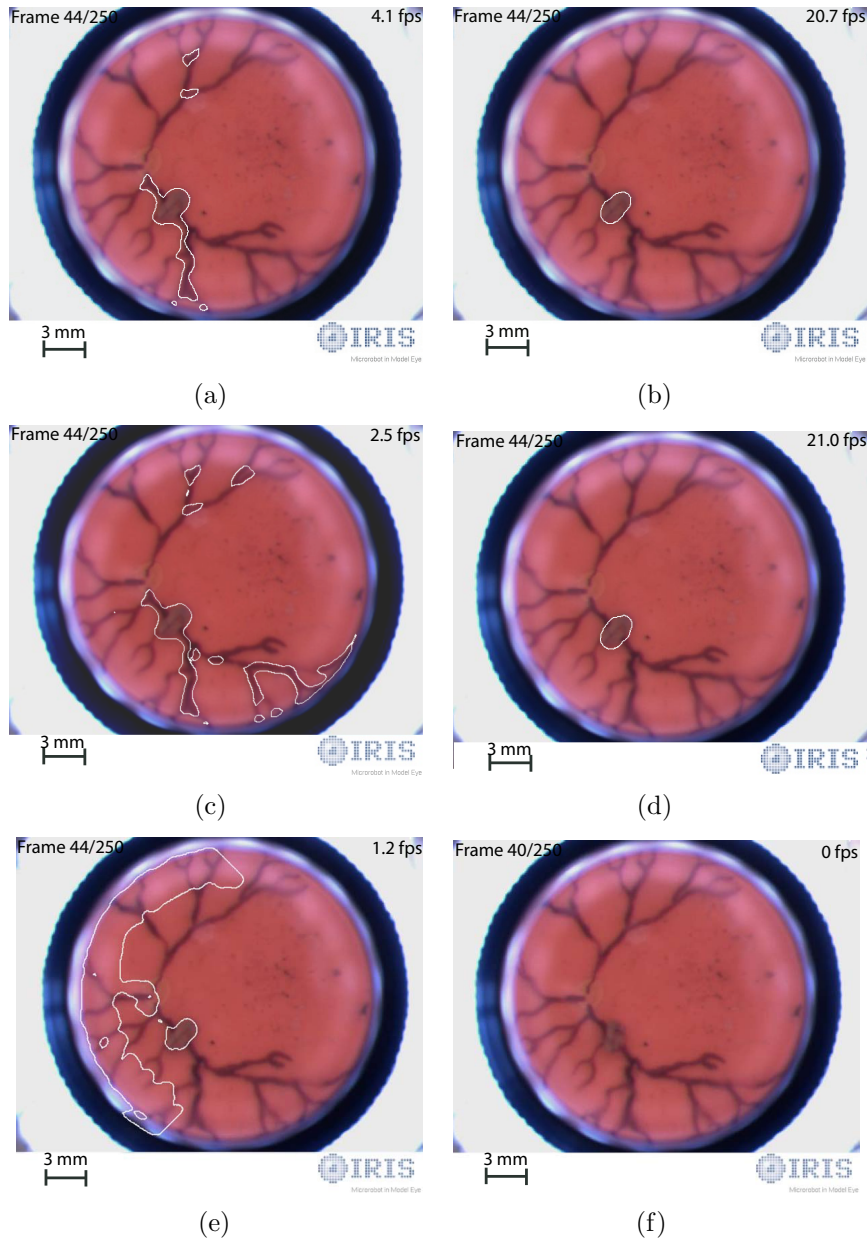


Figure 8.7: Tracking using (a), (b) the R-G channels of the RGB colorspace without and with thresholds, respectively, (c), (d) the Y-V channels of the YUV colorspace without and with thresholds, respectively, (e), (f) the H-S channels of the HSV colorspace without and with thresholds, respectively.

	δX_c (pix)	δY_c (pix)	δA (pix)	δB (pix)	$\delta\phi$ (deg)
RG	2.15	2.06	2.36	1.65	7.62
YV	2.03	2.20	2.38	1.82	8.26
YU	3.72	9.30	2.96	2.70	18.30

Table 8.3: Tracking errors for different colorspace

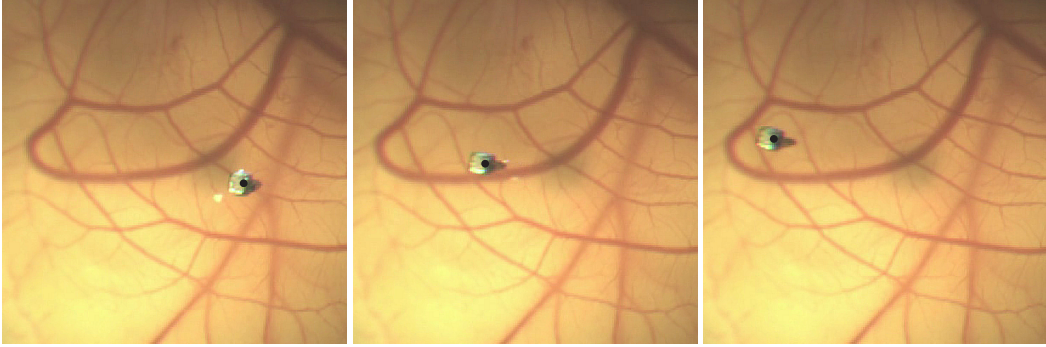


Figure 8.8: Tracking a $2\text{ mm} \times 1\text{ mm} \times 1\text{ mm}$ NdFeB device, equipped with a hypodermic needle as it moves on a chorioallantoic membrane to perform puncture experiments. The dot shows the microdevice’s position. To simulate the effects of human eye optics, we position the CAM under the lens of a model eye and an additional ophthalmic lens. Images were captured with a microscope.

8.3.4 Tracking Microdevices on CAM Vessels

We can use this tracking algorithm on a microdevice equipped with a needle as it moves to puncture veins on the chorioallantoic membrane of a chicken embryo. The CAM is imaged through the lenses of the model eye and the additional ophthalmoscopic lens (Fig. 8.8).

8.3.5 Tracking in a Model Eye Using Color/Shape Information

In the last experiment we demonstrate the effect of tracking in the best colorspace using shape information. Although the method presented in Sec. 8.2.2 may not be most appropriate for rigid bodies that exhibit projective distortion, in our case the shape variability of the microrobot projections can be effectively captured with the extracted eigenshapes (we use four eigenshapes). We track the microrobot using the R-G channels of the RGB colorspace, and

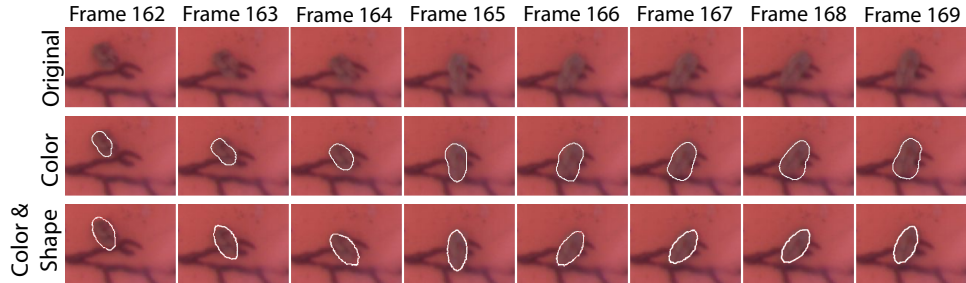


Figure 8.9: Tracking using color information and color/shape information, for different frame sequences.

we impose relatively lower thresholds ($t_l = 0$, $t_h = 0.6$), since this ensures that the full microrobot is always detected even with some misclassifications. The misclassifications are discarded by the shape information. Figure 8.9 compares tracking in R-G and tracking in R-G using shape information; when shape information is incorporated the results are improved.

8.4 Conclusions

In this chapter we presented a complete approach to tracking microrobots for manipulation and intraocular operations. Starting from colorspace evaluation, we selected the colorspace and channels that carry the most information. To decrease erroneous tracking, we introduced thresholds to maximize the object-from-background separation. We extended an available real-time level-set tracking algorithm to handle the thresholds and shape information. The colorspace and threshold selection, and the shape-prior extraction can be completed off-line. We showed the effectiveness of our approach through different experiments.

Chapter 9

Summary: Contributions and Conclusions

9.1 Research Contributions

The key aspects of the presented work are twofold:

1. Theoretically and practically examine the problem of estimating the position of untethered microdevices that move in the interior of the human eye in order to provide information to an electromagnetic field controller.
2. Theoretically and experimentally investigate the feasibility of performing truly minimally invasive ophthalmic surgery using microrobots.

We examined the methods of ophthalmic imaging in order to understand how the intraocular environment projects externally. This involved a thorough examination of the optical systems involved. We developed a new depth-from-focus algorithm, one that is applied on a complex optical system such as the human eye. Research and contribution of the algorithm is that it avoids using approximations that only work close to the axis and are only valid for simple optical systems.

Additionally, we presented a rigid-body-based pose-estimation algorithm which does not require focus information and is, thus, easier to use. We introduced a method to examine cascades of refractive optical elements and extract a model of projection that can be subsequently used in common computer vision algorithms. We developed this method for the optical system of the human eye, but it can be adapted for other optical systems as well.

We used human-eye models and designed our own cascade of lenses in order to conduct our experiments. The lenses were fabricated using biomet-

ric data extracted from the literature. Since we were the first to examine localization of intraocular devices with computer vision methods, our experimental data can be used as a basis for comparison with future research.

With clever fabrication of lenses, one can give observation systems such as optical microscopes the ability to monocularly extract position information.

We suggested a colorspace evaluation criterion and a real time level-set tracking algorithm in order to robustly track multiple microdevices and objects during micromanipulation or microsurgery. This algorithm was evaluated under various scenarios. Additionally, we implemented a method that coupled color and shape information. However, the additional information proved a bottleneck in algorithmic performance which can be overcome by implementing the algorithm in C++ or on the GPU.

Microrobots are a promising approach for improving ophthalmic surgery. Until now, however, all the experimental work had been conducted in silicone oils, and there was no strong connection with the limitations and challenges that are introduced during real operations. This work, through experiments in synthesized vitreous humors and in cadaver porcine eyes, succeeded in showing that permanent magnetic microrobots will be capable of moving in vitreous humors with similar properties to the aging human eye. We only examined gradient forces, and the experimental results show the potential of microrobots being used without requiring a vitrectomy.

The work in this thesis led to several publications. Specifically, the work on imaging was published in BioRob 2008 [Bergeles *et al.*, 2008]. Based on this work, we developed design considerations for a miniaturized mechatronic ophthalmoscope; we patented our ideas in (WO 2010/034502 A2) [Shamaei *et al.*, 2010]. Focus-based wide-angle localization was introduced in IROS 2009 [Bergeles *et al.*, 2009c], and MICCAI 2009 [Bergeles *et al.*, 2009b]. The conclusive version of this work, including sensitivity analysis and calibration was reported in TBME [Bergeles *et al.*, 2010b]. Our method for tracking microdevices for ophthalmic surgery was published in ICRA 2009 [Bergeles *et al.*, 2009a]. The *in vitro* and *ex vivo* feasibility study appeared as a poster at the workshop of “Mesoscale Robotics for Medical Interventions” of ICRA 2010 [Bergeles *et al.*, 2010a]. Initial work on rigid-body based intraocular

localization has been accepted to ICRA 2011 [Bergeles *et al.*, 2011 to appear], and our completed work, including sensitivity analysis and servoing, has been submitted to TRO [Bergeles *et al.*, 2011 submitted]. Parts of the knowledge accumulated during this research will be transferred to Aeon Scientific, AG., a spin-off company from our Institute.

9.2 Conclusion

Microrobots for ophthalmic surgery and localized intraocular drug delivery have the potential to enhance the capabilities of ophthalmic surgeons and improve the effectiveness of existing treatments. Existing work has addressed the problem of controlling the magnetic microdevices, and a prototype electromagnetic control system has been developed. However, the methods for providing position feedback of the intraocular devices to the controllers had not been considered. This dissertation, through work on optical modeling of the human eye, focus-based and model-based localization, and the introduction of color-based tracking methods, provides methods to extract the necessary location information. These contributions together with our conclusions from the *in vitro* and *ex vivo* experimentation answer fundamental questions and constitute a step towards making intraocular operations with microrobots a reality.

References

- [Abbott *et al.*, 2007] J. J. Abbott, O. Ergeneman, M. P. Kummer, A. M. Hirt, and B. J. Nelson. Modeling magnetic torque and force for controlled manipulation of soft-magnetic bodies. *IEEE Trans. Robotics*, 23(6):1247–1252, 2007.
- [Albert and Lucarelli, 2004] D. M. Albert and M. J. Lucarelli, editors. *Clinical Atlas of Procedures in Ophthalmic Surgery*. AMA Press, first edition, 2004.
- [Ascari *et al.*, 2004] L. Ascari, U. Bertocchi, C. Laschi, C. Stefanini, A. Starita, and P. Dario. A segmentation algorithm for a robotic micro-endoscope for exploration of the spinal cord. *IEEE Int. Conf. Robotics and Automation*, pages 491–496, 2004.
- [Atchison and Smith, 2000] D. A. Atchison and G. Smith. *Optics of the human eye*. Butterworth-Heinemann Medical, 2000.
- [Atchison *et al.*, 2004] D. A. Atchison, C. E. Jones, K. L. Schmid, N. Pritchard, J. M. Pope, W. E. Strugnell, and R. A. Riley. Eye shape in emmetropia and myopia. *Investigative Ophthalmology and Visual Science*, 45(10):3380–3386, 2004.
- [Atchison *et al.*, 2005] D. A. Atchison, N. Pritchard, K. L. Schmid, D. H. Scott, C. E. Jones, and J. M. Pope. Shape of the retinal surface in emmetropia and myopia. *Investigative Ophthalmology and Visual Science*, 46(8):2698–2707, 2005.
- [Baker and Nayar, 1999] S. Baker and S. K. Nayar. A theory of single-viewpoint catadioptric image formation. *Int. J. Computer Vision*, 35(2):175–196, 1999.

- [Bakutkin *et al.*, 1987] V. V Bakutkin, I. L. Maksimova, P. I. Saprykin, V. T. Tuchin, and L. P. Subochkin. Diffusion of light by the human sclera. *J. Applied Spectroscopy*, 1(46):86–89, 1987.
- [Balda, 2009] M. Balda. LMFSolve.m: Levenberg-Marquardt-Fletcher algorithm for nonlinear least-squares problems, 2009.
- [Becker *et al.*, 2009a] B. C. Becker, V. Sandrine, R. A. MacLachlan, G. D. Hager, and C. N. Riviere. Active guidance of a handheld micromanipulator using visual servoing. *Int. Conf. Robotics and Automation*, pages 339–344, 2009.
- [Becker *et al.*, 2009b] B. C. Becker, C. R. Valdivieso, J. Biswas, L. A. Lobes, and C. N. Riviere. Active guidance for laser retinal surgery with a handheld instrument. *Int. Conf. Engineering in Medicine and Biology*, 1:5587–5589, 2009.
- [Bergeles *et al.*, 2008] C. Bergeles, K. Shamaei, J. J. Abbott, and B. J. Nelson. On imaging and localizing untethered intraocular devices with a stationary camera. *IEEE Int. Conf. Biomedical Robotics and Biomechatronics*, pages 489–494, 2008.
- [Bergeles *et al.*, 2009a] C. Bergeles, G. Fagogenis, J. J. Abbott, and B. J. Nelson. Tracking intraocular microdevices based on colorspace evaluation and statistical color/shape information. *IEEE Int. Conf. Robotics and Automation*, pages 3934–3939, 2009.
- [Bergeles *et al.*, 2009b] C. Bergeles, K. Shamaei, J. J. Abbott, and B. J. Nelson. Wide-angle intraocular imaging and localization. *Int. Conf. Medical Image Computing and Computer Assisted Intervention*, pages 540–548, 2009.
- [Bergeles *et al.*, 2009c] C. Bergeles, K. Shamaei, J. J. Abbott, and B. J. Nelson. Wide-angle localization of intraocular devices from focus. *IEEE/RSJ Int. Conf. Intelligent Robots and Systems*, pages 4523–4528, 2009.

-
- [Bergeles *et al.*, 2010a] C. Bergeles, M. P. Kummer, B. E. Kratochvil, J. J. Abbott, and B. J. Nelson. *Ex vivo* experiments with intraocular micro-robots. *IEEE Int. Conf. Robotics and Automation, Workshop on Mesoscale Robotics for Medical Interventions, Poster Presentation*, 2010.
- [Bergeles *et al.*, 2010b] C. Bergeles, K. Shamaei, J. J. Abbott, and B. J. Nelson. Single-camera focus-based localization of intraocular devices. *IEEE Trans. Biomedical Engineering*, 57(8):2064–2074, 2010.
- [Bergeles *et al.*, 2011 submitted] C. Bergeles, B. E. Kratochvil, and B. J. Nelson. Visually servoing intraocular microrobots. *IEEE Trans. Robotics*, 2011, submitted.
- [Bergeles *et al.*, 2011 to appear] C. Bergeles, B. E. Kratochvil, and B. J. Nelson. Model-based localization of intraocular microrobots for wireless electromagnetic control. *IEEE Int. Conf. Robotics and Automation*, 2011, to appear.
- [Bettini *et al.*, 2004] A. Bettini, P. Marayong, S. Lang, A. M. Okamura, and G. D. Hager. Vision-assisted control for manipulation using virtual fixtures. *IEEE Trans. Robotics*, 20(6):953–966, 2004.
- [Calkins and Hochheimer, 1980] J. L. Calkins and B. F. Hochheimer. Retinal light exposure from ophthalmoscopes, slit lamps, and overhead surgical lamps. an analysis of potential hazards. *Investigative Ophthalmology and Visual Science*, 19(9):1009–1015, 1980.
- [Campbell, 1984] M. C. W. Campbell. Measurement of refractive index in an intact crystalline lens. *Vision Research*, 24(5):409–415, 1984.
- [Carney *et al.*, 1997] L. G. Carney, J. C. Mainstone, and B. A. Henderson. Corneal topography and myopia: A cross-sectional study. *Investigative Ophthalmology and Visual Science*, 38(2):311–320, 1997.
- [Cattin *et al.*, 2006] P. Cattin, H. Bay, L. Van Gool, and G. Szekely. Retina mosaicing using local features. *Int. Conf. Medical Image Computing and Computer Assisted Intervention*, pages 185–192, 2006.

-
- [Chanwimaluang *et al.*, 2009] T. Chanwimaluang, G. Fan, G. G. Yen, and S. R. Fransen. 3D retinal curvature estimation. *IEEE Trans. Information Technology in Biomedicine*, 13(6):997–1005, 2009.
- [Chaumette and Hutchinson, 2006] F. Chaumette and S. Hutchinson. Visual servo control: basic approaches. *IEEE Robotics and Automation Magazine*, 13(4):82–90, 2006.
- [Chaumette and Hutchinson, 2007] F. Chaumette and S. Hutchinson. Visual servo control: advanced approaches. *IEEE Robotics and Automation Magazine*, 14(1):109–118, 2007.
- [Chen *et al.*, 2006] P. J. Chen, D. Rodger, M. Humayun, and Y. C. Tai. Unpowered spiral-tube parylene pressure sensor for intraocular pressure sensing. *Sensor and Actuators A: Physical*, 127(2):276–282, 2006.
- [Chen *et al.*, 2008] P. J. Chen, D. Rodger, S. Saati, M. Humayun, and Y. C. Tai. Implantable parylene-based wireless intraocular pressure sensor. *IEEE Int. Conf. Micro Electro Mechanical Systems*, pages 58–61, 2008.
- [Chen, 2008] P. J. Chen. *Implantable wireless intraocular pressure sensors*. PhD thesis, California Institute of Technology, 2008.
- [Coile and O’Keefe, 1988] D. C. Coile and L. P. O’Keefe. Schematic eyes for domestic animals. *Ophthalmic and Physiological Optics*, 8(2):215–219, 1988.
- [Congdon *et al.*, 2004a] N. Congdon, B. O’Colmain, C. C. Klaver, R. Klein, B. Munoz, D. S. Friedman, J. Kempen, H. R. Taylor, and P. Mitchell. Causes and prevalence of visual impairment among adults in the United States. *Archives of Ophthalmology*, 122(4):477–485, 2004.
- [Congdon *et al.*, 2004b] N. Congdon, J. R. Vingerling, B. E. Klein, S. West, D. S. Friedman, J. Kempen, B. O’Colmain, S. Y. Wu, and H. R. Taylor. Prevalence of cataract and pseudophakia/aphakia among adults in the United States. *Archives of Ophthalmology*, 122(4):487–494, 2004.

- [Cullity and Graham, 2009] B. D. Cullity and C. D. Graham. *Introduction to Magnetic Materials*. Hoboken, New Jersey: John Wiley and Sons, second edition, 2009.
- [Das *et al.*, 2001] H. Das, T. Ohm, C. Boswell, R. Steele, and G. Rodriguez. Robot-assisted microsurgery development at JPL. *Information Technologies in Medicine, Vol. II: Rehabilitation and Treatment*, pages 85–99, 2001.
- [Deguchi *et al.*, 2000] K. Deguchi, D. Kawamata, K. Mizutani, H. Hontani, and K. Wakabayashi. 3D fundus shape reconstruction and display from stereo fundus images. *IEICE Trans. Information and Systems*, 83(7):1408–1414, 2000.
- [Delori *et al.*, 2007] F. C. Delori, R. H. Webb, and D. H. Sliney. Maximum permissible exposures for ocular safety (ANSI 2000), with emphasis on ophthalmic devices. *J. Optical Society of America A*, 25(5):1250–1265, 2007.
- [Derrien and Konolige, 2000] S. Derrien and K. Konolige. Approximating a single viewpoint in panoramic imaging devices. *IEEE Int. Conf. Robotics and Automation*, pages 3931–3938, 2000.
- [Dewan *et al.*, 2004] M. Dewan, P. Marayong, A. M. Okamura, and G. D. Hager. Vision-based assistance for ophthalmic microsurgery. *Int. Conf. Medical Image Computing and Computer Assisted Intervention*, pages 49–57, 2004.
- [Dogangil *et al.*, 2008] G. Dogangil, O. Ergeneman, J. J. Abbott, S. Pane, H. Hall, S. Muntwyler, and B. J. Nelson. Toward targeted retinal drug delivery with wireless magnetic microrobots. *IEEE/RSJ Int. Conf. Intelligent Robots and Systems*, pages 1921–1926, 2008.
- [Dogangil *et al.*, 2010] G. Dogangil, B. L. Davies, and F. Rodriguez y Baena. A review of medical robotics for minimally invasive soft tissue surgery. *J. Engineering in Medicine*, 224(5):653–679, 2010.

- [Doignon *et al.*, 2005] C. Doignon, P. Graebing, and M. de Mathelin. Real-time segmentation of surgical instruments inside the abdominal cavity using a joint hue saturation color feature. *Real-Time Imaging*, 11(5-6):429–442, 2005.
- [Drummond and Cipolla, 2002] T. Drummond and R. Cipolla. Real-time visual tracking of complex structures. *IEEE Trans. Pattern Analysis and Machine Intelligence*, pages 932–946, 2002.
- [Dubbelman *et al.*, 2006] M. Dubbelman, V. Sicam, and G. L. Van der Heijde. The shape of the anterior and posterior surface of the aging human cornea. *Vision Research*, 46(6-7):993–1001, 2006.
- [Ens and Lawrence, 1993] J. Ens and P. Lawrence. An investigation of methods for determining depth from focus. *IEEE Trans. Pattern Analysis and Machine Intelligence*, 15(2):97–108, 1993.
- [Ergeneman *et al.*, 2008a] O. Ergeneman, J. J. Abbott, G. Dogangil, and B. J. Nelson. Functionalizing intraocular microrobots with surface coatings. *IEEE Int. Conf. Biomedical Robotics and Biomechatronics*, pages 232–237, 2008.
- [Ergeneman *et al.*, 2008b] O. Ergeneman, G. Dogangil, M. P. Kummer, J. J. Abbott, M. K. Nazeeruddin, and B. J. Nelson. A magnetically controlled wireless optical oxygen sensor for intraocular measurements. *IEEE Sensors*, 8(1-2):29–37, 2008.
- [Escudero-Sanz and Navarro, 1999] I. Escudero-Sanz and R. Navarro. Off-axis aberrations of a wide-angle schematic eye model. *J. Optical Society of America A*, 16(8):1881–1891, 1999.
- [Espinosa-Romero and Martinez-Perez, 2005] A. Espinosa-Romero and M. E. Martinez-Perez. Optical 3D reconstruction of retinal blood vessels from a sequence of views. *Proc. SPIE, 3D Inspection and Metrology*, 5776:605–615, 2005.

-
- [Focal Encyclopedia of Photography, 1965] Focal Encyclopedia of Photography. *The focal encyclopedia of photography*. Focal Press, fully revised edition, 1965.
- [Friedman *et al.*, 2004a] D. S. Friedman, M. P. H. O’Colmain, B. Munoz, C. Sandra, M. A. Tomany, C. McCarty, P. T. V. M. de Jong, P. Mitchel, J. Kempen, and N. Congdon. Prevalence of age-related macular degeneration in the United States. *Archives of Ophthalmology*, 122(4):564–572, 2004.
- [Friedman *et al.*, 2004b] D. S. Friedman, R. C. Wolfs, B. O’Colmain, B. E. Klein, H. R. Taylor, S. West, M. C. Leske, P. Mitchell, N. Congdon, and J. Kempen. Prevalence of open-angle glaucoma among adults in the United States. *Archives of Ophthalmology*, 122(4):532–538, 2004.
- [Frutiger *et al.*, 2010] D. R. Frutiger, B. E. Kratochvil, K. Vollmers, and B. J. Nelson. Small, fast, and under control: wireless resonant magnetic micro-agents. *Int. J. Robotics Research*, 29(5):613–636, 2010.
- [Genina *et al.*, 2006] E. A. Genina, A. N. Bashkatov, Y. P. Sinichkin, and V. V Tuchin. Optical clearing of the eye sclera *in vivo* caused by glucose. *Quantum Electronics*, 36(12):1119–1124, 2006.
- [Gliss *et al.*, 2004] C. Gliss, J. M. Parel, J. T. Flynn, H. Pratisto, and P. Niederer. Toward a miniaturized fundus camera. *J. Biomedical Optics*, 9:126, 2004.
- [Goncharov and Dainty, 2007] A. V. Goncharov and C. Dainty. Wide-field schematic eye models with gradient-index lens. *J. Optical Society of America A*, 24(8):2157–2174, 2007.
- [Grossberg and Nayar, 2005] M. D. Grossberg and S. K. Nayar. The raxel imaging model and ray-based calibration. *Int. J. Computer Vision*, 61(2):119–137, 2005.

- [Guizar-Sicairos *et al.*, 2008] M. Guizar-Sicairos, S. T. Thurman, and J. R. Fienup. Efficient subpixel image registration algorithms. *Optics Letters*, 33(2):156–158, 2008.
- [Gullstrand, 1909] A. Gullstrand. Die dioptrik des auges. *Leopold Voss*, 1:226–320, 1909.
- [Gupta *et al.*, 1999] P. Gupta, P. S. Jensen, and E. de Juan. Surgical forces and tactile perception during retinal microsurgery. *Int. Conf. Medical Image Computing and Computer Assisted Intervention*, pages 1218–1225, 1999.
- [Gwb International, Ltd., 2010] Gwb International, Ltd. Model eye (3 mm pupil) from Gwb International, Ltd., 2010.
- [Hager *et al.*, 2008] G. D. Hager, A. M. Okamura, P. Kazanzides, L. Whitcomb, G. Fichtinger, and R. H. Taylor. Surgical and interventional robotics: Part iii. *IEEE Robotics and Automation Magazine*, 15(4):84–93, 2008.
- [Hagn *et al.*, 2008] U. Hagn, T. Ortmaier, R. Konietschke, B. Kubler, U. Seibold, A. Tobergte, M. Nickl, S. Jorg, and G. Hirzinger. Telemanipulator for remote minimally invasive surgery. *IEEE Robotics and Automation Magazine*, 15(4):28–38, 2008.
- [Hecht, 2002] E. Hecht. *Optics*. San Francisco, CA, Addison Wesley, fourth edition, 2002.
- [Holligan *et al.*, 2003] D. L. Holligan, G. T. Gillies, and J. P. Dailey. Magnetic guidance of ferrofluidic nanoparticles in an *in vitro* model of intraocular retinal repair. *Nanotechnology*, 14(6):661–666, 2003.
- [HUCO Vision, 2008] HUCO Vision. S5.7010 lens from FCI Ophthalmics, 2008.
- [Hutchinson *et al.*, 1996] S. Hutchinson, G. D. Hager, and P. I. Corke. A tutorial on visual servo control. *IEEE Trans. Robotics*, 12(5):651–670, 1996.

-
- [Ikuta *et al.*, 1998] K. Ikuta, T. Kato, and S. Nagata. Optimum designed microactive forceps with built-in fiberscope for retinal microsurgery. *Int. Conf. Medical Image Computing and Computer Assisted Intervention*, pages 411–420, 1998.
- [Jagtap and Riviere, 2004] A. D. Jagtap and C. N. Riviere. Applied force during vitreoretinal microsurgery with handheld instruments. *IEEE Int. Conf. Engineering in Medicine and Biology*, pages 2771–2773, 2004.
- [Jensen *et al.*, 1997] P. S. Jensen, K. W. Grace, R. Attariwala, J. E. Colgate, and M. R. Glucksberg. Toward robot-assisted vascular microsurgery in the retina. *Graefe’s Archive for Clinical and Experimental Ophthalmology*, 235(11):696–701, 1997.
- [Joint Committee for Guides in Metrology, 2008] Joint Committee for Guides in Metrology. *Evaluation of measurement data – Guide to the expression of uncertainty in measurement*. JCGM, first edition, 2008.
- [Jones *et al.*, 2005] C. E. Jones, D. A. Atchison, R. Meder, and J. M. Pope. Refractive index distribution and optical properties of the isolated human lens measured using magnetic resonance imaging (MRI). *Vision Research*, 45(18):2352–2366, 2005.
- [Kass *et al.*, 1988] M. Kass, A. Witkin, and D. Terzopoulos. Snakes: active contour models. *Int. J. Computer Vision*, 1(4):321–331, 1988.
- [Kempen *et al.*, 2004] J. H. Kempen, B. O’Colmain, M. C. Leske, S. M. Haffner, R. Klein, S. E. Moss, H. R. Taylor, and R. F. Hamman. The prevalence of diabetic retinopathy among adults in the United States. *Archives of ophthalmology*, 122(4):552, 2004.
- [Kirschkamp *et al.*, 2004] T. Kirschkamp, M. Dunne, and J. C. Barry. Phakometric measurement of ocular surface radii of curvature, axial separations and alignment in relaxed and accommodated human eyes. *J. Ophthalmic and Physiological Optics*, 24(2):65–73, 2004.

- [Kratochvil *et al.*, 2009] B. E. Kratochvil, L. X. Dong, and B. J. Nelson. Real-time rigid-body visual tracking in a scanning electron microscope. *Int. J. Robotics Research*, 28(4):498–511, 2009.
- [Kratochvil, 2008] B. E. Kratochvil. *Visual tracking for nanorobotic manipulation and 3d reconstruction in an electron microscope*. PhD thesis, ETH Zurich, 2008.
- [Kumar *et al.*, 2000] R. Kumar, P. Berkelman, P. Gupta, A. Barnes, P. S. Jensen, L. Whitcomb, and R. Taylor. Preliminary experiments in cooperative human/robot force control for robot assisted microsurgical manipulation. *IEEE Int. Conf. Robotics and Automation*, pages 610–617, 2000.
- [Kummer *et al.*, 2007] M. P. Kummer, J. J. Abbott, S. Dinser, and B. J. Nelson. Artificial vitreous humor for *in vitro* experiments. *IEEE Int. Conf. Engineering in Medicine and Biology*, pages 6406–6409, 2007.
- [Kummer *et al.*, 2010] M. P. Kummer, J. J. Abbott, B. E. Kratochvil, R. Borer, A. Sengul, and B. J. Nelson. OctoMag: An electromagnetic system for 5-DOF wireless micromanipulation. *IEEE Trans. Robotics*, pages 1006–1017, 2010.
- [Lambda Research Corporation, 2001] Lambda Research Corporation. OSLO optics reference, version 6.1, 2001.
- [Lambda Research Corporation, 2010] Lambda Research Corporation. Lambda Research Corporation, 2010.
- [Lee and Robinson, 2009] S. S. Lee and M. R. Robinson. Novel drug delivery systems for retinal diseases. *Ophthalmic Research*, 41(3):124–135, 2009.
- [Leventon *et al.*, 2000] M. E. Leventon, W. E. L. Grimson, and O. Faugeras. Statistical shape influence in geodesic active contours. *IEEE Int. Conf. Computer Vision and Pattern Recognition*, pages 316–323, 2000.
- [Li *et al.*, 2008] S. K. Li, M. J. Lizak, and E. K. Jeong. MRI in ocular drug delivery. *NMR in Biomedicine*, 21(9):941–956, 2008.

-
- [Lin and Medioni, 2008] Y. Lin and G. Medioni. Retinal image registration from 2D to 3D. *IEEE Int. Conf. Computer Vision and Pattern Recognition*, pages 1–8, 2008.
- [Liou and Brennan, 1997] H. L. Liou and N. A. Brennan. Anatomically accurate, finite model eye for optical modeling. *J. Optical Society of America A*, 14(8):1684–1695, 1997.
- [Liu *et al.*, 2009] D. Liu, N. B. Wood, X. Y. Xu, N. Witt, A. D. Hughes, and T. SAMcG. 3D reconstruction of the retinal arterial tree using subject-specific fundus images. *Advances in Computational Vision and Medical Image Processing*, pages 187–201, 2009.
- [Lourakis, 2004] M. I. A. Lourakis. levmar: Levenberg-Marquardt nonlinear least-squares algorithms in C/C++, 2004.
- [Luo *et al.*, 2006] R. Luo, X. Y. Yang, X. F. Peng, and Y. F. Sun. Three-dimensional tracking of fluorescent particles applied to micro-fluidic measurements. *J. Micromechanics and Microengineering*, 16(8):1689–1699, 2006.
- [Machemer *et al.*, 1972] R. Machemer, H. Buettner, and E. Norton. Vitrectomy: a *pars plana* approach. *Trans. Am. Acad. Ophthalmology and Otolaryngology*, 75:813, 1972.
- [Mejia-Barbosa and Malacara-Hernandez, 2001] Y. Mejia-Barbosa and D. Malacara-Hernandez. A review of methods for measuring corneal topography. *Optometry and Vision Science*, 78(4):240–253, 2001.
- [Meng *et al.*, 2005] E. Meng, P. J. Chen, D. Rodger, Y. C. Tai, and M. Humayun. Implantable parylene MEMS for glaucoma therapy. *IEEE Int. Conf. Engineering in Medicine and Biology*, pages 116–119, 2005.
- [Mitchell *et al.*, 2007] B. Mitchell, J. Koo, I. Iordachita, P. Kazanzides, A. Kapoor, J. Handa, G. D. Hager, and R. H. Taylor. Development and application of a new steady-hand manipulator for retinal surgery. *IEEE Int. Conf. Robotics and Automation*, pages 623–629, 2007.

-
- [Moreno-Noguer *et al.*, 2006] F. Moreno-Noguer, A. Sanfeliu, and D. Samaras. A target dependent colorspace for robust tracking. *Int. Conf. Pattern Recognition*, 3:43–46, 2006.
- [Murray *et al.*, 1994] R. M. Murray, Z. Li, and S. S. Sastry. *A mathematical introduction to robotic manipulation*. CRC, 1994.
- [Nagy *et al.*, 2008] Z. Nagy, O. Ergeneman, J. J. Abbott, M. Hutter, A. M. Hirt, and B. J. Nelson. Modeling assembled-MEMS microrobots for wireless magnetic control. *IEEE Int. Conf. Robotics and Automation*, pages 874–879, 2008.
- [Navarro *et al.*, 2006] R. Navarro, L. Gonzalez, and J. O. S. L. Hernandez-Matamoros. On the prediction of optical aberrations by personalized eye models. *Optometry and Vision Science*, 83(6):371–381, 2006.
- [Nelson *et al.*, 2010] B. J. Nelson, I. K. Kaliakatsos, and J. J. Abbott. Microrobots for minimally invasive medicine. *Annual Review of Biomedical Engineering*, 12:55–85, 2010.
- [Nickerson, 2005] C. S. Nickerson. *Engineering the mechanical properties of ocular tissues*. PhD thesis, California Institute of Technology, 2005.
- [Norrby, 2008] S. Norrby. Sources of error in intraocular lens power calculation. *J. Cataract and Refractive Surgery*, 34(3):368–376, 2008.
- [Osher and Fedkiw, 1987] S. Osher and R. P. Fedkiw. Level set methods. *J. Computational Physics*, 1987.
- [Paragios and Deriche, 2000] N. Paragios and R. Deriche. Geodesic active contours and level sets for the detection and tracking of moving objects. *IEEE Trans. Pattern Analysis and Machine Intelligence*, 22(3), 2000.
- [Parker, 2003] A. Parker. *In the Blink of an Eye*. Perseus Publishing, first edition, 2003.

- [Patel *et al.*, 1995] S. Patel, J. Marshall, and F. W. Fitzke. Refractive index of the human corneal epithelium and stroma. *J. Refractive Surgery*, 11(2):1100–1105, 1995.
- [Pezzementi *et al.*, 2009] Z. Pezementi, S. Voros, and G. D. Hager. Articulated object tracking by rendering consistent appearance parts. *IEEE Int. Conf. Robotics and Automation*, pages 3940–3947, 2009.
- [Pomerantzeff, 1976] O. Pomerantzeff. Wide-angle ophthalmoscope employing transillumination. US Patent 3,954,329, May 4 1976.
- [Quigley and Vitale, 1997] H. A. Quigley and S. Vitale. Models of open-angle glaucoma prevalence and incidence in the United States. *Investigative Ophthalmology and Visual Science*, 38(1):83, 1997.
- [Read *et al.*, 2006] S. A. Read, M. J. Collins, L. G. Carney, and R. J. Franklin. The topography of the central and peripheral cornea. *Investigative Ophthalmology and Visual Science*, 47(4):1404–1415, 2006.
- [Riviere *et al.*, 1998] C. N. Riviere, R. S. Rader, and N. V. Thakor. Adaptive canceling of physiological tremor for improved precision in microsurgery. *IEEE Trans. Biomedical Engineering*, 45(7):839–846, 1998.
- [Riviere *et al.*, 2003] C. N. Riviere, W. T. Ang, and P. K. Khosla. Toward active tremor canceling in handheld microsurgical instruments. *IEEE Trans. Robotics and Automation*, 19(5):793–800, 2003.
- [Robocup, 2009] Robocup. Nanogram information, 2009.
- [Roffman, 1991] J. H. Roffman. Lens design method and resulting aspheric lens, December 1991. U.S. Patent 5,050,981.
- [Rousson and Paragios, 2002] M. Rousson and N. Paragios. Shape priors for level set representations. *Europ. Conf. Computer Vision*, 2351:78–92, 2002.

-
- [Shamaei *et al.*, 2010] K. Shamaei, C. Bergeles, J. J. Abbott, and B. J. Nelson. Ophthalmoscopy using direct sensing. Patent W.O. 2010/034502 A2, April 1 2010.
- [Shi and Karl, 2005] Y. Shi and W. C. Karl. Real-time tracking using level sets. *IEEE Int. Conf. Computer Vision and Pattern Recognition*, 2:34–41, 2005.
- [Smith and Atchison, 1997] G. Smith and D. A. Atchison. *The eye and visual optical instruments*. Cambridge University Press, 1997.
- [Snead *et al.*, 1992] M. P. Snead, M. P. Rubinstein, and P. M. Jacobs. The optics of fundus examination. *Survey of Ophthalmology*, 36(6):439–445, 1992.
- [Soman and Banerjee, 2003] N. Soman and R. Banerjee. Artificial vitreous replacements. *Bio-medical Materials and Engineering*, 13(1):59–74, 2003.
- [Stern and Efros, 2005] H. Stern and B. Efros. Adaptive color space switching for tracking under varying illumination. *Image and Vision Computing*, 23(3):353–364, 2005.
- [Subbarao and Surya, 1994] M. Subbarao and G. Surya. Depth from defocus: A spatial domain approach. *Int. J. Computer Vision*, 13(3):271–294, 1994.
- [Sumipro BV, 2010] Sumipro BV. Sumipro bv, 2010.
- [Sun *et al.*, 2004] Y. Sun, S. Duthaler, and B. J. Nelson. Autofocusing in computer microscopy: selecting the optimal focus algorithm. *J. Microscopy Research and Technique*, 65(3):139–149, 2004.
- [Swaminathan *et al.*, 2006] R. Swaminathan, M. D. Grossberg, and S. K. Nayar. Non-single viewpoint catadioptric cameras: Geometry and analysis. *Int. J. Computer Vision*, 66(3):211–229, 2006.
- [Taylor and Stoianovici, 2003] R. H. Taylor and D. Stoianovici. Medical robotics in computer-integrated surgery. *IEEE Transaction on Robotics and Automation*, 19(5):765–781, 2003.

-
- [Taylor *et al.*, 1999] R. H. Taylor, P. S. Jensen, L. Whitcomb, A. Barnes, R. Kumar, D. Stoianovici, P. Gupta, Z. X. Wang, E. de Juan, and L. Kavoussi. A steady-hand robotic system for microsurgical augmentation. *Int. J. Robotics Research*, 18(12):1201–1210, 1999.
- [Theocharis *et al.*, 2007] I. P. Theocharis, A. Alexandridou, and Z. Tomic. A two-year prospective study comparing lidocain 2% jelly versus peribulbar anaesthesia for 25G and 23G sutureless vitrectomy. *Graefe’s Archive for Clinical and Experimental Ophthalmology*, 245(9):1253–1258, 2007.
- [Tjoa *et al.*, 2001] M. P. Tjoa, S. M. Krishnan, C. Kugean, P. Wang, and R. Doraiswami. Segmentation of clinical endoscopic image based on homogeneity and hue. *IEEE Int. Conf. Engineering in Medicine and Biology*, pages 2665–2668, 2001.
- [Tomasi and Kanade, 1992] C. Tomasi and T. Kanade. Shape and motion from image streams under orthography: a factorization method. *Int. J. Computer Vision*, 9(2):137–154, 1992.
- [Uhlig and Gerding, 2004] C. E. Uhlig and H. Gerding. Illuminated artificial orbit for the training of vitreoretinal surgery *in vitro*. *Eye*, 2(18):183–187, 2004.
- [Ulery *et al.*, 2005] A. L. Ulery, W. F. Chen, R. C. Dorf, O. W. Eshbach, B. D. Tapley, E. N. Ganic, K. Gieck, T. J. Glover, S. I. Heisler, R. G. Hudson, et al. IEEE standard for safety levels with respect to human exposure to radio frequency electromagnetic fields, 3khz to 300ghz. *IEEE Standards*, 2005.
- [Vilipuru and Glasser, 2001] A. S. Vilipuru and A. Glasser. Optical and biometric relationships of the isolated pig crystalline lens. *Ophthalmic and Physiological Optics*, 21(4):296–311, 2001.
- [Volk, 1998] D. A. Volk. Indirect ophthalmoscopy lens for use with split lamp or other biomicroscope, January 6 1998. U.S. Patent 5,706,073.
- [Volk, 2008] Volk. Digital High Mag[®] lens from Volk Optical Inc., 2008.

-
- [Vollmers *et al.*, 2008] K. Vollmers, D. R. Frutiger, B. E. Kratochvil, and B. J. Nelson. Wireless resonant magnetic microactuator for untethered mobile microrobots. *Applied Physics Letters*, 92(14), 2008.
- [Wei *et al.*, 2007] W. Wei, R. Goldman, N. Simaan, H. Fine, and S. Chang. Design and theoretical evaluation of micro-surgical manipulators for orbital manipulation and intraocular dexterity. *IEEE Int. Conf. Robotics and Automation*, pages 3389–3395, 2007.
- [Wei *et al.*, 2009] W. Wei, R. Goldman, H. Fine, S. Chang, and N. Simaan. Modeling and performance evaluation of hybrid multi-arm robots operating on hollow suspended organs. *IEEE Trans. Robotics*, 25(1):147–157, 2009.
- [World Health Organization, 2009] World Health Organization. Visual impairment and blindness. 2009.
- [World Health Organization, 2010] World Health Organization. Priority eye diseases, 2010.
- [Wu *et al.*, 2005] M. Wu, J. W. Roberts, and M. Buckley. Three-dimensional fluorescent particle tracking at micron-scale using a single camera. *Experiments in Fluids*, 38(4):461–465, 2005.
- [Yasukawa *et al.*, 2004] T. Yasukawa, Y. Ogura, Y. Tabata, H. Kimura, P. Wiedemann, and Y. Honda. Drug delivery systems for vitreoretinal diseases. *Progress in Retinal and Eye Research*, 23(3):253–281, 2004.
- [Yeşin *et al.*, 2004] K. B. Yeşin, K. Vollmers, and B. J. Nelson. Guidance of magnetic intraocular microrobots by active defocused tracking. *IEEE/RSJ Int. Conf. Intelligent Robots and Systems*, 4:3309–3314, 2004.
- [Yeşin *et al.*, 2006] K. B. Yeşin, K. Vollmers, and B. J. Nelson. Modeling and control of untethered biomicrobots in a fluidic environment using electromagnetic fields. *Int. J. Robotics Research*, 25(5-6):527–536, 2006.

- [Zadnik *et al.*, 1992] K. Zadnik, D. O. Mutti, and A. J. Adams. The repeatability of measurement of the ocular components. *Investigative Ophthalmology and Visual Science*, 33(7):2325–2333, 1992.
- [Zhang *et al.*, 2009] L. Zhang, J. J. Abbott, L. X. Dong, B. E. Kratochvil, D. Bell, and B. J. Nelson. Artificial bacterial flagella: fabrication and magnetic control. *Applied Physics Letters*, 94:064107, 2009.

Appendix A

Developing a Miniaturized Ophthalmoscope

Eye diseases affect different population categories. Moreover, the large number of cases and the specific characteristics of each disease make constant monitoring of each unique case by specially trained personnel impossible. Especially in developing countries, there is no guarantee that an experienced ophthalmologist will be able to perform the examination. The solution to these problems lies in telemedicine.

Telemedicine involves the use of equipment by general purpose medical personnel, the acquisition of medical data, and the further evaluation of the data by a specialized medical doctor off-site. Usually, ophthalmoscopes are large and not-so-easy to handle and transport (e.g. Panoret 1000 and Nidek AFC-210). In addition, they are costly and thus not widely available in developing areas. Easy-to-use handheld ophthalmoscopes (e.g. direct ophthalmoscopes used by clinicians) do not offer the capability of data storing. For successful telemedical procedures, an easy-to-use, miniaturized, and digital ophthalmoscope needs to be developed. Such a device will also be of particular interest for remote regions of the earth, where highly skilled technical and medical personnel is absent.

A first attempt to create a miniaturized fundus camera is presented in [Gliss *et al.*, 2004]. The authors perform experiments on albino rabbits. The authors report backreflections due to the transpupillary illumination device. Transscleral illumination is also investigated, however, with unsuccessful results due to thickness of the pigmented rabbit sclera. The camera used a cascade of lenses and this led to an increase in size. Moreover, since each lens absorbs and reflects a portion of the light that reaches it, higher radiation of the retina was required.

Based on our analysis on image formation in chapter 3, in this appendix we aim at investigating the feasibility of developing a miniaturized fundus camera that consists of a single aspheric lens that can create an aerial image of the retina³. Such an approach can lead to a small device, and also limit the amount of required retinal radiance.

Two fundamentally individual setups are investigated. First, we examine direct acquisition of the retinal aerial image created by an aspheric lens. Subsequently, we present a light-emitting-diode-based transscleral illuminator. We discuss initial results from experimentation with cadaver porcine eyes. We were unable to fully pursue our ideas to a final product, but we developed our ideas and secured a patent (WO 2010/034502 A2) [Shamaei *et al.*, 2010].

A.1 Optical Construction

An ophthalmoscopic aspheric lens capable of generating a flat aerial image of the retina is used. The aerial image is captured by an image sensor which is directly positioned at the aerial image by a translational mechanism. Figure A.1(a) shows the optical construction considering Navarro’s eye model and an aspheric lens.

The image sensor need not be able to capture the full aerial image at once. It can rotate or translate on the aerial image, and the captured portions of the full retinal image can be stitched together with retinal mosaicing techniques [Cattin *et al.*, 2006].

Magnification and depth-of-field considerations for the final device can be found in chapters 3 and 4.

Focusing can be achieved by translating the sensor, the lens, or by using the natural focusing ability of the crystalline lens (Fig. A.1(b)). A projector is used to show an image to the patient, and guide his crystalline lens to focus on it. The image sensor and the projector are placed in fixed distances

³The primary contributor of the work described in this appendix is Kamran Shamaei, currently at Yale University. Kamran conducted his Master Thesis research at the Institute of Robotics and Intelligent Systems under my supervision, and handled the design and assembly of the ophthalmoscopes.

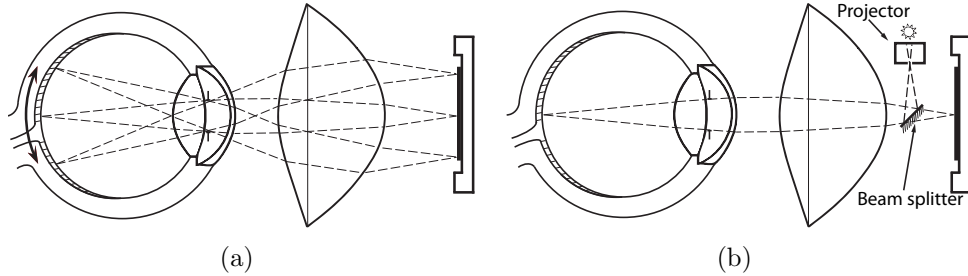


Figure A.1: (a) The basic optical structure that we are considering, and (b) concept of using the accommodating property of the crystalline lens to guide camera focusing.

from the condensing lens, and the ability to see the projected image implies that the aerial retinal image will project on the camera's sensor. A partially reflecting mirror can be used to separate the light path.

A.2 Illumination

With the aim of miniaturization, a non-contact LED-based transscleral illumination method is designed as shown in Fig. A.2. An LED-based light source results in no constraint on the imaging device. LEDs can be aligned in a ring, generating a wide-angle of illumination. Lenses are used to focus the light on the *par plana*, as is suggested in [Pomerantzeff, 1976]. The LEDs normally emit in the visible range. Based on the eye safety characteristics, near-IR and near-UV should be avoided. The required light intensity can be calculated based on the imaging span and safety standards for the eye [Calkins and Hochheimer, 1980; Ulery *et al.*, 2005; Delori *et al.*, 2007].

A.3 Developed Prototypes and Experimental Work

We developed two prototypes: one uses a small sensor that rotates on the aerial image and capture portions of it, and one that uses a large sensor captures the full aerial image at once. The fabricated prototypes can be seen in Fig. A.3 and Fig. A.4.

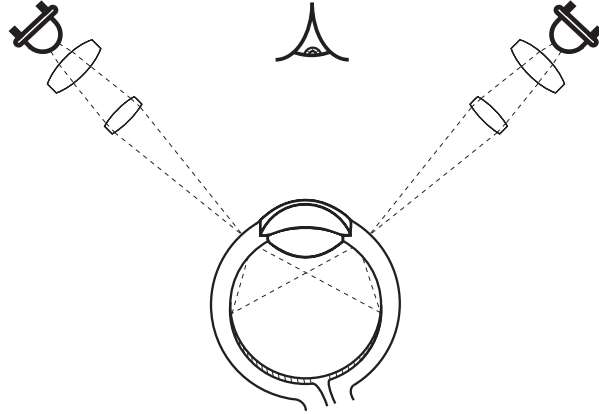


Figure A.2: A transscleral LED-based illumination apparatus. Light is focused on the *pars plana* region of the sclera.

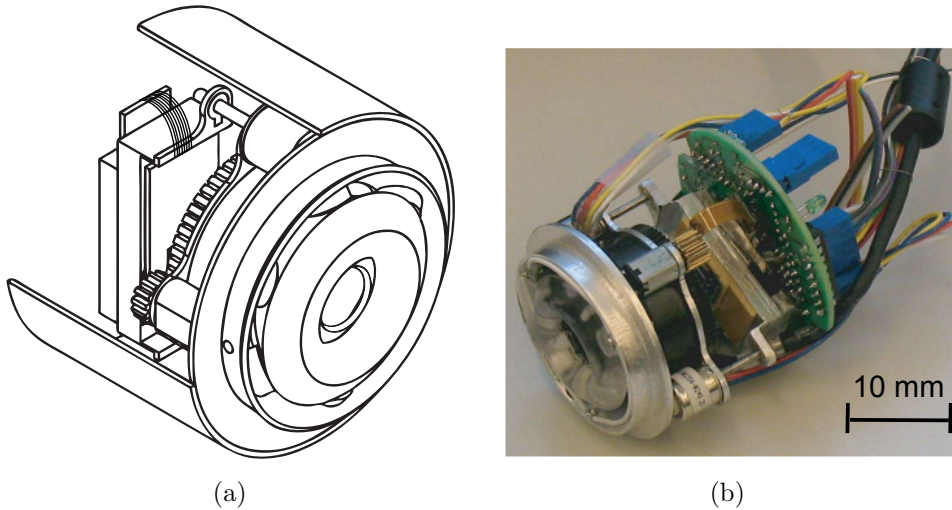


Figure A.3: (a) The device consists of two motors to move the sensor plane and focus on the image, a motor to rotate the sensor in plane, a condensing lens, and a microcontroller. (b) The first crude prototype.

A.4 Discussion

We tested the autofocusing and mosaicing concept of our device by imaging the retina of a model eye. Additionally, we performed experiments with cadaver eyes. However, we were unable to capture an image of their retina; only the choroidal structure was distinguishable, in images that were of poor

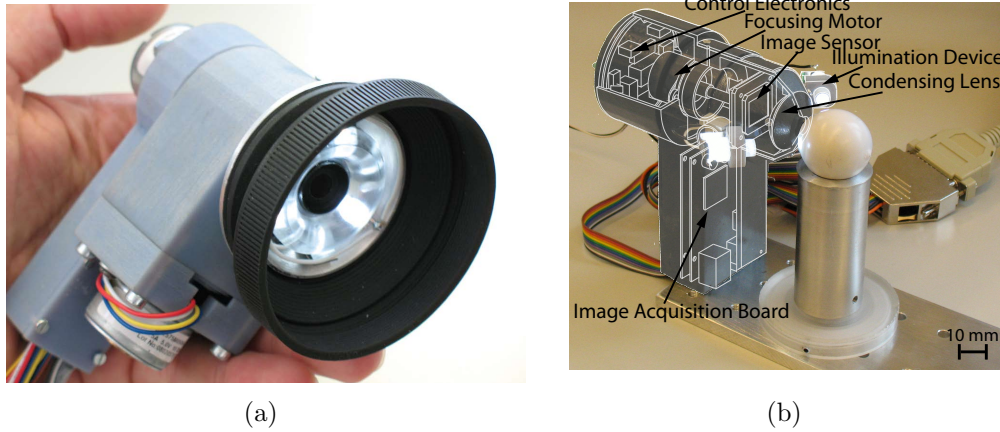


Figure A.4: (a) Prototype that uses a small image sensor that translates to focus, and rotates to capture multiple portions of the created aerial image, and (b) prototype containing a larger higher resolution image sensor that captures a large portion of the retinal image directly.

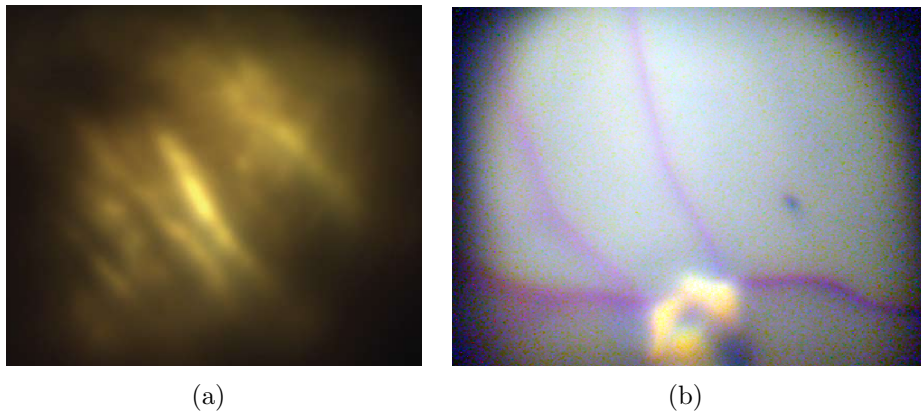


Figure A.5: (a) Using our first prototypes and transscleral illumination, only a part of the choroidal structure with poor quality could be observed, and (b) using an additional contact lens and endoillumination enable us to observe the retina with a better quality.

quality (Fig. A.5(a)). Additionally, we went through the procedure of acquiring a license of *in vivo* testing on pigs. Our tests, however, were not successful. One reason for that was that the pigs were under light anesthesia, and at this state, they can roll their eyeballs towards the interior of the

skull when they perceive strong light.

After consulting experts from Haag-Streit, a Switzerland-based company that specializes in the design and construction of ophthalmoscopes, it was made clear that the biggest problem is proper illumination. Transscleral illumination is indeed an option that is used commercially in products, but most of the existing devices rely on transpupillary illumination. At that point however, we had to bring our research to a halt due to the lack of people available for the project.

With an additional contact lens and endoillumination, we were able to capture images of the retina of a porcine cadaver eye. This demonstrates that with perhaps a contact lens and a good illumination source, a miniaturized ophthalmoscope can be possible.

CHRISTOS BERGELES

Meierwiesenstrasse 54
8064 Zurich, Switzerland

<http://christos.bergeles.net>
christosbergeles@gmail.com
tel: +41 44 632 54 46

PERSONAL DATA

Born in March 1984, single, male, citizen of Greece.

EDUCATION

10/2006–03/2011, Ph. D., Mechanical Engineering
Swiss Federal Institute of Technology (ETH), Zurich, Switzerland
Thesis title: Visually servoing magnetic intraocular microrobots

09/2001–07/2006, Diploma, Electrical and Computer Engineering
National Technical University of Athens (NTUA), Athens, Greece
Major: Computer Science, Minor: Signals, Control, and Robotics
Thesis title: Tracking of moving objects with emphasis on human gestures

RESEARCH INTERESTS

Computer Vision, Robotics, Imaging, Software Engineering.

PROFESSIONAL EXPERIENCE

Research Assistant ETH Zurich, Switzerland Fall 2006–Present
Conducted research in the field of computer vision and microrobotics, in projects involving micro-robots for ophthalmic surgery, and microrobots for micromanipulation.

Student Advisor ETH Zurich, Switzerland 2007–2011
Supervised 15 students during their Bachelor Theses, Semester Projects, or Master Theses.

Teaching Assistant ETH Zurich, Switzerland 2007–2010
Prepared and conducted tutorial sessions and lectures for more than 80 students, for the course “Theory of Robotics and Mechatronics”. Assisted in the laboratory exercises for the “Introduction to Robotics and Mechatronics”. Co-advised and guided students for the participation in Robocup (micro-scale) 2009 (course of “Advanced Robotics and Mechatronics”).

IT Responsible ETH Zurich, Switzerland 2008–2011
Responsible for first-level IT support in Linux and Windows PCs at the Multiscale Robotics Laboratory of the Institute of Robotics and Intelligent Systems.

Computer Science Intern TU Berlin, Germany Summer 2005
Designed a mini content management system for the events and courses for Fak. 3 of TU Berlin. Contributed in the design of a geo-based portal for the institutes and universities of Berlin.

Beta-testing Intern Institute for Language and Speech Processing Summer 2004
Greece
Performed beta-testing on ‘Simfonia’, a greek-language spell-checking tool for Microsoft’s Word.

Laboratory Assistant NTUA, Greece 2002-2005
Performed exercise sessions for the courses of Introduction to Programming (PASCAL) and Programming Techniques (C), and provided feedback and assistance to more than 60 students throughout 4 semesters.

PROFESSIONAL ACTIVITIES

Research and networking workshop co-organizer: 2-day workshop for 50 participants, 2010.
Member of the recruitment and marketing team of Zurich's local IAESTE committee, 2008–now.
Student Member of the IEEE Robotics and Automation Society, 2004–now.
Student Member of the IEEE Engineering in Medicine and Biology Society, 2004–now.
IEEE Student Branch Board Member: Responsible for recruitment and marketing, 2005–2006.
Reviewer for Ro-Man 2008, BioRob 2008, ICRA 2009, 2010, 2011, IROS 2009, 2010, AIM 2010.

HONORS AND AWARDS

ETH Travel Support for the Int. Conf. on Robotics and Automation, Alaska, 2010.
Member of the World Champion ETH Team at the Nanogram League of Robocup, Austria, 2009.
Best Conference Paper Finalist and Best Student Paper Finalist at the Int. Conf. Biomedical Robotics and Biomechatronics, Arizona, 2008.
Greek Chamber of Engineers Award for overall academic performance (2001–2006), 2008. Best Presentation Award and Gold Medal at the Int. Genetically Engineered Machines Competition, MIT, Massachusetts, 2007.
Chr. Papakyriakopoulos mathematics award, NTUA, Greece, 2002, 2003.
N. Kritikos mathematics award, NTUA, Greece, 2002, 2003.
Ranked 1st among 300 students during 2001–2002, NTUA, Greece, 2002.
State Scholarship Foundation (IKY) award for excellent performance, NTUA, Greece, 2002.
Best Student Project Award for “Reducing Energy Consumption in School Buildings”, Greece, 2000.
Hellenic Ministry of Education Award for outstanding national-wide performance at the university entrance examinations, 2000.

MEDIA PUBLICITY

New Scientist: Drug-carrying robot roams through eye, 2011.
PBS: NOVA's Making Stuff Smaller, 2011.
Discovery Channel: How microrobots could prevent blindness, 2010.
Science et Vie Junior: Des microrobots dans le corps humain, 2010. [in french]
New Scientist: Rise of the Medirobots, 2009.
ETHLife: “MagMite” outperforms the competition, 2009.
Nouvo, TSR: Cherie, j'ai retrechi le medecin!, 2008. [in french]
The Economist: Swallow the surgeon, 2008.
ETHLife: Gold fuer gebildete Bakterien, 2007. [in german]

TECHNICAL SKILLS

Development: Matlab, C++, Qt4, OpenCV, C, PHP, OSLO, C#.
Operating Systems: Linux, Mac OS X, Windows XP/Vista/7.
Image Processing: ImageJ, Adobe Illustrator, Adobe Lightroom, Adobe Photoshop.

LANGUAGE SKILLS

Greek - *Native speaker*.
English - *Excellent* - Proficiency of Michigan, Proficiency of Cambridge.
French - *Intermediate* - Delf 1^{er} Degree.
German - *Basic/Intermediate* - 1 year studies, lived in Germany and Switzerland for 5 years.
Chinese - *Beginner* - 2 years of studies, but no recent practice.

HOBBIES

Building and painting miniatures.
Playing the piano.
Snowboarding.
Photography.

PUBLICATIONS

- C. Bergeles, B. E. Kratochvil, and B. J. Nelson, “*Visually Servoing Intraocular Microrobots*,” submitted to IEEE Trans. Robotics. [**journal**]
- C. Bergeles, K. Shamaei, J. J. Abbott, and B. J. Nelson, “*Single-Camera Focus-Based Localization of Intraocular Devices*,” IEEE Trans. Biomedical Engineering, vol. 57, no. 8, pp. 2064–2074, 2010. [**journal**]
- L. Zhang, J. J. Abbott, L. Dong, K. Peyer, B. E. Kratochvil, H. Zhang, C. Bergeles, and B. J. Nelson, “*Characterizing the Swimming Properties of Artificial Bacterial Flagella*,” Nano Letters, vol. 9, no. 10, pp. 3663–3667, 2009. [**journal**]
- O. Ergeneman, C. Bergeles, M. P. Kummer, J. J. Abbott, B. N. Nelson, “*Wireless Intraocular Microrobots: Opportunities and Challenges*,” J. Rosen, B. Hannaford, and R. Satava, editors, Surgical Robotics: Systems, Applications, and Visions, Springer, first edition, 2010. [**book chapter**]
- C. Bergeles, B. E. Kratochvil, B. J. Nelson, “*Model-Based Localization of Intraocular Microrobots for Wireless Electromagnetic Control*,” IEEE Int. Conf. Robotics and Automation (ICRA), 2011 (accepted). [**conference, full paper**]
- C. Bergeles, K. Shamaei, J. J. Abbott, and B. J. Nelson, “*Wide-Angle Localization of Intraocular Devices from Focus*,” in Proc. IEEE/RSJ Int. Conf. Intelligent Robots and Systems (IROS), pp. 4523–4528, 2009, St. Louis, MO, USA. [**conference, full paper**]
- C. Bergeles, K. Shamaei, J. J. Abbott, and B. J. Nelson, “*Wide-Angle Intraocular Imaging and Localization*,” in Proc. Int. Conf. Medical Image Computing and Computer Assisted Intervention (MICCAI), pp. 540–548, 2009, London, UK. [**conference, full paper**]
- C. Bergeles, G. Fagogenis, J. J. Abbott, and B. J. Nelson, “*Tracking Intraocular Microdevices Based on Colorspace Evaluation and Statistical Color/Shape Information*,” IEEE Int. Conf. Robotics and Automation (ICRA), pp. 3934–3939, 2009, Kobe, JP. [**conference, full paper**]
- C. Bergeles, K. Shamaei, J. J. Abbott, and B. J. Nelson, “*On Imaging and Localizing Untethered Intraocular Devices with a Stationary Camera*,” IEEE RAS/EMBS Int. Conf. Biomedical Robotics and Biomechanics (BioRob), pp. 489–494, 2008, Scottsdale, AZ, USA, **Finalist, Best Student Paper and Best Conference Paper**. [**conference, full paper**]
- C. Bergeles, M. P. Kummer, B. E. Kratochvil, J. J. Abbott, and B. J. Nelson, “*Ex-vivo Experiments with Intraocular Microrobots*,” Poster Presentation, in Proc. IEEE Int. Conf. Robotics and Automation (ICRA), Workshop on Mesoscale Robotics for Medical Interventions, 2010, Anchorage, AK, USA. [**workshop**]
- C. Framme, C. Bergeles, O. Ergeneman, B. E. Kratochvil, M. P. Kummer, S. Pane, V. Pocepcova, B. J. Nelson, “*Magnetically steered inserts for minimally invasive intravitreal surgical procedures*,” submitted to Deutsche Ophthalmologie Gesellschaft, 2011. [**conference, abstract**]
- K. Shamaei, C. Bergeles, J. J. Abbott, and B. J. Nelson, “*Ophthalmoscopy Using Direct Sensing of the Flat Aerial Image Created by an Aspheric Lens*,” WO 2010/034502 A2, 2008. [**patent application**]
- C. Bergeles, “*Visually Servoing Wireless Magnetic Intraocular Microrobots*,” ETH Zurich, Ph. D. Thesis, 2011. [**thesis**]
- C. Bergeles, “*Tracking Moving Objects with Emphasis on Human Gestures*,” NTUA, Diploma Thesis, 2006 (in greek). [**thesis**]